Crack propagation in disordered materials

How to decipher fracture surfaces

Thèse

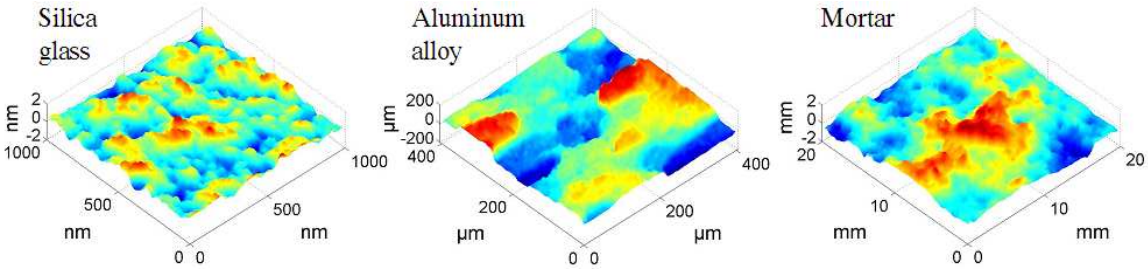
pour obtenir le titre de

Docteur de l'Ecole Polytechnique

Spécialité Physique

présentée par

Laurent Ponson



Soutenue le 24 Novembre 2006 devant le jury composé de :

Directeurs de thèse :	Daniel Bonamy
	Jean-Pierre Hulin
Rapporteurs :	Sergio Ciliberto
	Werner Krauth
Examinateurs :	Itamar Procaccia
	Michel Rosso
Président :	Stéphane Roux

Service de Physique et Chimie des Surfaces et Interfaces – CEA Saclay

Fluides, Automatique et Systèmes Thermiques – Univ. Paris VI et Paris XI

Contents

Table of Contents i
Acknowledgments iii
Collaborations iv
Introduction 1

1 Context and motivation **3**
1.1 At the continuum scale: The Linear Elastic Fracture mechanics . . . 4
1.2 Failure of disordered materials: The physical approach 11

2 Morphology of fracture surfaces revisited **19**
2.1 Materials and methods 20
2.2 Statistics of fracture surfaces 23
2.3 Anisotropy of fracture surfaces 28
2.4 Two-dimensional scaling properties of fracture surfaces 34
2.5 Physical interpretation 39
2.6 Concluding remarks 43

3 Low roughness exponents of fractured porous material surfaces **46**
3.1 Materials and methods 47
3.2 Fracture surfaces of glass ceramics 52
3.3 Roughness amplitude 58
3.4 Morphology of fractured sandstone surfaces 63
3.5 Concluding remarks 70

4 Fracture surfaces for model linear elastic disordered materials **71**
4.1 Model of crack propagation in ideal linear elastic disordered materials 72
4.2 Fracture surface of porous materials: Interpretation 82
4.3 Fracture surfaces of other brittle materials 97
4.4 Fracture surfaces of ductile materials : Interpretation 101

Conclusion **107**

Bibliography **110**

A Mechanical properties of glass ceramics **119**

B Publications **126**

Remerciements

J'ai été particulièrement gâté au cour de ma thèse car j'ai eu la chance d'avoir quatre encadrants. Et contrairement aux idées reçues (les soucis, ça croit proportionnellement – voir exponentiellement – avec le nombre de maîtres de thèse), j'ai vécu une expérience inoubliable. Leur disponibilité, leurs constants encouragements et leur passion qu'ils ont su, chacun à leur manière, me faire partager, ont fait de mes années de thèse trois très belles années.

Je tiens à remercier tout particulièrement Daniel Bonamy, pour avoir été le chercheur avec qui tout étudiant rêve de travailler. C'est à la fois mon ami, mon conseiller et mon mentor.

Je voudrais remercier ma "mère spirituelle", Elisabeth Bouchaud, pour avoir bien souvent éclairé mes pensées et pour m'avoir toujours bien conseillé, soutenu et encouragé.

Travailler avec Harold Auradou fut un grand plaisir. Je le remercie d'avoir supporté mon impatience. J'ai beaucoup appris avec lui et je lui en sais gré.

Je voudrais remercier Jean-Pierre Hulin qui a assuré le rôle de directeur de thèse, pour son incroyable disponibilité à toute heure du jour et de la nuit. De par ses compétences et son humilité, il est pour moi un modèle à suivre.

Je remercie Claude Guillot, qui a commencé cette thèse avec moi et qui nous a trop rapidement quitté. Il a été présent à mes côtés tout au long de ces trois années.

Je remercie très chaleureusement Sergio Ciliberto, Werner Krauth, Michel Rosso, Itamar Procaccia et Stéphane Roux qui m'ont fait l'honneur de participer à mon jury de thèse.

Merci à Daniel Bonamy, Jean-Pierre Hulin, Harold Auradou, Werner Krauth, Sergio Ciliberto et Itamar Procaccia pour leur relecture du manuscrit. Leur remarques et leur suggestions auront été précieuses.

Comment ne pas remercier tous ceux qui par leurs idées, leur encouragements, leur coup de main ou leur coup de pouce, ont contribué chacun à leur façon à ce travail de thèse. Merci à Luc Barbier, Alexandre Bataille, Hugo Bellenger, Thierry Bernard, Noushine Bonn, Jean-Philippe Bouchaud, Christophe Buisson, Fabrice Célarié, Stéphane Chapuliot, Gérard Chauvin, Guilherme Cordeiro, Olaf Duemmer, Eduardo Fairbairn, Claudia Guerra, Francine Guillot, Rajiv Kalia, ma bonne étoile, Jérôme Martin, Knut Jørgen Måløy, Stéphane Morel, Guillaume Mourot, Marc Pessel, Rafaël Pidoux, Silke Prades, Krishnaswamy Ravi-Chandar, Alberto Rosso, Cindy Rountree, Dominique Salin, Stéphane Santucci, Marcos Silvoso, Romildo Toledo, Reila Velasco, Stéphane Vernède et Philippe Vié.

Enfin, si ces années ont été si belles, c'est bien grâce à ma famille et mes amis. Merci à Brigitte, Raymond, Carine, Michel, Laure, Vincent, Elsa, Pierre, Hugo, Baptiste, Eva, à mes amis de Sartrouville, de Rio et de Paris.

Collaborations

La majorité des travaux présentés dans ce mémoire a été réalisée au sein du groupe "Fracture" au CEA Saclay et au sein du groupe "Mélanges et milieux dispersés" du laboratoire FAST. Toutefois, l'étude de surfaces de rupture de divers matériaux a impliqué l'utilisation de nombreuses techniques expérimentales – que ce soit pour synthétiser ces matériaux, les casser de façon contrôlée puis mesurer la topographie de leur surface – qui n'était pas toujours disponibles dans mes deux laboratoires d'acceuil. J'ai donc été ammené à collaborer avec d'autres groupes de recherche possédant les techniques adaptées. Cette page me permettra de remercier ces groupes, les personnes impliquées et de décrire très brièvement les expériences qui y ont été menées.

La synthèse et la caractérisation des frittés de verre, dont l'étude est présentée dans le chapitre 3, ont été effectuées par Philippe Vié du Laboratoire Central des Ponts et Chaussés à Champs-sur-Marne. J'ai effectué les tests de rupture de ces matériaux au cours de deux campagnes expérimentales effectuées au Département de Génie Civil de la COPPE à Rio de Janeiro et au Laboratoire de Rhéologie du Bois à Bordeaux. Les conseils et l'expérience de Guillerme Cordeiro et Eduardo Faribairn à Rio ainsi que ceux de Stéphane Morel et de Guillaume Mourot à Bordeaux auront alors été précieux. La grande majorité des surfaces de rupture obtenues ont été mesuré dans mes deux laboratoires d'accueil. Avec Harold Auradou, nous avons utilisé (et souvent réparé, merci Harold) le profilomètre point par point présent au laboratoire FAST. Quant au profilomètre mécanique du SPCSI, je l'ai utilisé avec Daniel Bonamy. Grâce à Christophe Buisson, j'ai pu utiliser le profilomètre optique présent dans les locaux de Taylor Hobson. Nous avons mené au FAST avec Harold Auradou l'ensemble de l'étude portant sur la rupture du grès.

L'étude sur le verre de silice a été menée au sein du groupe "Fracture" (par Silke Prades, Daniel Bonamy et moi-même). Les autres surfaces de rupture étudiées dans le chapitre 2 de cette thèse ont été obtenues dans d'autres laboratoires. Stéphane Morel et Guillaume Mourot du laboratoire de rhéologie du bois de Bordeaux m'ont très gentiment envoyé les relevés topographiques de surfaces de rupture de mortier et de bois. Philippe Ebert de Jülich en Allemagne nous a fourni des images STM de surfaces de quasicristaux. Elisabeth Bouchaud m'a gentiment prêté ses éprouvettes d'alliage d'aluminium dont nous sommes allé mesurer les surfaces au Laboratoire d'Etude des Microstructures à Châtillon avec l'aide de Jean-Louis Pouchou et Denis Boivin. Stéphane Chapuliot m'a gentiment prêté ses éprouvettes d'alliage métallique que nous avons ensuite étudiées au SPCSI. Il m'a également initié aux plaisirs des simulations éléments finis qui m'auront maintes fois servies au cours de ces trois ans. J'ai développé les méthodes d'analyse statistique 2D des surfaces rugueuses et les ai appliquées aux surfaces expérimentales. De façon générale, l'analyse statistique des surfaces de rupture est un travail personnel. J'ai mené l'étude théorique presentée dans le Chapitre 4 en collaboration avec Daniel Bonamy.

Introduction

Understanding how materials break is both of fundamental and of practical interest. Most people are confronted to this problem in daily life e. g. when they drop inadvertently their cup of coffee. For the engineering standpoint, the question is much more crucial than in our daily problems: How to create materials with longer life-time and improved resistance to shock and stress fluctuations.

Since the pioneering work of Griffith, a coherent theoretical framework, the Linear Elastic Fracture Mechanics (LEFM) has been developed. It states that — in an elastic material — a crack is initiated when the mechanical energy released by the crack advance is sufficient to balance the energy needed to create new surfaces. This approach has been proved to be extremely powerful as long as one considers ideal homogeneous media, but is more questionable for real disordered materials. Indeed, as soon as one considers real materials, its microstructural disorder plays a crucial role and many questions remain, in a great extent, without answers: What sets the strength of a material? Which factors determine its life-time? How can one relate these quantities to the material microstructure?

Why is the role of the disorder so crucial to understand the failure of materials? At first, when we pull on a solid, its resistance to failure is not ruled by an average response of the material, but by the behavior of little parts of it, that act as "weak links" and are responsible for the failure of the whole structure [1]. On the other hand, when we consider a crack propagating in a solid, some rare specific processes occurring at the crack tip can have a giant effect on the average macroscopic behavior. In particular, the presence of a crack enhances catastrophically the effects of the disorder.

The main objective of this work is precisely to identify and quantify the effects of the microstructural disorder on the failure of a material. More precisely, we will study - both theoretically and experimentally - its implication on the path chosen by the crack to propagate, which sets the morphology of the *post mortem* fracture surfaces.

Therefore, we have focused on the roughness displayed by the fracture surfaces, the morphology of which is expected to encode the various failure processes. But what is precisely the information we can get from their geometry? Is it possible to

analyze the failure processes by studying *post mortem* the roughness of cracks?

This manuscript is divided into four chapters. In the Chapter 1, I give the context and motivations of this study. After a brief introduction to the continuum approach of failure problems, I review recent developments investigating the fracture of disordered materials.

In the Chapter 2, the morphology of fracture surfaces that were intensively studied during last two decades is revisited. Five very different disordered materials are investigated. Using new methods of analysis, we will provide new insights on the scaling properties of cracks. We will show that a full description of the fracture surfaces requires a 2D description involving *two* universal scaling exponents, independent of the material.

The Chapter 3 is devoted to the experimental investigation of fractured sandstone surfaces that were reported to display puzzling scaling properties [2]. We study an artificial sandstone, a glass ceramics made of sintered beads, quite comparable with natural sandstone but with a microstructure that can be tuned experimentally. The investigation over a broad range of porosities, grain sizes and crack growth velocities leads us to conjecture the existence of a second universality class for failure problems.

The Chapter 4, mainly devoted to a theoretical investigation of the geometry of fracture surfaces, makes the link between fracture morphology and failure mechanisms in disordered materials. By integrating the effects of the material disorder to the theoretical framework of the Linear Elastic Fracture Mechanics, one gets predictions on the statistical properties of fracture surfaces of ideal linear brittle materials in *quantitative* agreement with the experimental observations of Chapter 3. The origin of the scaling properties of fracture surfaces studied in Chapter 2 is then discussed.

Chapter 1

Context and motivation

Contents

1.1 At the continuum scale: The Linear Elastic Fracture mechanics 4

1.2 Failure of disordered materials: The physical approach . 11

Despite the great interest of scientists for solid-state physics during the two last centuries, the first step to understand how materials break was taken in 1913 [3]. And this first step was to identify the intrinsic difficulty of failure problems, the fact that its study involves a singularity. Indeed, a crack is only sensitive to a zone of small extension near its tip so that the macroscopic behavior of the material is governed by local mechanisms. Developed all over the twentieth century, Linear Elastic Fracture Mechanics (LEFM) brings a solid theoretical framework to describe how cracks propagate in homogeneous ideal media. But this continuum approach neglects the effects of the material structure – defects, microstructural disorder - – that can have catastrophic consequences on crack propagation. Therefore, the LEFM leaves many fundamental questions open: How to predict the strength of a real material? Its life-time? In the vicinity of the crack tip, *i.e.* at the scale of the material microstructure, it is difficult to neglect the disorder of a material. And the crack, sensible to a small zone near its crack tip, enhances the effects of this disorder so that the crack propagation is not ruled by the average behavior of a material but by its more vulnerable spots. The influence of the microstructural disorder of a material on the propagation of a crack is the central point of this study. After a brief introduction to the continuum approach, we will review recent developments investigating failure of disordered materials, and will present the challenging questions about crack propagation that are raised by the presence of disorder.

1.1 At the continuum scale: The Linear Elastic Fracture mechanics

Failure of flawless solids : Let us first consider a very simple solid and estimate its strength. In first approximation, it appears natural to model the solid as a network of springs of lengths a (interatomic length) and stiffness E (Young's modulus), the so-called Young's modulus of the material. As represented in Fig. 1.1, when submitted to

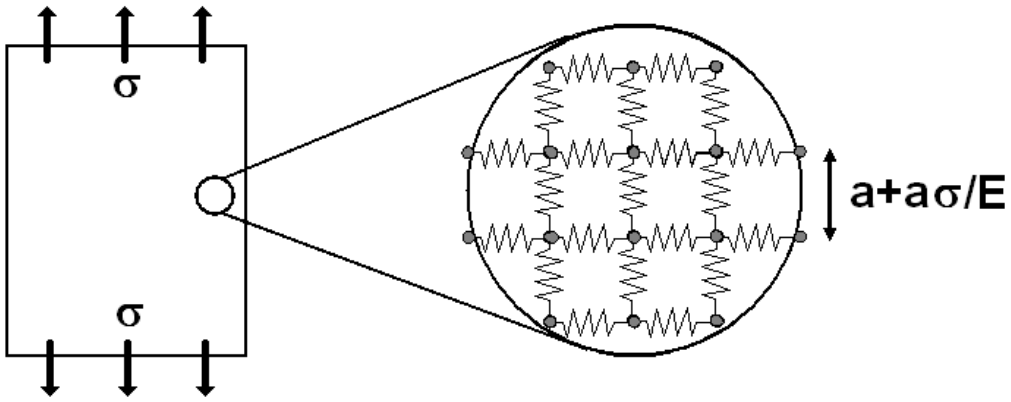


Figure 1.1: An ideal flawless solid is submitted to an exterior stress σ. Its atomic bonds – described by springs of stiffness E and length a – can undergo a deformation $\delta a = a\sigma/E \simeq a/5$ before rupture. This leads to a "theoretical" strength $E/5$ for a perfect material.

an external stress σ, the atomic bonds stretch over the length $\delta a = a\sigma/E$. Suppose now that a bond is broken if two neighboring atoms move apart by 20 % of their original spacing[1], *i.e.* for a deformation $\delta a_c = a/5$. Thus, the failure of the material is obtained for the critical stress $\sigma_c = E/5$. This estimation is compared to practical

Material	Young's modulus E	Theoretical strength $E/5$	Practical strength
Steel	200 GPa	40 GPa	500 Mpa
Glass	70 GPa	14 GPa	300 Mpa
Al_20_3	400 GPa	80 GPa	100 MPa

Table 1.1: Comparison between theoretical and practical strengths of materials. The measured strengths are about two orders of magnitude smaller than the predictions for a flawless solid described in Fig. 1.1.

[1]Sophisticated quantum-mechanical calculations can confirm that this rough estimate is rather good [4].

strengths of materials in Table 1.1. This oversimplified model predicts a strength σ_c which is two orders of magnitude larger than the experimental measurements. In other words, the strength of materials is far from being directly given by bonding energies. An ingredient is clearly lacking in our simplistic model: the presence of flaws in materials.

Introduction of cracks : Let us change slightly our previous model by introducing a flaw in our ideal elastic solid. Inglis, in his work published in 1913 [3], analyzed the effects of a defect on the stress field in the material. Considering an elliptical cavity of semi-axes b and c, in the solid submitted to an external stress σ as represented in Fig. 1.2, Inglis showed that the effective stress acting at point P where the local radius of curvature $\rho_P = b^2/c$ is minimal, is

$$\sigma_p = \sigma \left(1 + 2\sqrt{\frac{c}{\rho_p}}\right) \tag{1.1}$$

Considering the case $b \ll c$ corresponding to a sharp defect, the ratio $\frac{\sigma_p}{\sigma}$ of the normalized stress undergone by the material at the tip P becomes $\simeq 2\sqrt{\frac{c}{\rho_p}}$. This ratio can be much larger than unity for slender cavities. The resulting *stress concentration* in the vicinity of defects may explain the discrepancy between practical and theoretical strengths of materials (see Table 1.1). Indeed, considering micrometer-sized flaws, *i.e.* $\rho_p \simeq 1$ Å and $c \simeq 1$ μm, one gets $\sqrt{\frac{c}{\rho_p}} \simeq 100$. Let us note that it is the shape of the defect rather than its size that sets the factor of stress concentration. Moreover, one microscopic flaw in an homogeneous material is enough to modify crucially the macroscopic behavior of a solid. In part, this explains why the extreme of the characteristic parameters of the material are often more useful than averaged quantities to predict the resistance to rupture of materials.

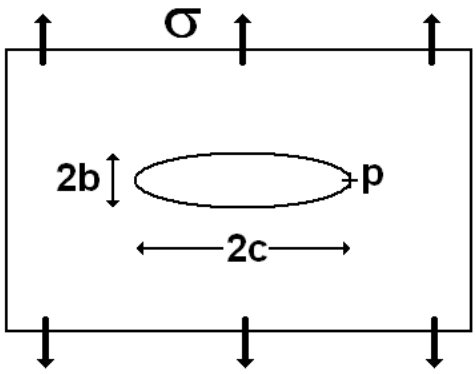


Figure 1.2: Plate containing an elliptical cavity, semi-axes b and c, subjected to uniform applied tension σ.

The next step to understand how materials break was achieved by Griffith in 1920 [5]. He considered the limit case $c/\rho_p \to \infty$ equivalent to a slit crack in our ideal elastic homogeneous solid. In that case, the stress is diverging at its tip as expected from Eq. (1.1). Let us investigate in detail the stress field in this geometry.

The rupture modes : To assess the stress field in the vicinity of the slit crack tip, it is useful to distinguish the three basic modes of crack surface displacement. Mode I, II and III are displayed in Fig. 1.3 and correspond respectively to the tensile, shear and tear mode. The relevance of this description lies in the fact that the stress field near the tip of a slit crack in an elastic solid can be written as the sum of the contributions of each mode, irrespective of the load/displacement applied to the solid.

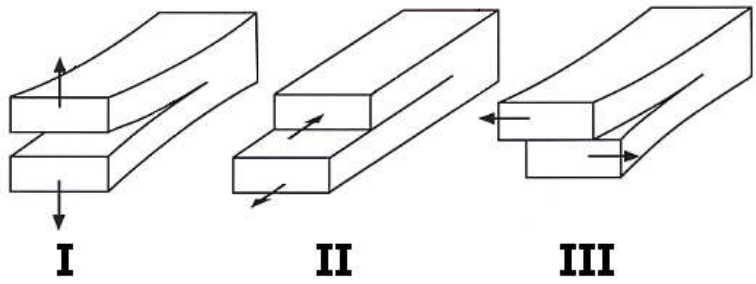


Figure 1.3: The three modes of fracture: I, tensile mode; II, shearing mode; III, tearing mode.

Stress field at the crack tip : Let us focus first on a pure mode I loading[2] In 1958, Irwin [6] showed that, in the very vicinity of the crack, the stress field in the rectangular coordinate system of Fig. 1.4 can be written as

$$\begin{aligned} \sigma_{xx} &= \frac{K_I}{\sqrt{2\pi r}} \cos(\theta/2)(1 - \sin(\theta/2)\sin(3\theta/2)) \\ \sigma_{yy} &= \frac{K_I}{\sqrt{2\pi r}} \cos(\theta/2)(1 + \sin(\theta/2)\sin(3\theta/2)) \\ \sigma_{xy} &= \frac{K_I}{\sqrt{2\pi r}} \sin(\theta/2)\cos(\theta/2)\cos(3\theta/2) \end{aligned} \tag{1.2}$$

Here, K_I is the so-called stress intensity factor. This quantity depends both on the geometry of the system and on the external loading.

[2]In the following, we will study experimental systems under dominant mode I. loading. This choice is motivated because (i) mode I generates fracture surfaces avoiding any possible destructive friction between the two corresponding crack surfaces; (ii) There is always a tendency for cracks to seek an orientation that minimizes the mode II loading, leading to a dominant tensile mode.

Let us note that non-diverging terms contribute also to the stress field near the crack tip. They can be developed as a $r^{k/2}$ expansion with $k \geq -1$

$$\sigma_{ij} = \frac{K_I}{\sqrt{2\pi r}} g^{ij}(\theta) + T_I k^{ij}(\theta) + A_I l^{ij}\sqrt{r} + ... \tag{1.3}$$

Here g_{ij} are the functions given in Eq. (1.2). k^{ij} and l^{ij} are also universal functions of θ (i and j denotes both either x or y).

Mode II and mode III loadings lead to the same form of stress field as given in Eq. (1.3) but with stress intensity factors K_p as well as the functions g_p, k_p and l_p depending on the mode $p = \{\mathrm{II}, \mathrm{III}\}$. As mentioned previously, the stress field for mixed modes is given by the sum of the three contributions.

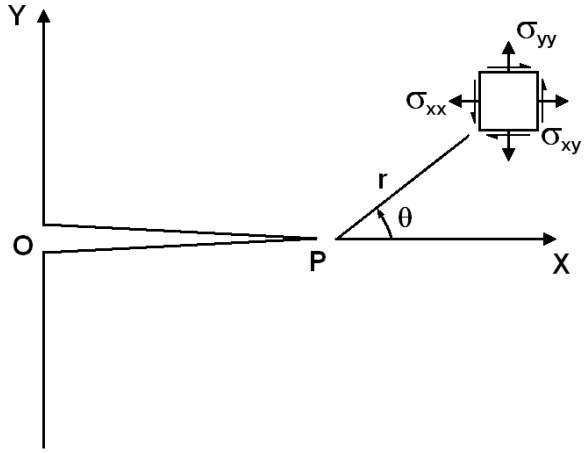


Figure 1.4: Stress field in the vicinity of the crack tip P.

Stress intensity factor and energy release rate : The value of the stress intensity factors K_I, K_{II} and K_{III} fully determines the diverging part of the stress field in the vicinity of a slit crack. The stress intensity factor K_I in the tensile mode will be shown to determine the stability of a crack while the value of K_{II} will determine the path followed by the crack for two-dimensional systems as in Fig. 1.4. Therefore, many methods have been developed to assess the quantities K_I, K_{II} and K_{III}, expressed in $\mathrm{Pa\,m^{1/2}}$. For a sample under a uniform applied tensile stress σ, the stress intensity factor in mode I takes the form

$$K_I = \psi \sigma c^{1/2} \tag{1.4}$$

Here, c is the crack length and ψ is a dimensionless quantity depending on the geometrical parameters of the system. For example, for an infinite sample with a slit notch (Fig. 1.2 with $b \to 0$), one has $\psi = \sqrt{\pi}$. More generally, for more complex loading

conditions/geometries, the value of the stress intensity factors can be found in hand books (see for example Ref. [7]) or determined through finite element calculations. We used mainly this last method in our work.

First, let us derive a criterion for crack propagation. The amount of elastic energy δE_{el} released by a solid in pure mode I loading when a slit crack propagates on an infinitesimal length δc is[3] $\delta E_{el} = \delta c \frac{K_I^2}{E}$ (see Ref. [8] for the demonstration) where E is the Young's modulus of the material. This energy release rate [4] is

$$G_I = \frac{\delta E_{el}}{\delta c} = \frac{K_I^2}{E} \tag{1.5}$$

For the crack to propagate, the energy released by the system must at least balance the energy required to create two new surfaces. Therefore, the so-called Griffith's criterion[4] for crack propagation is[5]

$$G_I \geq G_{Ic} \tag{1.6}$$

One can define also the toughness of the material $K_{Ic} = \sqrt{G_{Ic}E}$. Using Eq. (1.5), one gets another criterion of crack propagation equivalent to Eq. (1.6)

$$K_I \geq K_{Ic} \tag{1.7}$$

The toughness – as well as the fracture energy – is an intrinsic quantity of a material. It can be measured experimentally and is therefore available for various materials. However, a theory that would relate the microstructural properties of a material to its toughness is still missing. In particular, we don't know how to estimate the toughness of a multi-compound material from the toughness of its elements.

For the ideal elastic homogeneous medium studied here, the behavior of a slit crack is entirely determined by its stress field in the tip vicinity: Its stability is set by K_I and its possible deflection is set by K_{II}. Indeed, a crack chooses the path for which the local stress field is of mode I type ("criterion of local symmetry") [9, 10, 11]. In other words, the mode II stress intensity factor vanishes at the tip

$$K_{II} = 0 \tag{1.8}$$

The "criterion of local symmetry" was proposed to predict the crack path for two-dimensional problems.[6] For three-dimensional systems, the role of K_{III} on the crack path is still an open question (see for example Refs. [12, 13]).

[3] in plane stress conditions ($\sigma_{zz} = 0$).

[4] For a pure mode I loading.

[5] Note that the fracture energy G_{Ic} is different from the surface tension because the rupture involves dissipative and irreversible processes: Once broken, the material cannot be healed by simply bringing back the two pieces into contact.

[6] Invariant along z as in Fig. 1.4.

The case of ductile failure : In this paragraph, we deal with a first obstacle towards the description of crack propagation in real materials. While until now, a slit crack in an ideal homogeneous elastic medium, referred to as perfectly brittle crack propagation, has been addressed, we tackle now the problem of ductile failure. This is a common thing to say that some materials are brittle while others are ductile. In fact, this distinction is directly related to the manner a crack propagates in the material. Let us consider a solid with a sharp preexisting crack. For some materials, the crack propagates by breaking interatomic bonds one after the other, while for the others, the material deforms irreversibly before the crack starts to propagate.

But this distinction must be taken cautiously. For example, we keep qualifying the glass as brittle while it has been shown that, at the nanometer scale, a crack propagates through nucleation, growth and coalescence of damage cavities [14, 15]: Is the notion of brittle and ductile a matter of observation scale or a question of material?

The assumption of ideal brittle rupture – or infinitely sharp crack – is violated as soon as we consider real materials. At first, the divergence of the stress field at the crack tip is physically unacceptable. Therefore, mechanisms relaxing this stress are expected in a more or less extended process zone near the tip. Second, fracture is an irreversible process; thus, the fracture energy is always greater than the energy required to create the new surfaces. This suggests the existence of dissipative processes, even for cleavage of crystals (see for example the Refs. [16, 17, 18] that debates whether the classical picture of ideal brittle fracture for crystal cleavage is correct). Finally, let us note that the size of this so-called process zone varies from one material to the other. The dissipative processes, damage, are material specific.

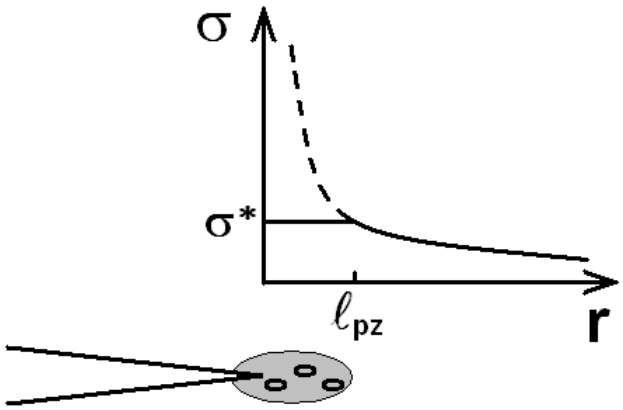


Figure 1.5: Variation of the tensile stress σ at the crack tip of a single crack. The distance to the crack tip for which the stress field without damage ($\sigma = \frac{K_I}{\sqrt{2\pi r}}$) is equal to the intrinsic strength σ^* of the material gives a good estimate of the process zone size ℓ_{PZ} (see Eq. (1.9)).

Under some assumptions, it is however possible to reconcile crack propagation involving these non-linear processes with the framework of Linear Elastic Fracture Mechanics. This is called the *small scale zone* assumption. It assumes that these dissipative processes are localized in a zone of finite extent in the vicinity of the crack tip.[7]

In that case, it is possible to assess the extent of this zone. We give here a very simple argument illustrated in Fig. 1.5 and leading to an estimate of this zone. A more sophisticated and realistic model is given in Ref. [19]. The size $\ell_{\rm PZ}$ of this so-called process zone is assimilated to the maximum distance from the crack tip where the tensile stress imposed by the presence of the crack is sufficient to induce irreversible damage. At this distance, the stress level is expected to be $\frac{K_{Ic}}{\sqrt{2\pi\ell_{\rm PZ}}}$ (see Eq. (1.2)). This stress is sufficient to induce irreversible deformation in the material. Therefore, it is equal to the intrinsic tensile strength σ^* of the material. Hence[8]

$$\ell_{\rm PZ} \simeq \frac{\pi}{8}\left(\frac{K_{Ic}}{\sigma^*}\right)^2 \tag{1.9}$$

Using this approach, a crack involving localized damage processes can be treated as a slit crack propagating in an equivalent linear elastic medium. The beauty of this theory lies in the very simple resulting criterion of crack propagation: If the stress intensity factor K_I – that depends only on the imposed boundary conditions and the geometry – is larger than the toughness K_{Ic}, the crack propagates. Unfortunately, this is also the weakness of this macroscopic approach. Indeed, the quantity K_{Ic} that, admittedly, can be experimentally measured, hides all the irreversible mechanisms of rupture at the microstructure scale. A complementary approach, that would give the physical meaning of the toughness of a material, seems necessary.

To summarize, the Linear Elastic Fracture Mechanics provides predictions on the motion of a crack based on an energy balance: The energy provided to the material when it is loaded – stored as elastic energy in the solid – must balance the energetic cost for making a crack propagate – energy required to create two new surfaces. This framework can be used even for ductile fracture if the process zone is small enough. Unfortunately, this macroscopic approach is restricted to ideal homogeneous media. As soon as one considers real materials, its microstructural disorder plays a crucial role. This is the central point of the following section.

[7] In other words, we suppose that it is still possible to find a length scale above which the effects of the dissipative processes localized at the tip have vanished. We will see in the following that such an assumption is impossible for the effects of the disorder of a material.

[8] The coefficient in Eq. (1.9) is larger than the one expected from the simple derivation shown here. To get the correct prefactor, one needs to use the more sophisticated model of the Barenblatt crack [19].

1.2 Failure of disordered materials: The physical approach

Position of the problem : Linear Elastic Fracture Mechanics provides a framework to predict the motion and trajectory of a crack in an ideal homogeneous elastic medium. In real materials, one would expect that this framework remains valid but at a scale larger than both the process zone size and the microstructure scale. This is not the case, unfortunately for engineers and thankfully for physicists. Microscopic mechanisms, even very localized in a small zone in the vicinity of the crack tip, can have macroscopic consequences on the motion of the crack and its trajectory. This effect is characteristic of failure problems: Because of the stress concentration, the crack enhances catastrophically the effects of mechanisms localized at its tip. In other words, rare specific processes can have a giant effect on the averaged macroscopic behavior. This is true in the case of an ideal elastic homogeneous material where the crack motion is determined by the quantities K_I and K_{II} that are rigorously defined at the tip by $K_I = \lim_{r\to 0} \sqrt{2\pi r}\sigma_{yy}(r, \theta = 0)$ and $K_{II} = \lim_{r\to 0} \sqrt{2\pi r}\sigma_{xy}(r, \theta = 0)$ (see Eq. (1.2) and (1.3)). And this is also true for more realistic cases. Therefore, theoretical approaches – such as homogenization technique – that would amount to neglect small-scale effects to predict macroscopic behavior must be considered carefully.

The central point of this work is the transition from microscopic processes to macroscopic behavior in failure problems for real material: What are the effects of the microstructural disorder of the material on the macroscopic behavior of the crack? The classical approach defines an "effective" equivalent homogeneous medium using "effective" quantities. The macroscopic behavior of the material at length scales larger than the disorder would then coincide with that of this so-defined "equivalent" homogeneous medium. For example, it is natural to define the effective Young's modulus E_{eff} either (i) experimentally by measuring its response to a perturbation with a wavelength larger than the typical length scale ξ_d of the disorder/microstructure (see Annexe A for the experimental setup) or (ii) theoretically by using homogenization techniques that gives the relation between the effective Young's modulus E_{eff} and the ones of each component of the disordered material (see for example Ref. [20]). With regard to its elastic response, the macroscopic (at scales larger than ξ_d) behavior of the disordered material is strictly identical to that of the so-defined effective homogeneous medium with Young's modulus E_{eff}.

For failure problems, this approach is not valid. For example, let us consider a material characterized by a one-dimensional disorder as represented in Fig. 1.6. It is made of two compounds a and b characterized by their toughness K_I^a and K_I^b, respectively ($K_I^a < K_I^b$). To make the crack propagate through the whole material, one must apply a stress intensity factor K_I^{applied} at least equal to K_I^b. Indeed, if $K_I^a < K_I^{\text{applied}} < K_I^b$, the crack is "pinned" in the grey regions. Therefore, the macroscopic stress intensity factor of this model heterogeneous material is equal to

K_I^b, irrespective of the properties of the phase a. We can now consider a material made of N different sections of toughness K_I^i. The macroscopic toughness is then given by the maximum value of the K_I^i so that a relatively small part of the disordered material rules its whole behavior.

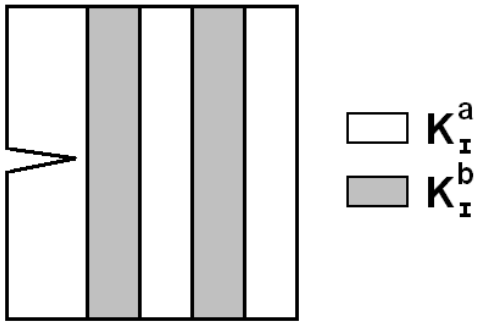


Figure 1.6: Ideal two-compounds material characterized by a one-dimensional disorder. If the toughness K_I^a of the compound a is lower than K_I^b, that of the compound b, then the macroscopic toughness of the material is K_I^b, irrespective of the properties of the compound a.

The morphology of fracture surfaces which is reminiscent of the path followed by a crack is also a good experimental example of the failure of the classical techniques. For an ideal homogeneous medium under a pure mode I loading, these surfaces are flat. For a real material[9] under the same loading, it is self-affine, *i.e.* rough at all length scales, even much larger than the typical length scale ξ_d of the disorder. It is clear that in this example, to reconcile the behavior of the ideal homogeneous system – the predictions of the LEFM – with that of the disordered material is not an easy task: There is no length scales at which the behavior of the two media – here the morphology of the fracture surface – will coincide. In other words, the transition from homogeneous to disordered material is not "smooth" in view of the macroscopic behavior of the crack. Even very slightly disordered material will behave differently than any homogeneous one. The example of self-affine fracture surfaces leads to the conclusion that LEFM, as it has been developed for homogeneous media, will never reproduce all the characteristics of crack propagation in real materials. In order to prospect the relevant alternative theory, let us review the mean features of the effect of the disorder on crack propagation.

Clues for a critical phenomenon : Coming back to the example of the geometry of fracture surfaces, one realizes that the crack enhances the microscopic disorder so that we cannot define a length scale at which its effects become negligible. This

[9]therefore characterized by a microstructural disorder.

lack of characteristic length scales may be reminiscent of a critical phenomenon, and the exponents involved in the scaling laws measured for fracture problems may be universal. We give here some clues that support this idea:

(a) As previously emphasized, failure of disordered materials results in fracture surface geometry without characteristic length scales. Moreover, the scaling properties of the roughness of crack surfaces are characterized by universal quantities – the scaling exponents – that do not depend on the nature of the materials – the details of the disorder properties. power-law behavior and universal aspect of crack surfaces suggest the existence of an underlying phase transition for failure problems in disordered media. The main properties of fracture surfaces are reviewed in detail in paragraph 1.2.

(b) The study of the local velocities of a crack front suggests a burst-like dynamic involving avalanches of all sizes. Studying the dynamical properties of the crack, it appears impossible to define both a characteristic local velocity and avalanche size. Fig. 1.7 a displays the distribution of local velocity of a crack front propagating in a disordered weak plane between two sandblasted plates of Plexiglas sintered together as measured by Måløy, Santucci *et al.* [21]. Fig. 1.7 b shows the avalanche size distribution involved in the burst-like dynamics of the front motion for the same experiment. In addition to the power-law behaviors,

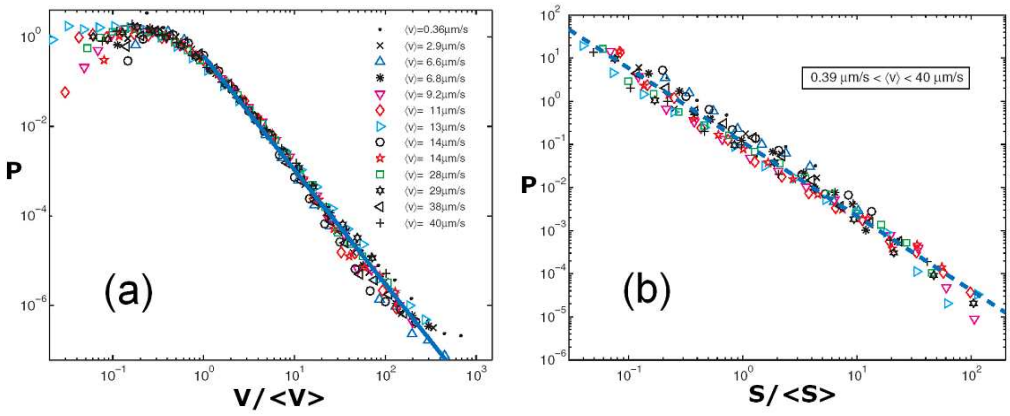


Figure 1.7: (a): Distribution of the local velocities measured on a crack front in motion in a disordered weak plane between two plates of Plexiglas sintered together (Courtesy of K. Måløy, S. Santucci and co-workers [21]). (b) Avalanche size distribution involved in the burst-like dynamics of the front motion (Courtesy of K. Måløy, S. Santucci and co-workers [21]). Note that the value of the scaling exponents – the slope of the power-law fit in this logarithmic scale – do not depend on the mean velocity $\langle v \rangle$ of the front. This "universal" burst like dynamics suggests that the crack front motion could be described as a dynamic phase transition.

one observes that the value of the scaling exponents – the slope of the straight lines in this logarithmic scale – are very robust: They do not depend on the mean crack growth velocity of the crack front $\langle v \rangle$ and the sample preparation – the details of the disorder of the weak plane – in the range investigated. This "universal" burst like dynamics of the crack front seems reminiscent of critical phenomena.

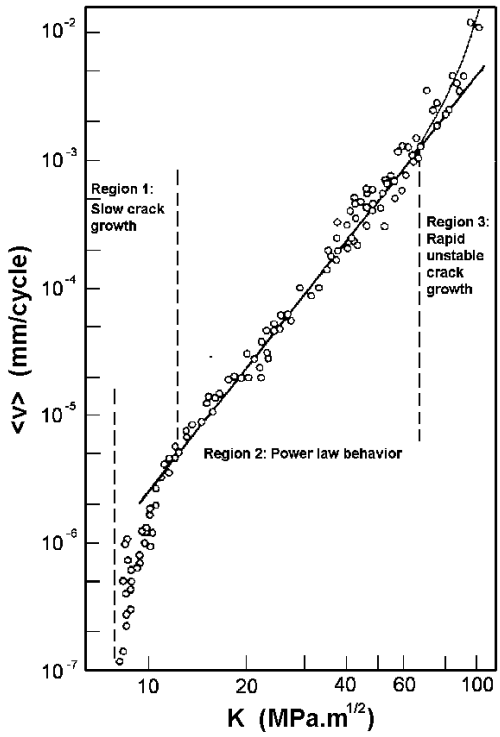


Figure 1.8: Mean crack growth velocity $\langle v \rangle$ of a crack front propagating in a steel under cyclic loading – fatigue regime – as a function of the stress intensity factor $\Delta K = K_{\max} - K_{\min}$ [23].

(c) In addition to its local velocity and its geometry, the macroscopic motion of a crack involves also remarkable properties, however still unexplained. Fig. 1.8 displays the mean velocity of a crack propagating in an aluminum alloy in the fatigue regime – also referred as subcritical regime because $K_I < K_{Ic}$. The velocity of the crack evolves as a power-law of the applied stress intensity factor and $\langle v \rangle \simeq (\Delta K_I)^n$. Contrary to the other experimental examples, the exponent n seems to be material dependant. As suggested in Ref. [22], the remarkable features of the law relating the crack growth velocity – order parameter in the theoretical framework of dynamic phase transitions – and the applied stress intensity factor – control parameter in this same framework – could be explained

in the frame of a description of crack propagation in disordered material as a dynamic phase transition.

The features of crack propagation in disordered materials suggest that it could be described as a critical phenomenon. The fundamental issue in this work is:

(i) Can we provide convincing arguments that crack propagation in disordered materials is a critical phenomenon?

(ii) To which extend can we characterize it?

Many theoretical efforts have been devoted to this issue. In the last paragraph of this section, we will briefly review the four main competing theories that were proposed to explain the universal features observed during the failure of disordered materials. But first, we will present one of the major results obtained these past twenty years concerning the scaling properties of the roughness of fracture surfaces.

Scaling properties of fracture surfaces : The Holy Grail : Because fracture surfaces have been largely experimentally investigated since the 80's and because their morphology is the immediate signature of the failure mechanisms, this morphology has often been chosen as a first test for the various theories of crack propagation in disordered materials. In other words, a relevant model of failure of disordered materials is expected to reproduce in the first place the rather remarkable properties of scaling invariance of the roughness exhibited by fracture surface. Prediction of the competing models can then be compared with respect to each other. This experimental test, although indirect, is easier to do than on other aspects of failure in disordered materials such as the dynamical properties of cracks.

Here, we will give the main experimental results reported on the geometry of fracture surfaces. In particular, we will focus on their universal properties, *i.e.* independent of the material. Scientists have for a long time studied the morphology of fracture surfaces to improve their knowledge of the complex processes occurring at the microstructure scale during the failure of heterogeneous materials [24]. For example, engineers have widely used fracture surface analysis to determine the reasons of failure of a solid. More recently, the roughness of fracture surfaces became the center of interest of physicists studying the physical aspects of material failure. Indeed, in the pioneer work published in Ref. [25] in 1984, Mandelbrot *et al.* showed that fracture surfaces of various kind of metallic alloys exhibited very remarkable properties of scale invariance. Studying a wide range of aluminum alloys of different toughness, Bouchaud *et al.* [26] measured however the same value for the scaling exponent that characterized the roughness of their crack surface. They conjectured that this value was "universal". Måløy *et al.* [27] performed the same analysis on fracture surfaces of six materials (porcelain, steel, graphite ...). All these experimental results led to the conclusion that the roughness of fracture surfaces is self-affine and characterized

by a so-called roughness exponent $\zeta \simeq 0.8$ independent of the material. One of the key consequence of this scaling invariance is

$$\Delta h(\Delta r) \sim \Delta r^{\zeta} \tag{1.10}$$

where Δh is the 1D height−height correlation function computed on height profiles extracted on the fracture surface and defined as $\Delta h(\Delta r) = \langle (h(r + \Delta r) - h(r))^2 \rangle_r^{1/2}$. Figure 1.9 displays the way we compute this function on a rough profile taken from a fracture surface of silica glass. Let us note that many other disordered materials were then investigated (granite [28], wood [29], mortar [30] ...). All these experiments confirmed the value of the "universal" roughness exponent $\zeta = 0.8$.

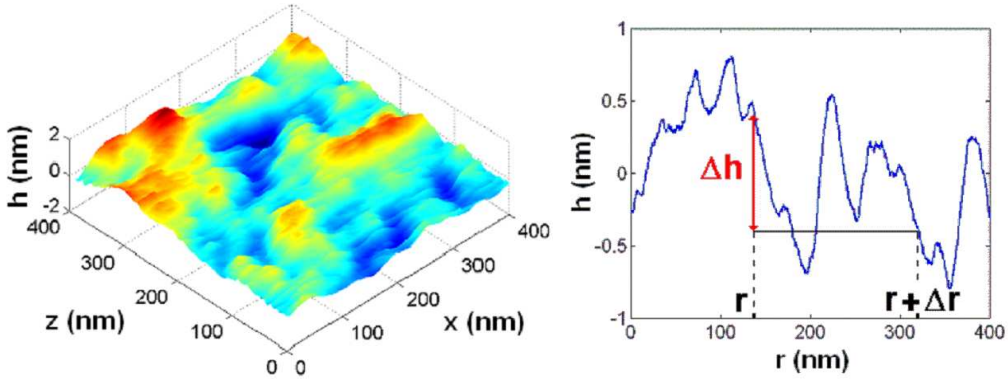


Figure 1.9: Computation of the 1D height−height correlation function $\Delta h(\Delta r)$ on the example of a fracture surface of silica glass. The profile of interest (right) is measured along a given direction of the fracture surface (left). In addition to the use of a 3D representation, the colors on the left figure correspond to the height of each point of the fracture surface. This allows for a good visualization of the surface roughness.

Some studies reported exceptions to the universality of the roughness exponent. Metallic surfaces investigated at the nanometer scale were found to display self-affine scaling properties, but with a roughness exponent significantly smaller than 0.8, closer to $0.4 - 0.5$ [31, 32, 22]. On the same surfaces, the "universal" roughness exponent $\zeta \simeq 0.8$ was also observed, but at larger scales. Similar observations were reported for silicate glasses [22]. Measurements corresponding to various crack growth velocities were performed both for a silicate glass and Al-based metallic alloys [32, 22]. They observed that the crossover length between the two self-affine domains ($\zeta \simeq 0.45$ at small scales and $\zeta \simeq 0.8$ at large scales) was decreasing when the crack growth velocity was increasing. In other words, for very small velocities, the small scale domain is expected to become broader. The universality of this small scale regime was later questioned since no small scale $\zeta \simeq 0.4 - 0.5$ roughness exponent was observed for nanoresolved fracture surfaces of silica glass broken under stress corrosion with crack

growth velocities as small as a picometer per second [33, 34]. The effects of the crack growth velocity on the morphology of fracture surfaces are widely studied here. No effects are observed (see Chapter 2) for crack growth velocities varying on more than 12 decades (from some picometers to some meters per second).

On the other hand, recent experiments reported similar values $\zeta \simeq 0.4-0.5$ *at large length scales* in sandstone [2, 35]. This "apparent" exception to the widely reported roughness exponent $\zeta \simeq 0.8$ will be studied in Chapter 3. This experimental result will be proved to be the starting point towards the understanding of the fracture surface morphology.

In the next paragraph, the main models of failure of disordered materials are reviewed. Unfortunately, we will see in chapter 2 that they are unable to reproduce the properties of experimental fracture surfaces.

The competing models : We describe now the four main models of failure of disordered materials. For each of them, we give their predictions for the fracture surface geometry.

(i) Bouchaud *et al.* [36] proposed to model the crack front as an elastic line moving through randomly distributed microstructural obstacles – the dynamics of which is described through a phenomenological Langevin equation, keeping only the terms allowed by the symmetry of the system. The fracture surface is then the trace left by the moving front. The geometry of an elastic line moving in a 3D random medium has been studied in Refs. [37, 38]. The scaling exponents characterizing the line – and therefore the roughness of fracture surfaces – depend on the coefficient involved in its motion equation. But on general grounds, for such a moving line just above its depinning transition, one expects two scaling regimes: At small (resp. large) scales, the roughness exponent corresponds to an effective quenched (resp. thermal) noise [39]. The crossover length scale between the small-scale and the large-scale regime is expected to increase with the line velocity. The influence of the crack growth velocity on the scaling properties of fracture surfaces is a crucial test for the relevance of such an approach.

(ii) Larralde and Ball [40] and then Ramanathan and Fisher [41] used Linear Elastic Fracture Mechanics to derive a linear non-local Langevin equation within the hypothesis of slowly growing crack (elastostatic approximation). Their models both led to crack surfaces with a roughness increasing logarithmically with the scale, in contradiction with the experimental measurements.

(iii) Another class of models for fracture is the network models [42, 43] made of elastic beams, bonds, or electrical fuses with random failure thresholds. For all network approaches, bonds are supposed to model the material at a mesoscopic scale and the aim is to investigate the interrelation between disorder and

properties of the network such as fracture stress and damage spreading. The surprising result is that properties of the network are related to the system size by scaling laws involving non-trivial exponents independent of the precise distribution and of the microscopic aspects of the model. It was therefore suggested to model slow crack propagation in quasi-brittle materials.[10] One of the most studied models is the random fuse model since it leads to self-affine fracture surfaces. But a precise value of the roughness exponent is still an issue[44, 45]. Recently, large scale numerical simulations were carried out and a discrepancy in the self-affine exponent was found: Batrouni *et al.* reported $\zeta \simeq 0.62$ [44] while Räisänen *et al.* [45] observed $\zeta \simeq 0.40$. The results can be used as a very interesting guideline, but in order to compare with experiments, it is inevitable to consider the vectorial nature of elasticity.

(iv) Hansen and Schmittbuhl [46] suggested that the universal scaling properties of fracture surfaces are due to the fracture propagation being a damage coalescence process described by a stress-weighted percolation phenomenon in a self-generated quadratic damage gradient. They obtained a roughness exponent $\zeta = 0.80$ in apparent agreement with the experimental observations. Moreover, in this static model, crack surfaces are expected to be isotropic. This point will be investigated in detail in Chapter 2. The experimental observations reported in Chapter 2 question the relevance of such a model to describe the scaling properties of experimental fracture surfaces.

To summarize, every model leads to prediction on the scaling properties of fracture surfaces. In the following chapter, we study the morphology of experimental fracture surfaces of five different materials. This study will allow determining the relevant theoretical descriptions.

[10] Broken bonds can be present in a rather extended zone ahead of the main crack. To model brittle fracture, one should prevent that the bonds not immediately ahead of the main crack break.

Chapter 2

Morphology of fracture surfaces revisited

Contents

2.1 Materials and methods 20

2.2 Statistics of fracture surfaces 23

2.3 Anisotropy of fracture surfaces 28

2.4 Two-dimensional scaling properties of fracture surfaces 34

2.5 Physical interpretation 39

2.6 Concluding remarks 43

During the two last decades, physicists have focused on the properties of crack surfaces. Their roughness aroused such an attention because it is expected to reflect the failure mechanisms of materials. After the work of Bouchaud *et al.* [26], it was conjectured that fracture surfaces of disordered materials are self-affine and characterized by a universal roughness exponent $\zeta \simeq 0.8$. Extensive experimental investigations on many materials were then performed to test this conjecture (for example, see the review [47]). On the other hand, various statistical methods were developed in order to test the self-affine behavior of crack roughness and measure the roughness exponent with a higher and higher precision [48, 49]. Roughly, all these studies validated the first conjecture: Fracture surfaces are self-affine with a scaling exponent $\zeta = 0.8 \pm 0.05$ independent of the material.

In this chapter, we revisit the analysis of rough fracture surfaces. We use new methods that provide new insights on the scaling properties of cracks. At first, we study the distribution of height variation of the surface in order to investigate whether profiles extracted on crack surfaces are self-affine or multi-affine. Then, we show that the current description – with one roughness exponent – of the roughness of fracture surface is incomplete. A complete description of the crack roughness is shown to

require the use of a two-dimensional analysis. In particular, the fracture surface is observed to follow a Family−Vicsek scaling involving *two* scaling exponents.

In order to study the robustness of our observations, we have chosen to study five very different materials, broken under five different loading conditions[1]: Silica glass, an aluminum alloy, mortar, wood and AlPdMn quasicrystal. The new properties of fracture surfaces reported here will be shown to be independent of the material/loading conditions. The case of sandstone fracture surfaces that exhibit a surprisingly low roughness exponent $\zeta \simeq 0.5$ [2, 35] will be studied in the next chapter.

2.1 Materials and methods

In this section, we present in detail the experimental techniques used in this study. Fracture surfaces investigated here were obtained from various fracture tests, and scanned using various techniques. They are listed in Table 2.1. The crack growth velocity and the typical length scale of the features observed on the fracture surfaces are also given in Table 2.1. The research groups that performed the fracture tests and the scanning of the fracture surfaces are also listed in this Table. The experimental procedure is given in details in the following paragraphs for each material.

Silica glass : The experiments were performed by the "Fracture" Group (CEA Saclay) [33]. Fracture surfaces of silica glass were obtained by applying a DCDC (Double Cleavage Drilled Compression) to parallelepipedic ($5 \times 5 \times 25$ mm^3) samples under stress corrosion in mode I (see [54] for details). After a transient dynamic regime, the crack propagates at low velocity through the specimen under stress corrosion. This velocity was measured by imaging in real time the crack tip propagation at the free surface through Atomic Force Microscopy (AFM). In the stress corrosion regime, the crack growth velocity can be controlled by adjusting the compressive load applied to the specimen [15]. The protocol is then the following: (i) a large load is applied to reach a high velocity; (ii) the load is decreased to a value lower than the prescribed one; (iii) the load is increased again up to the value that corresponds to the prescribed velocity[2] and kept constant. This procedure allows to obtain for the same sample various crack growth velocities ranging from 10^{-6} m s^{-1} to 10^{-12} m s^{-1} corresponding to zones on the *post mortem* fracture surfaces which are clearly separated by visible arrest marks. Each arrest mark is numerated and its distance to the initiation is measured so that it is possible to identify *post mortem* the zone corresponding to

[1] But still in mode I.

[2] The value of the load F required to get the prescribed velocity is known because: (i) The applied stress intensity factor is given by $K_I = Fg(c)$ where $g(c)$ is a function of the crack length c and has been estimated through finite element simulations [55, 15] ; (ii) the relation between the applied stress intensity factor K_I and the crack growth velocity has been measured previously for silica glass sample [15].

the velocity to investigate on the fracture surface. A higher velocities zone is obtained near the hole where the crack initiated. During the dynamic transient regime, the crack velocity is estimated to be of the order of 10^2 m s^{-1}. The topography of these fracture surfaces is then measured through AFM with in-plane and out-of-plane resolutions of the order of 5 nm and 0.1 nm, respectively. To ensure that there is no bias due to the scanning direction of the AFM tip, each image is scanned in two perpendicular directions and the analyses presented hereafter are performed on the two sets of images. These images represent a square field of 1×1 μm (1024 by 1024 pixels).

Material	Fracture test	Scanning technique	Crack velocity	Length scale	Research group
Silica glass	DCDC	AFM	10^{-12} to 10^2 m s^{-1}	nm	"Fracture" Group (CEA Saclay) [33]
AlPdMn quasi-crystal	Cleavage	STM	rapid	nm	P. Ebert's Group (Jülich) [52, 53]
Aluminum alloy	CT	SEM and stereoscopy	rapid	μm	ONERA (Châtillon) [50, 51]
Mortar	TDCB	optical profilometer	quasi-static	mm	S. Morel's Group (Bordeaux) [30]
Wood	TDCB	optical profilometer	quasi-static	mm	S. Morel's Group (Bordeaux) [29]

Table 2.1: For each material studied, the type of fracture test and the scanning technique used are listed in the second and third column. DCDC, CT and TDCB mean Double Cleavage Drilled Compression, Compact Tension and Tapered Double Cantilever Beam, respectively. The crack growth velocity as well as the typical length scale of the features observed on the fracture surface are then given. The sixth column gives the research group that performed both the fracture test and the scanning of the fracture surface. Let us note that except for the quasicrystals fracture surfaces the propagation direction of the crack is known *a priori*.

Quasicrystal : Cleavage of quasicrystals and fracture surface scanning were performed by P. Ebert and co-workers at Jülich in Germany [52, 53]. Single quasicrystal samples of $Al_{70.5}Pd_{21}Mn_{8.5}$ were cleaved along two different cleavage plane in ultra-high vacuum. In order to measure the topography of the fracture surfaces, the samples were transferred to an Ultra Vacuum Scanning Tunneling Microscope (US-STM) without breaking the vacuum. As a consequence, the direction of crack propagation is *a priori* unknown. We will see in Section 2.3 that this direction can however be deduced *post mortem* from the 2D analysis of the scaling properties of the cleaved surfaces. The lateral resolution of the STM images (500×500) was estimated to be 0.1 nm and 0.2 nm parallel and perpendicular to the scanning direction, respectively.

Aluminum alloy : The fracture test was performed by E. Bouchaud (ONERA, Châtillon) and the scan of the fracture surface was achieved by J. Amman (ONERA, Châtillon) [50] and J.-L. Pouchou and co-workers (ONERA, Châtillon) [51]. Fracture surfaces of the commercial 7475 aluminum alloy were obtained from CT (Compact Tension) specimens, first precracked in fatigue and then broken under uniaxial mode I. In the tensile zone, the fracture surface has been observed with a scanning electron microscope at two tilt angles. High resolution surface height maps has been produced from the stereo pairs using the cross-correlation based surface reconstruction technique described in [50]. Two reconstructed images of the topography corresponding to two zones of the same fracture surface has been obtained and correspond to rectangular fields of 565×405 μm (512 by 512 pixels). The in-plane and out-of-plane resolutions are of the order of $2 - 3$ μm.

Mortar : The experiments on mortar and wood were performed by G. Mourot and S. Morel (LRBB, Bordeaux) [30]. Fracture surfaces of mortar were obtained by applying four points bending to a notched beam of square cross section leading to a mode I failure. The displacement is controlled during the test. The length of the beam is 1400 mm and its height and thickness are both equal to 140 mm. The topography of the fracture surfaces has been recorded using an optical profilometer. The maps is made of 500 profiles of 4096 points (pixel size: 20 μm) recorded along the direction of the crack front, perpendicular to the direction of crack growth. The first profile is close to the initial notch. Two successive profiles are separated by 50 μm along the direction of crack propagation. The lateral and vertical accuracy are of the order of 5 μm. A transient regime was observed on the fracture surfaces. On the first 10 mm of the crack propagation, corresponding to the first 200 profiles, the roughness of the profiles increases with the distance to the initial straight notch. A full description of the roughness in this region of the fracture surface is given in [30]. The present study focuses on the geometry of the surface far from the initial notch and the first 200 profiles are therefore systematically removed from the maps.

Wood : The experiments were performed by S. Morel [29]. Fractured wood surfaces were obtained from modified Tapered Double Cantilever Beam specimens (TDCB) subject to uniaxial tension with a constant opening rate leading to mode I failure (see [56] for details). The wood species used in the study is a Spruce (*Picea excelsa W.*) which is strongly anisotropic. The crack propagated along the longitudinal direction of the wood. As a result, the characteristic length scale of the elementary feature of the fracture surface is anisotropic: it is respectively of the order of a mm and of a few tens of micrometer in the longitudinal and transverse directions. These values correspond respectively to the length and the diameter of the wood cells. As a consequence, the height of the surface has been scanned by an optical profilometer over a 50×50 mm area with a higher resolution in the transverse direction (25 μm) than in the longitudinal one (2.5 mm): this map includes 50 profiles parallel to the crack front with 2048 points each. As for the mortar fracture surfaces, the maps of the wood fracture surfaces correspond to the zone far from the initial straight notch where the roughness is statistically stationary, *i. e.* approximately 50 mm from the initiation.

Visual features of the surfaces : In all four cases, the reference frame $(\vec{e}_x, \vec{e}_y, \vec{e}_z)$ is chosen so that $\vec{e}_x$ and $\vec{e}_z$ are respectively parallel to the direction of crack propagation and to the crack front. Figure 2.1 shows three-dimensional views of the fracture surfaces as observed in silica glass, AlPdMn quasicrystals, aluminum alloy, mortar and wood. These surfaces display striking visual differences: the in-plane (along x or z) and out-of-plane (along h) length-scales of the observed features strongly depend indeed on the considered material. They are respectively of the order of 50 nm and 1 nm for the silica glass surface, about 3 nm and 1 nm for quasicrystal, approximately 100 μm and 30 μm for aluminum, and 5 and 0.6 mm for mortar. The wood fracture surface is highly anisotropic: The typical in-plane sizes of the patterns are respectively 50 and 1 mm along the longitudinal (x-axis) and transverse (z-axis) directions and out-of-plane features have a typical height of 200 μm. Despite their apparent differences, thesesurfaces share common scaling properties to be discussed in the next paragraphs.

2.2 Statistics of fracture surfaces

Scaling of the 1D correlation function : Since the 80's and the pioneering work of Mandelbrot et al. [25], the roughness of fracture surface has been widely studied. These works have been motivated by the puzzling scaling invariance properties of these surfaces. Extensive experimental investigations have lead to the conclusion that fracture surfaces are self-affine, characterized by a universal roughness exponent $\zeta \simeq 0.8$ [26, 27]. A key consequence of this scale invariance is that the height−height correlation function defined as the standard deviation $\sigma_{\Delta h}(\Delta r) = \langle (\Delta h_{\Delta r})^2 \rangle_r^{1/2} =$

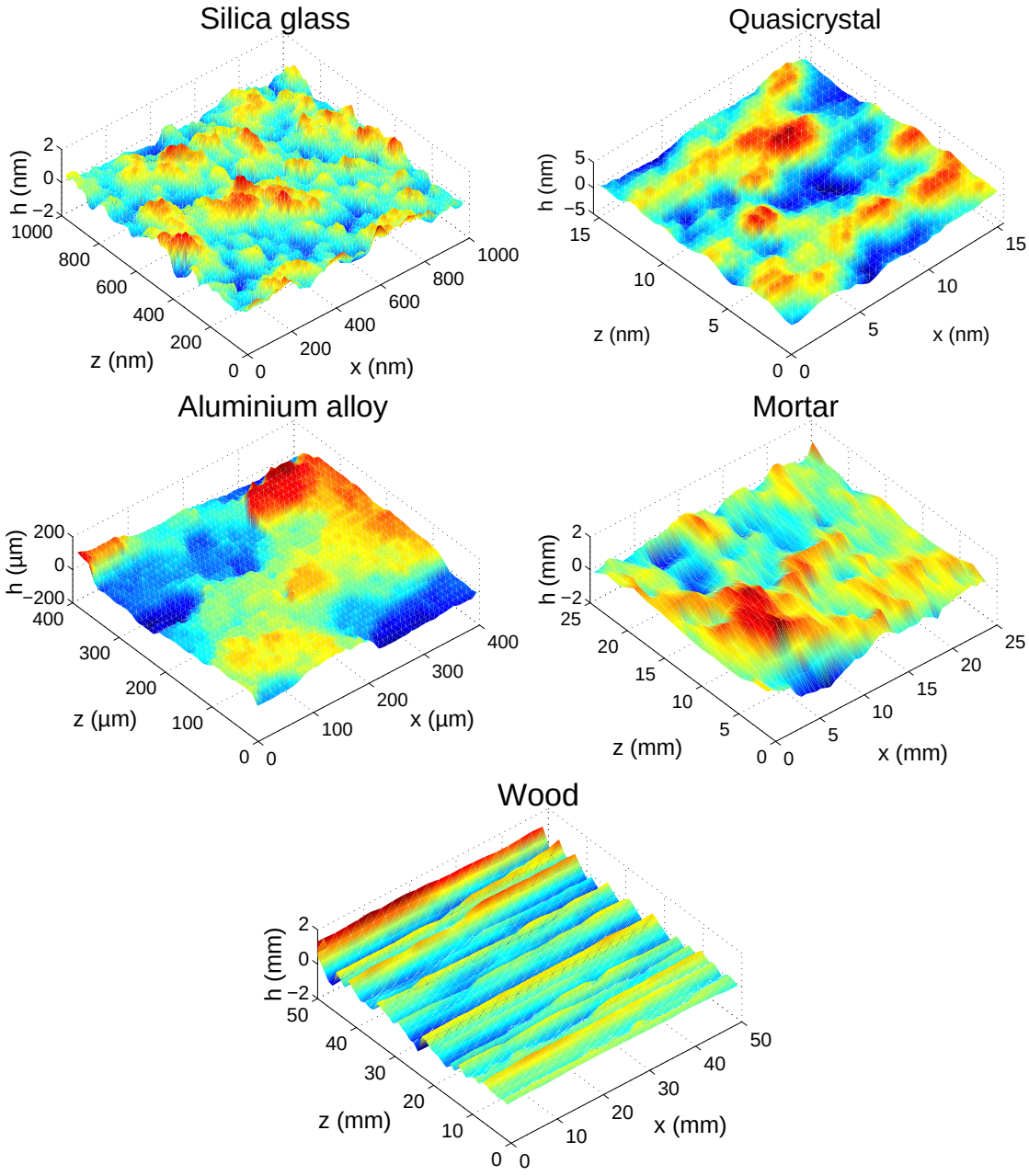


Figure 2.1: Topographic images of fracture surfaces of silica glass, AlPdMn quasicrystal, aluminum alloy, mortar and wood. Square fracture regions are represented here for the sake of clarity. The x-axis and z-axis correspond to the crack propagation direction and to the crack front direction respectively.

$\langle (h(r+\Delta r) - h(r))^2 \rangle_r^{1/2}$ of the distribution $\{\Delta h_{\Delta r}\}$ of height variation scales as

$$\frac{\sigma_{\Delta h}}{l} = \left(\frac{\Delta r}{l}\right)^{\zeta} \tag{2.1}$$

Here ζ is the roughness or Hurst exponent and l the topothesy, *i.e.* the length scale at which $\sigma_{\Delta h}$ is equal to Δr. Many other methods have been proposed to study the scaling properties of signals [57, 48, 49]. The choice of the height−height correlation function made here is motivated by the fact that this method is most efficient[3] when the signal is characterized by two self-affine regimes – or one regime and one saturation – which is the usual case for experimental signals.

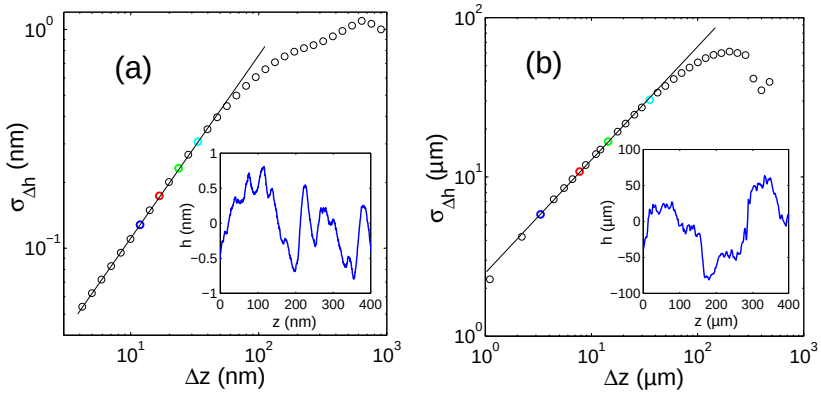


Figure 2.2: Height−height correlation function computed on profiles extracted along the z-axis of fracture surfaces of silica glass (a) and aluminum alloy (b). The straight lines correspond to power-law fits $\sigma = \ell_z^{1-\zeta}\Delta z^{\zeta}$ with $\zeta = 0.81$, $\ell_z = 0.58$ fm (a) and $\zeta = 0.74$, $\ell_z = 14$ μm (b).

Fig. 2.2 shows the evolution of the height−height correlation function computed on profiles extracted along the z-axis (perpendicular to the propagation direction) for silica glass and aluminum alloy fracture surfaces. A typical profile is given in the inset of the same figures. In a given range of Δz ranging from 4 to 40 nm for silica glass and from 2 to 35 μm for aluminum, σ is found to evolve as a power-law with Δz. This evolution is characterized by a roughness exponent corresponding to the slope of the power-law fit in the logarithmic representation of Fig 2.2 and found to be $\zeta = 0.81$ and $\zeta = 0.74$ for silica glass and aluminum respectively. These values are in agreement with the "universal" value $\zeta \simeq 0.8$ widely reported in the literature. The topothesy are measured to be $\ell_z = 0.58$ fm and $\ell_z = 14$ μm for silica glass and aluminum respectively. To summarize, the correlation function computed along the z-axis is found to be $\sigma_{\Delta h} = \ell_z^{1-\zeta}\Delta z^{\zeta}$.

[3]This method leads both (i) to physically relevant value of the crossover length scales and (ii) do not induce bias on the value of the exponents when two self-affine regimes are present on the same signal.

Distribution of height fluctuations : This result gives no hint of the actual statistical distribution of $\{\Delta h\}_{\Delta z}$ giving rise to such a scaling. In this part, we go beyond the sole computation of the roughness exponent and compute the statistical distribution for the fluctuations Δh of height of the fracture surfaces. This study is motivated by recent experimental results [58] reporting multi-affine scaling of crack surfaces obtained by rupture of a sheet of paper. In that case of failure of a 2D solid, one obtains crack lines resulting from the propagation of a point – the crack tip – in the materials. In the present study, the fracture surfaces result from the propagation of a crack front in a 3D solid. Although the two systems are quite different, it is of great interest to study the whole distribution of height variation and so the multi-affinity of fracture surfaces.

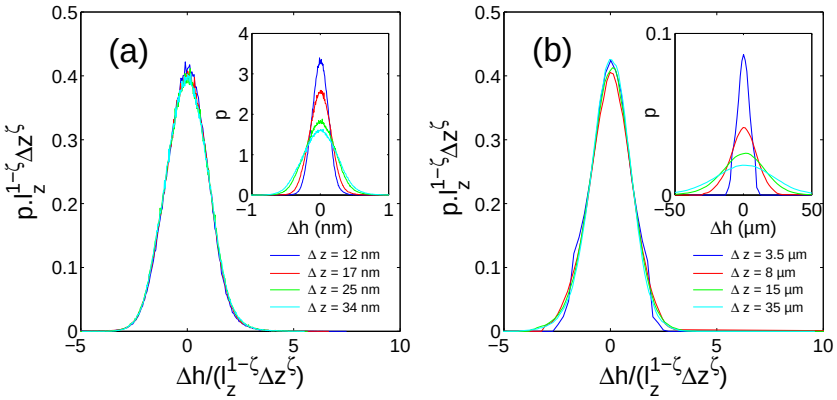


Figure 2.3: The insets show the distribution of the height fluctuations Δh for various values of Δz for fractured silica glass (a) and aluminum alloy (b) surfaces. The collapse of the curves was obtained using Eq. (2.2) with the values of the exponents ζ and topothesies ℓ_z measured from the calculation of the height−height correlation function (cf. Fig. 2.2).

We define the statistical distribution $P(\Delta h)$ of height variation $\Delta h(\Delta z)$ between two points distant of Δz along the z-axis. This distribution $P(\Delta h)$ is plotted in the insets of Fig. 2.3 for silica glass and aluminum alloy for various values of Δz corresponding each to a given color. The points corresponding to the standard deviation σ calculated for the same Δz values are plotted in the same color in Fig. 2.2. Using the values of ζ and ℓ_z calculated previously, it can be seen in the main graphs of these same figures that a very good collapse of the distributions can be obtained by dividing the abscissa by $\ell_z^{1-\zeta}.\Delta z^{\zeta}$ and multiplying the ordinates by $\ell_z^{1-\zeta}.\Delta z^{\zeta}$. After a normalization of the random variable Δh by the width of the distribution $\sigma_{\Delta h} = \ell_z^{1-\zeta}.\Delta z^{\zeta}$, all the normalized distributions corresponding to various Δz become the same. In other words:

$$P(\Delta h) = 1/(\ell_z^{1-\zeta}\Delta z^{\zeta}) \cdot g(\Delta h/(\ell_z^{1-\zeta}\Delta z^{\zeta}) \tag{2.2}$$

as long as Δz belongs to the self-affine regime. In other words, not only does the standard deviation display scale invariance, but also the whole distribution of height fluctuations and this scale invariance can be described through one single scaling exponent ζ.

The function g that corresponds to the collapse of all the normalized distribution does not depend on Δz. It is plotted in Fig. 2.4 in a semi-logarithmic representation. At first, it can be seen that even in this new representation, the collapse of the distributions corresponding to various values of Δz is rather good. The Gaussian distribution $p(x) = \frac{1}{\sqrt{2\pi}} e^{\frac{-x^2}{2}}$ with a standard deviation equal to unity is also plotted in Fig. 2.4. For small Δh values, the master curve g is rather well fitted by a Gaussian distribution. However, deviations to the Gaussian behavior can be observed in the tail of the distributions. No clear explanation of these deviations has been found yet.

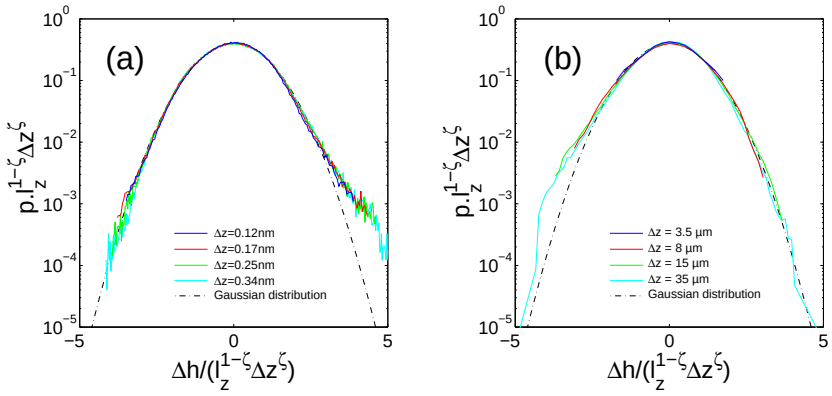


Figure 2.4: Normalized distribution of height fluctuations presented in Fig. 2.3 in a semi-logarithmic representation for fractured silica glass (a) and aluminum alloy (b) surfaces. The Gaussian distribution $p(x) = 1/\sqrt{2\pi} e^{-x^2/2}$ is represented as a dashed line.

Following the Eq. (2.2), once the roughness exponent and the topothesy are know, it is possible to give the evolution of the whole distribution of height fluctuation with the scale of study Δz. In other words, one exponent is sufficient to describe the scaling properties of the fracture surfaces studied (from Eq. (2.2), one can easily show that the n^{th} order moment of $P(\Delta h)$ scales as $\Delta z^{n \times \zeta}$). This study brings new insights into a currently widely debated question. In a recent study [58], it was reported that fracture surfaces of quasi-two-dimensional (2D) media (*e.g.* paper sheet) display multiscaling properties, in the sense that the n^{th} order moments of the height fluctuations over any distance Δr scale as a function of Δr with a characteristic exponent that depends nonlinearly on the order n of the moment. In other words, only one exponent is not enough to describe fully the statistical properties of the roughness of crack in paper sheet (2D medium). An analysis of profiles obtained on

3D granite samples also display multiscaling properties [28]. A multiscaling analysis were then performed by Santucci et al. [59] that shown that multiscaling occurs only at small length scales compared to the typical size of the disorder in the materials, both for 2D and 3D media. The current models of crack propagation proposed in the literature (elastic line based models as well as damage coalescence based models) do not predict such multiscaling properties of fracture surfaces. The study reported here on five different materials (the results on mortar, wood and quasicrystals are not shown but their distribution of height fluctuation scales also with a single exponent) is a strong argument in favor of mono-affinity of fracture surfaces in the investigated range of length scales.[4]

2.3 Anisotropy of fracture surfaces

Context and motivation : In the previous part, the statistical properties of the surface height parallel to the z-axis, perpendicular to the crack growth direction, have been shown to be fully described by a single scaling exponent, the roughness exponent ζ. From now on, we will focus on the standard deviation $\sigma_{\Delta h}$ (noted Δh for sake of simplicity) which is sufficient to estimate this roughness exponent and therefore the whole statistical properties of the profiles. In this section, we go beyond the analysis of profiles parallel to the z-direction and we study the statistics of surface height along other directions.

The scaling properties of fracture surfaces are usually believed to be isotropic [48, 35]. However, for surfaces obtained by shear fracture (mode II), it was reported in Ref. [60] that the scaling exponent measured on profiles parallel to the crack propagation was slightly smaller than for profiles along the perpendicular direction.

The analysis of such an anisotropy on samples obtained under tensile failure (mode I) is the central point of this paragraph. This point is crucial because, as we will see in Section 2.5, it will determine the kind of models developed to describe crack front propagation in heterogeneous materials. As reviewed in Section 1.2, the various competing theoretical approaches for failure of disordered materials lead to conflicting conclusions about the isotropy of fracture surfaces.

Scaling behavior parallel and perpendicular to the crack growth direction: In order to investigate the anisotropy of the experimental fracture surfaces, the 1D height−height correlation functions $\Delta h(\Delta z) = \langle (h(z+\Delta z, x) - h(z,x))^2 \rangle^{1/2}$ along the z direction, and $\Delta h(\Delta x) = \langle (h(z, x+\Delta x) - h(z,x))^2 \rangle^{1/2}$ along the x direction were computed for each material. They are represented in Figure 2.5.

[4]We will see in Section 3.4 that an "apparent" multiscaling is present at length scales smaller than the grain size in sandstone samples in agreement with the observations made in Ref. [59]. However, one can question the relevance of these observations made at a scale where the roughness of one individual grain/elementary microstructural feature becomes the dominant factor.

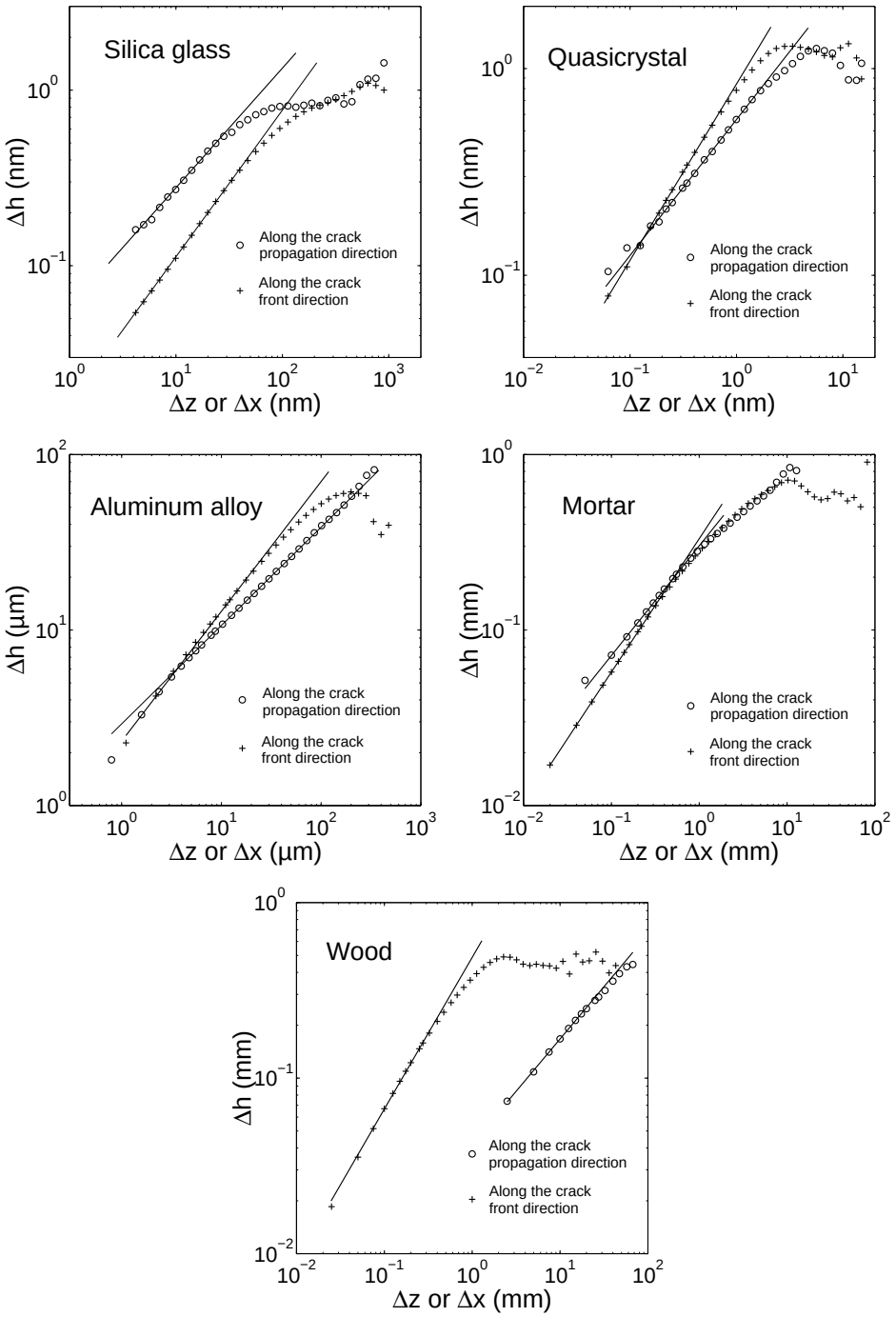


Figure 2.5: 1D height−height correlation functions measured parallel to the crack propagation direction and to the crack front for silica glass, quasicrystals, aluminum alloy, mortar and wood. The straight lines are power-law fits. The scaling exponents, corresponding to the slope of these lines, are listed in Table 2.2.

These curves indicate a clear dependence on the measurement direction although all profiles are self affine. Indeed, the height−height correlation functions $\Delta h(\Delta z)$ and $\Delta h(\Delta x)$ computed respectively along the crack front and crack propagation directions are found to scale as:

$$\frac{\Delta h}{\ell_z} = \left(\frac{\Delta z}{\ell_z}\right)^{\zeta} \quad \text{and} \quad \frac{\Delta h}{\ell_x} = \left(\frac{\Delta x}{\ell_x}\right)^{\beta} \tag{2.3}$$

where ζ and ℓ_z refer to the roughness exponent and topothesy measured along the direction of the crack front, while β and ℓ_x refer to the roughness exponent and topothesy measured along the crack growth direction. Along the crack front, the scaling exponent is found to be $\zeta \simeq 0.8$ irrespective to the nature of the material studied. This observation is fairly consistent with the "universal" value of the roughness exponent reported in the literature [26, 27, 61, 22]. Parallel to the crack front, the measured Hurst exponent β is significantly smaller, of the order of 0.6, irrespective of the nature of the material. The values of the scaling exponents ζ and β measured on the five materials are listed in Table 2.2.

	ζ	β	ℓ_z	ℓ_x
Silica glass	0.81 ± 0.04	0.64 ± 0.04	0.58 fm	1.7 pm
AlPdMn quasicrystal	0.81 ± 0.03	0.67 ± 0.05	0.32 nm	0.19 nm
Aluminum alloy	0.74 ± 0.04	0.57 ± 0.03	14 μm	5.6 μm
Mortar	0.76 ± 0.05	0.62 ± 0.05	12 μm	18 μm
Wood	0.79 ± 0.05	0.59 ± 0.05	18 pm	2.0 μm

Table 2.2: Scaling exponents and topothesies measured on profiles extracted on fracture surfaces of silica glass, quasicrystal, metallic alloy, mortar and wood. The exponent ζ and the topothesy ℓ_z corresponds to the value obtained after the analysis of profiles parallel to the crack front direction. β and ℓ_x corresponds to profiles extracted along the crack propagation direction. The error bars correspond to a confidence interval of 95% calculated from the various values of exponents measured on each profile studied.

On the other hand, the range of length scales on which the power-law behavior is measured does depend on the material studied. To select the range over which the scaling exponents are measured, we used the following procedure: The derivatives $\frac{\partial \log(\Delta h)}{\partial \log(\Delta z)}$ and $\frac{\partial \log(\Delta h)}{\partial \log(\Delta x)}$ are computed. A rather good plateau behavior is in general observed at smaller scales below the cut-off length scale. The correlation function is then fitted over a domain of length scales ranging from the resolution of the scanning apparatus up to this cut-off length scale. The vertical resolution of the apparatus has never been observed to be the limiting parameter that prevents a fit on smaller length scales. For the silica glass, the aluminum alloy and the quasicrystals, the lateral resolution is of the order of two pixels while it is smaller than one pixel for mortar and

wood. This size sets the lower bound of the power-law fit for each material. This procedure leads to self-affine domains that are observed to be roughly the same along the z and x-axis except for wood which has an anisotropic structure. For this material, the lower limits are a few tens of μm and a mm along the z and x-axis, respectively, and correspond to the dimensions of the wood cell.[5] The existence of these length scales creates a lower cut-off for the self-affine domains. It is remarkable that, despite the strongly anisotropic structure of the wood, the same scaling exponents as for isotropic materials are measured parallel and perpendicular to the crack growth direction, even though the length scales involved in these two directions are different.

As for the surface height along the z-axis, the profiles along the x-axis are monoaffine: Their description requires the use of only one single exponent β. This has been verified by computing the distribution of height fluctuation, using the same procedure as in Section 2.2.

In addition to the scaling exponents, the topothesies in both directions z and x were also measured. Their values are listed in Table 2.2 for the five materials studied. Presently, we do not know what select these topothesies. They provide information on the roughness amplitude. An interpretation of this quantity will be given in Section 4.2 for another kind of fracture surfaces. In this chapter, we will only use it because they will allow us to work with dimensionless quantities in order to compare the roughness properties of fracture surfaces of different materials irrespective of the various length scales involved in these experiments.

Scaling behavior along intermediate directions : It is crucial to note that pure power-law scaling is only observed along the directions x and z parallel and perpendicular to the crack growth direction. For instance, the 1D correlation function computed on an aluminum fracture surface along a transverse direction characterized by an angle of 30° with the z-axis is plotted on Fig. 2.6. To emphasize its peculiar scaling properties, the correlation function computed along the z and x-axis are also represented and all three are normalized by Δr^{β} with $\beta = 0.57$ as measured previously on this surface. As expected, $\Delta h(\Delta x)$ corresponding to the x-axis displays a plateau behavior after normalization. Then, $\Delta h(\Delta z)$ corresponding to the z-axis varies following a power-law characterized by the exponent $\zeta - \beta = 0.17$ after normalization until a decreasing due to the saturation of the correlation function observed in Fig. 2.2. The behavior of the normalized correlation function computed along the intermediate direction is more complex: It remains constant and then scales as a power-law with the same exponent $\zeta - \beta$. It means that along this transverse direction, the correlation function follows two distinct behaviors. At small scales, it evolves as a power-law characterized by the exponent β and, at larger scales, it evolves as another power-law characterized by the exponent ζ. We will show in the following that the

[5]The wood cells are oriented along the x-axis because the crack propagates along the longitudinal direction of the wood.

crossover length scale between these two regimes increases with the tilt angle, leading to pure scaling behavior only along the z and x-axis. Let us note that on Fig. 2.6, the anisotropy of the fracture surface is very clear. This anisotropy is emphasized by the normalization of the correlation function by Δx^{β} that results in a plateau behavior along the x-axis and a power-law behavior along the z-axis. In the following, another method based on 2D measurements will also emphasize the anisotropy.

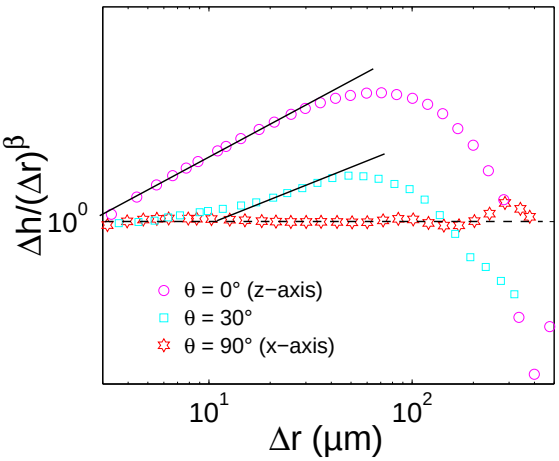


Figure 2.6: 1D normalized height−height correlation functions measured on an aluminum fracture surface for three directions corresponding to angles of 0°, 30° and 90° with the z-axis. The functions are normalized by $(\Delta r)^{\beta}$ with $\beta = 0.57$. The straight solid lines correspond to the power-law behavior with exponent $\zeta - \beta = 0.17$.

Application : The intrinsic scaling anisotropy of fracture surfaces suggests a method to determine the direction of the crack propagation from a *post mortem* analysis of the surface of a broken solid, as follows: Although intermediate directions θ exhibit a combination of the two scaling behaviors, let's fit the corresponding correlation function in coarse approximation by a single power-law characterized by an effective exponent $H(\theta)$ between β and ζ. In Fig. 2.7, the evolution of the effective exponent is plotted versus the direction of analyze for a quasicrystal fracture surface. $\theta = 0$ coincides here with the scanning direction of the STM tip used to study the surface. The angle θ where H is minimum (resp. maximum) coincides then with the direction of the crack propagation $\vec{e}_x$ (resp. the crack front direction $\vec{e}_z$). Using this methodology, it is possible to find the propagation direction of the crack leading to the fracture surface.

In addition to the previous studies presented here where the propagation direction of the crack was known *a priori*, we decided to perform a blind-test of this technique on fracture surfaces of an AlPdMn quasicrystal. The experiments were performed by P. Ebert and co-workers at Jülich in Germany [52, 53] while we performed the

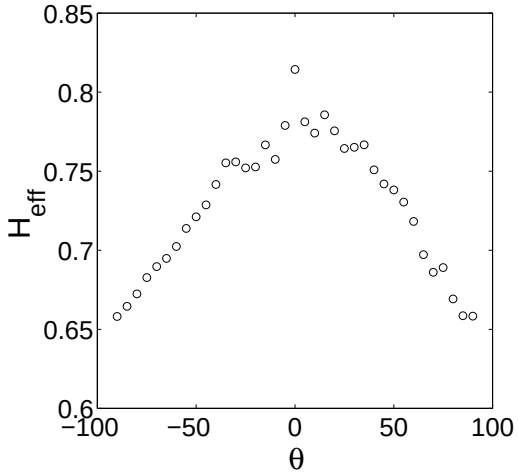


Figure 2.7: Variation of the effective Hurst exponent H measured along a direction making an angle θ with the z-axis. The maximum and minimum (at 0° and 90° respectively) of H coincide with the z and x-axis, *i.e.* the direction of crack propagation and the direction of the crack front respectively.

analysis of the fracture surfaces. The aim was to guess the propagation direction of the crack without knowing *a priori* the experimental procedure. These guesses were then sent to Ebert and co-workers that confronted it with their experimental procedure. We proceeded as follows: Two samples of quasicrystals were cleaved under ultra-vacuum (see Section 2.1 for details). For each sample, three images of the fracture surface are then recorded through STM measurement. The scanning direction of the STM tip was chosen in order to scan along the local minimum apparent slope of the surface to avoid rapid vertical motion of the tip. Thus, this direction is chosen independently of the propagation direction of the crack and can change from image to image. They then sent us the images without providing us with any additional information. We sent them back our guess for the propagation direction of the crack for each images. Knowing the experimental procedure, it was possible to show that our proposed propagation direction for the crack corresponded to an angle of $35° \pm 5°$ with respect to the sides of the cleavers irrespective to the STM image and so to the scanning direction. This result is a quite good agreement with what is expected from a cleavage experiment.[6] This result validates the method and confirms that the anisotropy measured on quasicrystal surfaces is not linked to a possible anisotropy induced by the scanning apparatus.

It is worth mentioning that this technique of analysis of fracture surfaces may have interesting appraisal application. Applied on various zones of a fracture surface

[6]In a cleavage experiment, the crack is expected propagating within a well-defined plane, but along an *a priori* unknown direction. However, the same fracture surface is expected to reveal the same crack propagation direction, irrespective to the scan direction, as it is observed here.

of a broken structure, this method allows the *post mortem* determination of the field of local orientation of crack propagation direction. Therefore, one can reconstruct the history of the process that led to the failure of a structure. This may have interesting applications in domains such as aeronautics or civil engineering. This led us to register a patent[62, 63].

2.4 Two-dimensional scaling properties of fracture surfaces

Motivation : The observation of the anisotropy of fracture surfaces raises a crucial question debated in [33] and [64]: Is this anisotropy a universal property of the fracture surface due to a physically relevant underlying phenomenon? Or is it a simple perturbation of the isotropic case and thus an experimental bias due to the choice of a particular fracture test configuration?

In this last case, the fracture surface might be described as an isotropic object with an additional anisotropic perturbation: this would lead to a roughness exponent that would vary continuously with the direction of analysis without any remarkable structure. In the former case, the whole anisotropic geometry of the fracture surface is expected to display universal properties that would be a signature of an underlying physical phenomenon. The analysis of profiles extracted along a random directions suggests that they are not self-affine, but display two distinct scaling behaviors (cf. Fig. 2.6). In order to study in detail the two-dimensional structure of the fracture surface roughness, the computation of the 1D correlation function only is not enough. A new approach based on the analysis of the 2D height−height correlation function $\Delta h(\Delta\vec{r}) = \langle (h(\vec{r}+\Delta\vec{r}) - h(\vec{r}))^2 \rangle_{\vec{r}}^{1/2}$ has therefore appeared to be necessary. This analysis should confirm the anisotropy measured by 1D technique and provides additional information on the 2D properties of fracture surfaces.

2D height−height correlation function : The observation of two pure scaling behaviors along the two different directions z and x of the fracture surface (see Section 2.3) suggests that the 2D height−height correlation function defined in the Cartesian frame ($\vec{e}_z$,$\vec{e}_x$) could be the appropriate quantity. This function Δh is defined as:

$$\Delta h(\Delta z, \Delta x) = \langle [h(z+\Delta z, x+\Delta x) - h(x,z)]^2 \rangle_{z,x}^{1/2} \tag{2.4}$$

The variations of correlation functions $\Delta h_{\Delta x}(\Delta z)$ corresponding each to a fixed Δx value are plotted as a function of Δz in Fig. 2.8 a for an aluminum fracture surface. For the smallest values of Δx, the correlation function Δh varies as Δz^{ζ} with $\zeta = 0.74$ in perfect agreement with the result obtained for the 1D correlation function along the z-axis. The other curves corresponding to larger values of Δx display a plateau regime

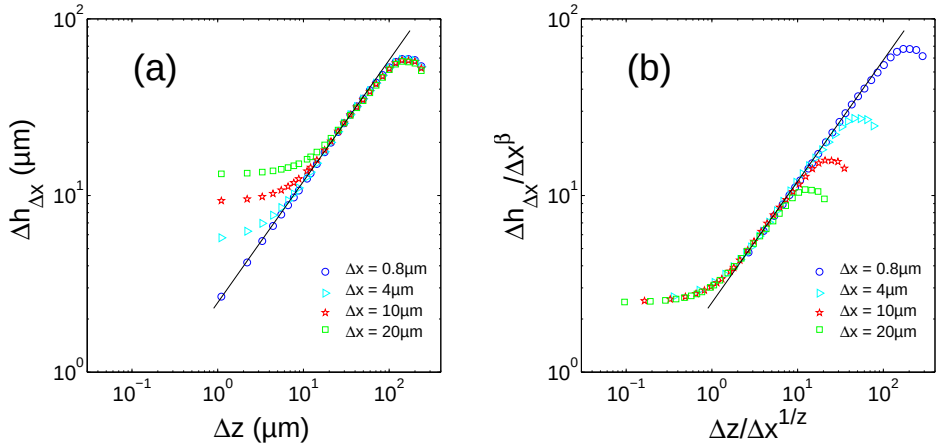


Figure 2.8: (a): 2D correlation function variations computed on a aluminum alloy fracture surface. The straight line correspond to a power-law fit with $\zeta = 0.74$. (b): The data collapse is obtained from Eq. (2.5) using $\beta = 0.58$ and $z = 1.26$.

followed by a power low variation also characterized by the scaling exponent ζ. The crossover length scale between the two regimes increases with Δx. More precisely, it varies as $\Delta x^{1/z}$ while the plateau value varies as Δx^{β}. Indeed, by dividing the abscissa by $\Delta x^{1/z}$ with $z = 1.26$ and the ordinates by Δx^{β} with $\beta = 0.58$ as shown in Fig. 2.8 b, the curves collapse onto a single master curve characterized by a plateau regime and then a power-law regime with exponent ζ. The part of the curves that correspond to Δz values larger than the upper limit of the self-affine domain of the 1D correlation function plotted in Fig. 2.2 does not collapse. The curves corresponding to Δx values that do not belong to the self affine domain of the 1D correlation function $\Delta h(\Delta x)$ does not collapse either (they are not represented here). In other words, as long as Δx and Δz values belong to the self-affine domains:

$$\begin{aligned} &\Delta h(\Delta z, \Delta x) \sim \Delta x^{\beta} f(\Delta z/\Delta x^{1/z}) \\ &\text{where} \quad f(u) = \begin{cases} 1 & \text{if u}\ll 1 \\ u^{\zeta} & \text{if u}\gg 1 \end{cases} \end{aligned} \tag{2.5}$$

The following procedure is then applied to the fracture surface: 2D correlation functions $\Delta h_{\Delta x}(\Delta z)$ are computed for Δz and Δx values belonging to the self-affine domain as measured in Fig. 2.5. These functions are represented in the insets of Figure 2.9 for the five materials studied. The values of β and z that optimize the collapse of the curves by normalizing the abscissa and the ordinates by $\Delta x^{1/z}$ and Δx^{β} respectively are then computed. It can be seen in the main graphs of Fig. 2.5 that a very good collapse is obtained. The resulting master curve is characterized by a plateau region and followed by a power-law variation of exponent ζ.

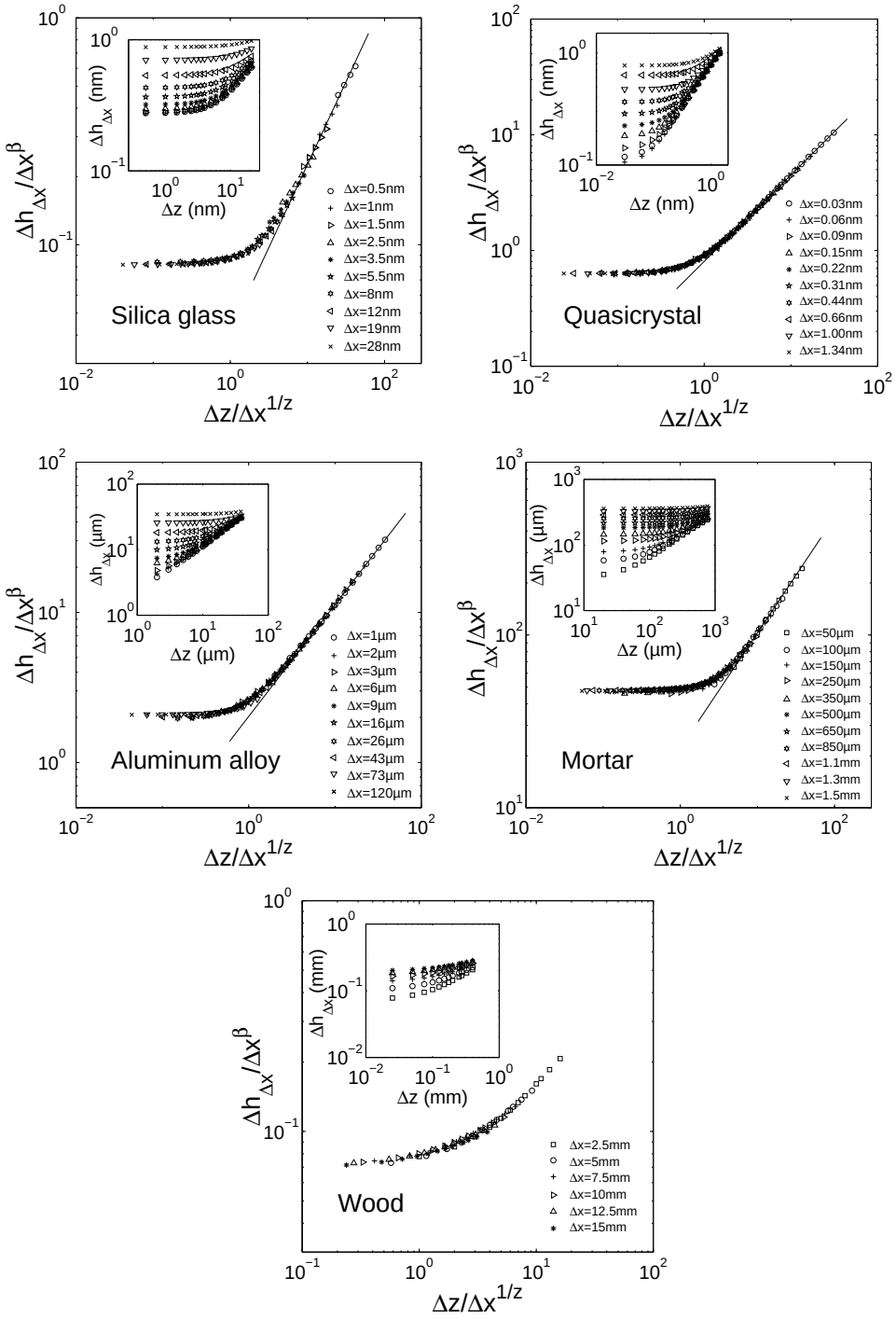


Figure 2.9: Normalized 2D height−height correlation function variations with Δz for various values of Δx for silica glass, AlPdMn quasicrystals, aluminum alloy, mortar and wood. The data collapse was obtained from Eq. (2.5) using exponents reported in Tab. 2.3.

The exponents β and z which optimize the collapse, and the ζ exponent determined thereafter by fitting the large scale regime followed by the master curve are listed in Table 2.3. The three exponents are found to be $\zeta \simeq 0.76 \pm 0.03$, $\beta \simeq 0.61 \pm 0.04$ and $z \simeq 1.23 \pm 0.05$, independent of the material and of the crack growth velocity over the whole range from ultra-slow stress corrosion fracture propagation (picometer per second) to rapid failure (several meters per second). They are therefore conjectured to be *universal*.

	ζ	β	z	ζ/β
silica glass	0.77 ± 0.03	0.61 ± 0.04	1.30 ± 0.15	1.26
AlPdMn quasicrystal	0.76 ± 0.03	0.65 ± 0.04	1.20 ± 0.08	1.17
aluminum alloy	0.75 ± 0.03	0.58 ± 0.03	1.26 ± 0.07	1.29
mortar	0.71 ± 0.06	0.59 ± 0.06	1.18 ± 0.15	1.20
wood	0.79 ± 0.05	0.58 ± 0.05	1.25 ± 0.15	1.36
average	0.76 ± 0.03	0.61 ± 0.04	1.23 ± 0.05	1.25

Table 2.3: Scaling exponents measured from the calculation of the 2D correlation function (see Eq. (2.5)) on fracture surfaces of silica glass, AlPdMn quasicrystals, metallic alloy, mortar and wood. ζ, β, z and ζ/β are respectively the roughness exponent, the growth exponent and the dynamic exponent z while the fourth column contains the ratio of ζ to β. Error bars are computed from the values of the exponents measured on the various local height maps studied.

Comparing Table 2.2 and Table 2.3, one observes that the exponents ζ and β depend slightly on the method used here (computation of the 1D or 2D correlation function). The computation of the 2D correlation function involves a larger number of data and should lead therefore to slightly more accurate values of the scaling exponents.

The ratio ζ/β, measured from the 2D correlation function, is given in the fourth column of Table 2.3. It is worth noting that the exponent z satisfies the relation $z = \zeta/\beta$. This makes perfectly coherent the 1D and 2D measured scaling properties of the fracture surfaces as given in Eq. (2.3) and (2.5).

Finally, the results presented in this paragraph confirm the anisotropies obtained thanks 1D measurements. The best collapse of the curve that can be obtained under the condition $z = 1$ (that corresponds to $\zeta = \beta$, *i.e.* to an isotropic surface) is shown in Fig. 2.10 for an aluminum fracture surface. It appears clearly that the best collapse is obtain for $z = 1.26$ as shown in Fig. 2.9.

Crossover function : Let us now look more closely at the crossover function $f(u)$ involved in the 2D correlation function for the five materials. Its asymptotic behavior $u \to 0$ and $u \to \infty$ was shown to be universal: It exhibits a plateau regime at small scales and a power-law regime with a scaling exponent $\zeta \simeq 0.75$ at large scales

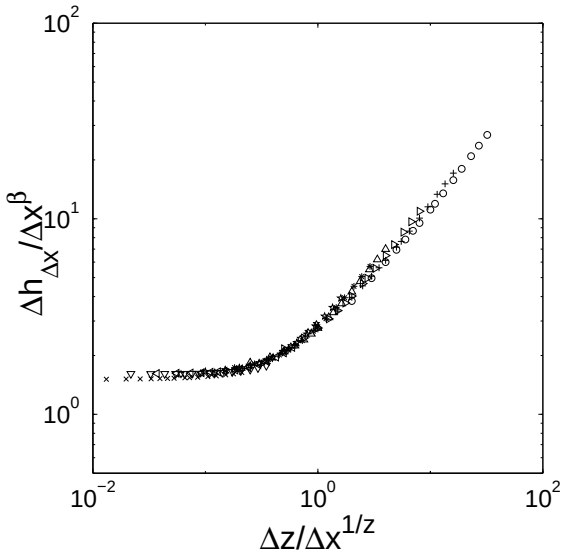


Figure 2.10: Normalized 2D height−height correlation function for an aluminum fracture surface under the condition $z = 1$ corresponding to an isotropic surface. The collapse is found clearly better if the value $z = 1.26$ is chosen as in Fig. 2.9. This is an additional proof of the anisotropy of fracture surfaces.

(see Eq. (2.5)). In order to compare *quantitatively* the crossover function for different materials, one needs to define dimensionless variables because the latter involve length scales that depend crucially on the material considered. Using the topothesies ℓ_z and ℓ_x defined in Eq. (2.3), the 2D correlation function can be rewritten:

$$\Delta h(\Delta z, \Delta x) = \ell_x (\frac{\Delta x}{\ell_x})^{\beta} f[(\frac{\ell_z}{\ell_x})^{1/\zeta} \frac{(\frac{\Delta z}{\ell_z})}{(\frac{\Delta x}{\ell_x})^{1/z}}]$$
$$\text{where} \quad f(u) = \begin{cases} 1 & \text{if u}\ll 1 \\ u^{\zeta} & \text{if u}\gg 1 \end{cases} \tag{2.6}$$

In other words, introducing the topothesies allows to replace all the signs $\sim$ by signs $=$, and consequently to qualitatively compare the structure functions measured in the various materials. Assuming that the scaling properties of the 2D correlation function given in Eq. (2.5) are satisfied, the form given in Eq. (2.6) is the only one compatible with the definition of the topothesies given in Eq. (2.3). For various values of Δz and Δx, $f = \Delta h/(\ell_x.\frac{\Delta x}{\ell_x})$ is plotted in Fig. 2.11 as a function of the dimensionless variable $u = (\frac{\ell_z}{\ell_x})^{1/\zeta} \frac{(\frac{\Delta z}{\ell_z})}{(\frac{\Delta x}{\ell_x})^{1/z}}$ using the values of the topothesies listed in Table 2.2 and the exponents $\zeta = 0.76$ and $z = 1.23$ corresponding to the mean of the exponents measured on the various materials. f has been plotted for silica glass, quasicrystal, aluminum alloy and mortar fracture surfaces. The crossover function is

observed to be independent of the material, not only in the plateau and power-law corresponding to $u \ll 1$ and $u \gg 1$, but also in the crossover domain, *i.e.* for $u \sim 1$. The crossover function calculated on the wood fracture surface is not represented in Fig. 2.11. Its shape is observed to be slightly different in the crossover domain. The highly anisotropic microstructure of the wood may account for this observation.

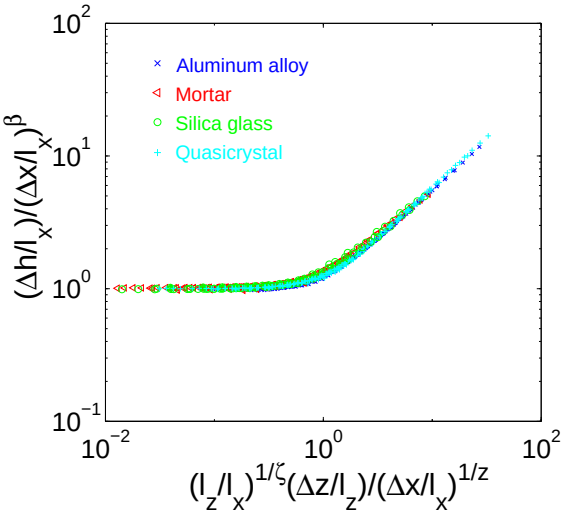


Figure 2.11: Scaling function f involved in Eq. (2.6) and measured on four different materials.

2.5 Physical interpretation

In this section, we give the physical interpretation of the very specific 2D scaling properties of fracture surfaces. In particular, we will show a new representation of the 2D correlation function (represented in Fig. 2.9) that reveals more clearly the physical meaning of its scaling (given in Eq. (2.5). This will lead us to give the physical sense of the second "universal" exponent measured on fracture surfaces, *i.e.* the exponent $z \simeq 1.2$. The implication of the 2D scaling properties of fracture surfaces on the models of failure will then be discussed.

Family−Vicsek scaling of fracture surfaces : At first, let us return to the shape of the 2D height−height correlation function. Figure 2.12 a displays a color scale representation of Δh in the $(\Delta z, \Delta x)$ plane for the fractured aluminum alloy surface. The function Δh is normalized by Δx^β and logarithmic scales are used to emphasize the anisotropy of the power-law scaling. This representation clearly demonstrates two distinct behaviors of the 2D correlation function depending on the orientation of the vector $\vec{AB}$ of components $(\Delta z, \Delta x)$.

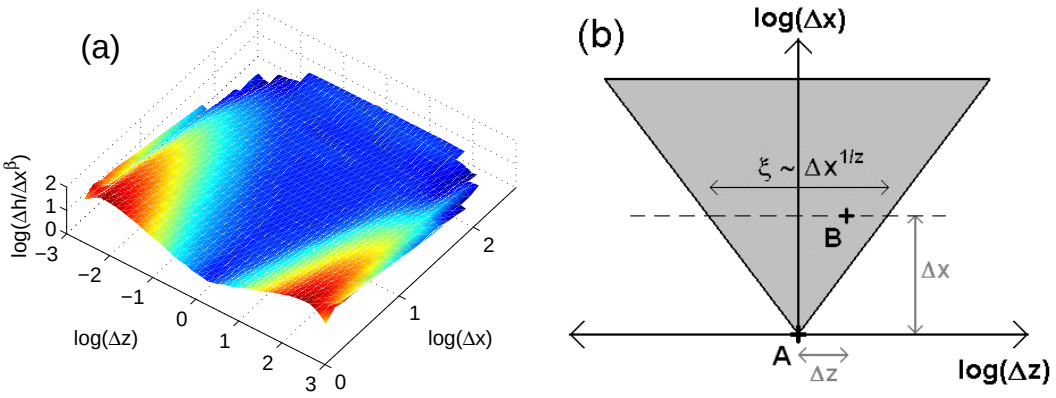


Figure 2.12: (a): 2D representation of the height−height correlation function for an aluminum fracture surface (Δh is normalized by Δx^β with $\beta = 0.58$). (b): Domains of different types of variation of the height−height correlation function in the $(\Delta z, \Delta x)$ plane. The grey zone corresponds to a height−height correlation function varying as $\Delta h \propto \Delta x^\beta$.

If $\vec{AB}$ lies within the grey region in Figure 2.12 b (corresponding to the blue domain in Figure 2.12 a), the 2D correlation function scales as Δx^β and does not depend on Δz. In formula 2.5, this correspond to the regime where $u = \Delta z/\Delta x^{1/z} \ll 1$, and so f(u)=1. The straight boundaries of this domain in these logarithmic coordinates indicate that its width ξ (Fig. 2.12 b) increases following a power-law $\xi \propto \Delta x^{1/z}$ where $z \simeq 1.2$. In other words, from any given point A of the fracture surface, a domain where the 2D correlation function scales as Δx^β develops over a width $\Delta z = \xi$ increasing as $\Delta x^{1/z}$ (the crack propagates parallel to x). Outside of this domain, the 2D correlation function depends only on Δz. In formula 2.5, this corresponds to the regime where $u = \Delta z/\Delta x^{1/z} \gg 1$, and so $f(u) = u^\zeta$.

Considering now the simple following scenario, we give the physical meaning of the development of this correlation domain (represented in grey in Fig. 2.12 b) from any point of the fracture surface: Let's consider a line, a straight crack front, propagating in a 3D space. The fracture surface is then the successive positions of the crack line. For the sake of simplicity, a constant crack velocity will be assumed, x and t being thus proportional. Let's assume that the front is perturbed at a given point A inducing a local out-of-plane displacement (along h, perturbation that will be then observed on the fracture surface) at time t=0. In agreement with the experimental observation of the development of a correlation cone in front of any point of the fracture surface, this perturbation will have repercussions on the resulting fracture surface in a zone of width $(\Delta x)^{1/z}$ where Δx is the distance to the point A, as represented in Fig. 2.12. This can be simply understood by considering that the information represented by the perturbation can propagate along the crack line as the crack propagates. More precisely, the information will propagate over $\Delta z \sim t^{1/z}$ along the crack line during

time t leading to a correlation domain $\Delta z \sim \Delta x^{1/z}$ since t is proportional to Δx.

This anomalous "diffusion" like process – very different from the classical diffusion process for which $\Delta z \sim \sqrt{t}$ – along a line has been widely studied theoretically and referred to as kinetic roughening processes [65]. The latter appears for example when an elastic line (of minimal energy when it is straight) is perturbed by an external disorder which roughens its profile. The competition between these two antagonist effects can be described in the theoretical framework of an elastic manifold driven in a random medium. The transient roughening development of a line $h(z,t)$ starting from an initially straight line $h(z,t=0)=0$ is generally studied. It is characterized by a 1D height−height correlation function $\Delta h(\Delta z,t)$ scaling as [65]:

$$\begin{aligned} &\Delta h(\Delta z,t) = t^{\beta} g(\Delta z/t^{1/z}) \\ &\text{where} \quad g(u) \sim \begin{cases} u^{\zeta} & \text{if u}\ll 1 \\ 1 & \text{if u}\gg 1 \end{cases} \end{aligned} \tag{2.7}$$

where ζ, β and z refer to the roughness, growth and dynamic exponents respectively. Signature of this roughening scaling can also be found in the steady state regime reached at long times when the mean roughness of the line remains constant even though it fluctuates. In this regime, the 2D height−height correlation function $\Delta h(\Delta z,t)$ is expected to scale as [39, 38]:

$$\begin{aligned} &\Delta h(\Delta z,\Delta t) = \Delta t^{\beta} f(\Delta z/\Delta t^{1/z}) \\ &\text{where} \quad f(u) \sim \begin{cases} 1 & \text{if u}\ll 1 \\ u^{\zeta} & \text{if u}\gg 1 \end{cases} \end{aligned} \tag{2.8}$$

which is exactly the scaling law (2.5) followed by the experimental surfaces after the time t has been replaced by coordinate x parallel to the crack propagation. This so called Family−Vicsek scaling [66], provides a rather strong argument in favor of models like [36, 41, 67, 68] that describe the fracture surface as a juxtaposition of successive positions of the crack front – modeled as a pseudo elastic line – moving through materials with randomly distributed local toughness. In this scenario, the Hurst exponents $\zeta \simeq 0.75$ and $\beta \simeq 0.6$ measured along the crack front direction and that of crack propagation respectively coincide with the roughness and the growth exponents as defined within the framework of elastic string models [65]. Let us note moreover that in such models, the dynamic exponent z is expected to be related to ζ and β through $z = \zeta/\beta$ [66]. This leads to a value of $z = 1.2$ in perfect agreement with the value measured experimentally.

Physical meaning of the scaling exponents : Finally, we can give the physical meaning of these three exponents: The roughness exponent $\zeta \simeq 0.75$ characterizes the geometry of the fracture surface perpendicularly to the crack propagation direction.

It furnishes information on the static geometrical properties of the crack front. The second independent exponent $z \simeq 1.2$ characterizes the way a relief on the crack front "diffuses" along the line when it propagates in the material. On a general manner, the exponent z furnishes information on the dynamical properties of the elastic line in motion. However, we will see in chapter 4 that this dynamical exponent z measured on the fracture surface gives no hint on the local velocities of a crack front propagating in a solid. To be more precise, we will show in Section 4.1 that the properties of the fracture surface – the trajectory of the crack front – and its dynamical properties – its local velocity – are two independent problems. Finally, the third exponent, $\beta = \zeta/z \simeq 0.6$, characterizes the fracture surface morphology along the direction of propagation. The value of these experimental scaling exponents as well as the universal shape of the crossover function will be crucial in the following to discriminate between the various models of crack propagation.

Implications on the models of fracture : Let us discuss now the implications of the two-dimensional scaling of fracture surfaces on the various models of fracture suggested in the literature. The observation of the Family−Vicsek scaling for all the fracture surfaces investigated represents a rather strong argument in favor of two of the four classes of models put forward to explain the fracture surface morphology and reviewed in Section 1.2. For the kind of models published in Refs. [46] and referred as (iv) in this section, fracture surfaces are suggested to result from a damage coalescence process. Whenever no crack front can be defined, the fracture surface is expected to be isotropic. As proposed in [64], a slight anisotropy could however be observed, but it would be induced by possible geometrical constraints and would not reflect an underlying relevant physical phenomenon.[7] In other words, the fracture surfaces resulting from this kind of models would not display Family−Vicsek scaling. For the models published in Refs. [42, 43] and referred as (iii) in section 1.2, this question has not been directly addressed yet. But to our knowledge, none of the simulations of failure in 3D bond networks led either to anisotropic surfaces or to Family−Vicsek scaling. In the types of models published in Refs. [36, 68] and [40, 41], and referred as (i) and (ii) in Section 1.2, cavities and microcracks – that are allowed in the other models – are neglected and the path followed by the crack front through the defects of the material is suggested to explain the full fracture surface morphology. In that case, fracture surfaces are expected to be anisotropic and characterized by a Family−Vicsek scaling. Even though damage cannot be neglected to explain the scaling of fracture surfaces reported here (see chapter 4), the observation of a Family−Vicsek scaling irrespective of the various materials studied and the various geometries used suggests that the latter approach is more suitable to reproduce our

[7] In a similar way, turbulence which is an intrinsically isotropic process has been observed to display slight anisotropic properties in experiments where boundary conditions favored a particular direction. But this anisotropy *is not* characterized by a Family−Vicsek scaling.

experimental observations. In other words, the two-dimensional scaling of fracture surfaces bring a strong argument in favor of models (i) and (ii).

Another remarkable property of fracture surfaces will help us to identify the relevant theoretical approach to describe failure of disordered materials: Silica glass fracture surface obtained from a broad range of crack growth velocities in the quasi-static regime limit (from 10^{-12} m s^{-1} to 100 m s^{-1}) have been investigated. No influence of the velocity on the value of the scaling exponents has been observed. We will see in Chapter 4 that only the upper cut-off length is influenced by the crack growth velocity. This experimental observation questions the scenario proposed in Refs. [36] and referred to model (i) in Section 1.2. In these studies, the roughness of fracture surfaces is interpreted as resulting from a pinning/depinning transition of the crack front within the microstructural obstacles of the material. In these models, two kinds of scaling exponents were predicted: At small scales, ζ_{quenched} was expected to result from a quenched noise due to the microstructural obstacles present in the material whereas at larger scales, ζ_{thermal} was expected to result from an effective thermal noise induced by the finite crack growth velocity as predicted in pinning/depinning models [39]. The crossover length between both regimes is also expected to increase with the crack growth velocity. This was observed on $TiAl_3$ based metallic alloy fracture surface as well as for soda-lime glass [22] where ζ_{quenched} was measured to be of the order of 0.5 and $\zeta_{\text{thermal}} \simeq 0.8$ at small and large scales respectively. In this present work, no influence of the crack growth velocity was observed in a very broad range of crack growth velocity (14 decades) on another amorphous material. This questions the universality of such observations and the validity of the pinning/depinning scenario. The observation of a self-affine regime characterized by $\zeta \simeq 0.8$ until the atomic scale on fractured quasicrystal surfaces is an additional argument that questions the existence of a second universal small roughness exponent at small scales on fracture surfaces.

The observation of (i) the Family−Vicsek scaling of fracture surfaces and (ii) the robustness of their scaling properties with respect to the crack growth velocity has brought precious information on the relevant theoretical approach: To describe failure in disordered materials, pinning/depinning scenarios and damage coalescence processes appears limited. At the opposite, models based on the Linear Elastic Fracture Mechanics and that describe crack surfaces as solution of a Langevin equation [40, 41] reproduce these two properties. Unfortunately, they do not lead to the experimental value of the scaling exponents. We will explain the reasons of this discrepancy in Section 4.1 and will propose an alternative model leading to their correct value.

2.6 Concluding remarks

In this chapter, the statistical properties of five very different fracture surfaces have been investigated. The main experimental results can be summed up as follows:

(i) Profiles parallel and perpendicular to the crack growth direction are self-affine,

in fact they are perfectly mono-affine. They are fully described by the value of their self-affine exponent: $\zeta = 0.76 \pm 0.04$ and $\beta = 0.61 \pm 0.04$ in the crack front direction and the crack growth direction respectively. The value of these exponents depends very weakly on the material, the crack growth velocity, the loading conditions and the fracture test geometry in the experimental ranges studied. Their value is conjectured to be universal.

(ii) In all the experimental cases studied, the 2D height−height correlation function computed in the set of coordinates parallel to the crack front and the propagation directions follow a specific shape given by Eq. (2.5) referred to as Family−Vicsek scaling. Among other implications, this scaling implies that profiles extracted along a direction that is neither the crack front direction nor the crack propagation direction are *not* self-affine.

(iii) The various scaling properties of the correlation function are universal: the three scaling exponents and the crossover function (if the material has an isotropic microstructure) do not depend on the three following parameter: the material, the crack velocity and the geometry of the fracture test.

(iv) These properties of fracture surfaces have led us to identify the relevant approach for future theoretical investigations of crack propagation in disordered materials (a model based on the Linear Elastic Fracture Mechanics describing the toughness of the disordered material as an uncorrelated noise as in Refs. [40, 41]; see Chapter 4) and to eliminate other ones (pinning/depinning transition [36, 22], damage coalescence process [46]). It is worth noting that weakly disordered materials have been studied here. Failure of strongly disordered materials could lead to a different fracture surface morphology with, in particular, isotropic properties. Let us note also that, without the presence of a notch used in all our experimental situations, damage spreading would have been larger. In these other cases, a damage coalescence approach could capture the whole physics of the failure process as suggested by Hansen and Schmittbuhl [46] and anisotropic geometrical conditions could induce a slightly non-universal anisotropy of fracture surfaces as predicted in Ref. [64] by Bouchbinder, Procaccia and Sela.

While our analysis have mainly focus on the universal properties of fracture surfaces, an important feature of their morphology has been shown to depend crucially of the nature of the material: The upper bound of the self-affine domain.[8] Indeed,

[8]The lower bound of the self-affine domain not been studied. Indeed, we were in most cases limited by the resolution of the scanning technique. However, for the STM images (atomic resolution) of fracture surfaces of quasicrystal, self-affine behavior of the roughness were observed down to the atomic scale. This suggests that in the general case, self-affine behavior with exponents $\{\zeta \simeq 0.75; \beta \simeq 0.6\}$ exists down the atomic scale.

it was observed to vary from some nanometers in quasicrystal or silica glass to some millimeters in mortar and wood. The mechanisms that set this length scale will be investigated in the following. This material dependent length scale will be proved to be crucial to capture the physics of fracture of heterogeneous materials.

But at first, we investigate in the following chapter the scaling properties of fractured porous materials for which a surprisingly low roughness exponent $\zeta \simeq 0.4 - 0.5$ has been recently reported [2, 35].

Chapter 3

Low roughness exponents of fractured porous material surfaces

Contents

3.1 Materials and methods 47

3.2 Fracture surfaces of glass ceramics 52

3.3 Roughness amplitude 58

3.4 Morphology of fractured sandstone surfaces 63

3.5 Concluding remarks 70

In the previous chapter, morphology of fracture surfaces has been studied. It was observed that their scaling properties can be described by two independent "universal" scaling exponents $\zeta = 0.76 \pm 0.03$ and $z = 1.23 \pm 0.05$. But somehow, the robustness of their scaling behavior makes difficult the investigation of its physical origin. However, in a recent study, Boffa *et al.* reported in Ref. [2] a surprisingly low roughness exponent $\zeta \simeq 0.45$ on fractured sandstone surfaces. Understanding why sandstone surfaces display such a scaling and why the other materials studied in Chapter 2 display other one is a quite interesting challenging: It would certainly help us to identify the physical origin of their self-affine geometry.

The observation of a low exponent on sandstone surfaces was interpreted as a signature of the intergranular propagation of the crack between the cemented grains that composed it. On the other hand, an transgranular rupture was suggested to lead to $\zeta \simeq 0.75$ [2]. To test this scenario, we will study artificial sandstone obtained by sintering of glass beads and referred as glass ceramics. Despite the wide range of porosities investigated – from 3 % to 26 % –, fracture surfaces have been observed to display the same scaling properties, characterized by the roughness exponent $\zeta = 0.40 \pm 0.03$ – perpendicularly to the crack growth direction. At the opposite, the amplitude of the roughness varies considerably with the porosity ϕ : It is observed to

be roughly proportional to ϕ. We will show that this result leads to the conclusion that the fracture mode in glass ceramics with low porosity is transgranular while a high porosity implies an intergranular fracture, without, however, any effect on the value of the roughness exponent. In addition to the broad range of porosities investigated, two sets of bead diameter and various crack growth velocities have been studied to determine to what extent this apparent "second class" of fracture surfaces with $\zeta \simeq 0.4$ is robust to system changes. Finally, following the same approach than in the chapter 2, we will study the two-dimensional scaling properties of fracture surfaces of glass ceramics. They are also observed to be anisotropic, but characterized by two different "universal" scaling exponents $\zeta = 0.40 \pm 0.03$ and $\beta = 0.48 \pm 0.05$ – corresponding to the crack front and the crack growth direction, respectively.

In the following section, the geometry of fractured sandstone surfaces are studied. Their scaling properties are observed to be quite similar to those of glass ceramics. On the other hand, the influence of sample width is systematically studied. We observe that only the upper bound of the self-affine domain is changing. The latter increases linearly with the sample width L and the roughness at this scale evolves as L^{ζ} with $\zeta \simeq 0.4$. For the very first time, fracture surfaces are observed to display a perfect Family−Vicsek scaling when the width of the system is changing. In other words, the so-called anomalous scaling that refers to the existence of *two* different roughness exponents – one for the scaling of the roughness with the system size and one for the local properties of the roughness of one sample – is found to be irrelevant for describing our system.

For the two materials, the approach is therefore the following: At first, we analyze the 1D self-affine properties of their fracture surfaces. In particular, possible multi-scaling is investigated through the analysis of the distribution of height fluctuations. Then, the effects of the microstructure and the system size on the self-affine domain are systematically studied. Finally, the 2D height correlations are investigated in order to reveal the anisotropy of fracture surfaces.

3.1 Materials and methods

Preparation of fracture surfaces of glass ceramics : First, fracture surfaces of an artificial material comparable to sandstone, glass ceramics made of sintered glass beads, are studied. The synthesis as well as the characterization of the samples of glass ceramics have been performed by P. Vié (LCPC, Marne la Vallée). The glass ceramics are prepared by heating a mold filled with glass beads. Two series of beads are used: Beads with diameters ranging from 104 to 128 μm and beads with diameters $50 - 65$ μm. The beads are made of a soda-lime glass mainly composed of SiO_2, Na_20 and Ca0 represented at 73 %, 14 % and 8 % respectively. The mold is then heated at 700 ^oC during a defined duration ranging from 20 to 200 minutes. This duration sets the porosity ϕ that can be tuned from 3 % to 26 %. In the following, the

characteristic microscopic length scale d is taken equal to the mean bead diameter. The open porosity is measured by saturating the sample with water and the profile of the total porosity (open + closed) along the sample is measured by gamma-ray absorption.[1] Porosity variations along the samples are measured to be of the order of 1 % so that ϕ may be considered as constant and equal to the mean value within ± 1 %. This process produce cylinders of glass ceramics of radius and height equal to 40 mm and 130 mm, respectively. The samples used in the fracture tests are cut out from this cylinder.

Two kinds of mode I fracture tests were performed. Some of these tests were performed in the laboratory of structural engineering at the federal university of Rio de Janeiro in collaboration with E. Fairbairn and R. Toledo and the others in Laboratoire de Rhélogie du Bois at Bordeaux in collaboration with S. Morel and G. Mourot. Fast fracture propagations are generated through modified Brazilian fracture tests: A uniaxial compressive load is applied to an annular specimen of inner and outer radii equal to 15 mm and 40 mm, respectively, and width equal to 20 mm. Two symmetrical cracks are then initiated. They propagate from the inside toward the outside where the compressive forces are applied. A picture of the samples used in the experiments is shown in Fig. 3.1.



Figure 3.1: Two samples that have been used to generate fracture surfaces of glass ceramics: Modified Brazilian test geometry that leads to rapid mode I fracture (left) and modified Tapered Double Cantilever Beam geometry that leads to stable mode I fracture (right). The outside diameter of the annular sample is 80 mm.

Quasistatic fracture propagations are generated within modified Tapered Double Cantilever Beam (TDCB) samples. A typical sample is shown in Fig. 3.1. The fracture is initiated from a straight notch (thickness 1 mm) by applying on both sides a uniaxial tension with a constant opening rate: The tapered shape of these specimens results in a stable mode I crack growth (see Ref. [69]). 2D finite element calculations

[1]The open porosity of a material is made of the pores that are connected to a free surface by connections with the other pores so that the open porosity can be measured by saturating the material of water. The close porosity is made of the pores that are not connected to a free surface. The total porosity is defined as the sum of the open and close porosity.

were performed to determine both the stress intensity factor and the compliance variations for various specimen dimensions. Therefore, it was possible to choose the dimensions of the samples to get a nearly constant crack growth velocity on the first 20 mm: In particular, their height and length are respectively 20 mm (perpendicular to the crack propagation) and 60 mm (parallel to it). Their width along the crack front direction is 20 mm. The crack propagation velocity v_{crack} is determined from the variations of the electrical resistance of a thin gold layer deposited on the side of the sample. As expected, v_{crack} has been observed to remain fairly constant during the propagation. Crack growth velocity ranging from 50 μm s^{-1} to 40 mm s^{-1} were obtained by varying the opening rate of the testing machine. A force sensor measures the applied loading. The experimental setup used for the quasistatic fracture tests is shown in Fig. 3.2. The mechanical parameters that have been measured during the fracture tests are analyzed in Annexe A.

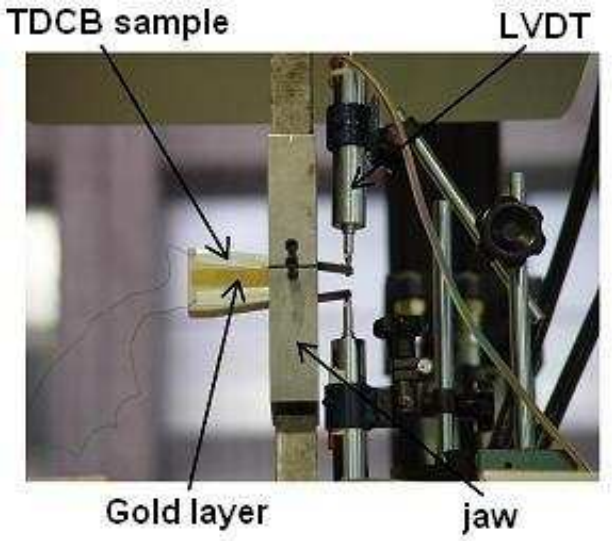


Figure 3.2: Experimental setup used to perform the quasistatic fracture tests.

Typical 1D profiles of fracture for three samples with three different porosities are displayed in Fig. 3.3. The roughness amplitude increases by almost two orders of magnitude from $\simeq$ 1 μm when $\phi = 3$ % up to $\simeq$ 100 μm when $\phi = 26$ %: Different profilometers are therefore needed to scan all the samples. For surfaces with very low rms roughness – and at the same time porosity – we use an interferometric optical profilometer[2] ($^{\text{TM}}$Talysurf CCI 6000) with a vertical resolution better than 0.1 nm and a lateral resolution $\simeq$ 1 μm. Unfortunately, such an interferometric optical profilometer remains confined to very smooth surfaces, with local slope smaller than 5 %. In practice, the fracture surfaces are too rough for such an interferometric technique

[2]These scans were realized at Taylor Hobson with C. Buisson.

when the porosity is larger than 7 %. We then use a mechanical stylus profilometer (^{TM}Talysurf Intra) with respective vertical and lateral resolutions $\simeq$ 10 nm and $\simeq$ 2 μm. For lower porosities ($\phi < 7$ %), both profilometers are usable (although the mechanical one has a poorer resolution) which allowed to check the consistency of the two measurements. For both profilometers the maps contain 1024×1024 points and the fields of view are respectively 3×3 and 6×6 mm. In the second technique, the stylus remains in contact with the surface and, for porosities higher than 18 %, it often gets jammed into the deepest asperities of the surface. One then uses a point by point mechanical profilometer. A sensor tip is lowered until it touches the surface in order to measure its height; the tip is then raised by 200 μm before getting moved laterally by 25 μm to the next measurement point. The vertical and the lateral resolutions are respectively $\simeq 3$ μm and $\simeq 10$ μm. The typical field of view is 8×8 mm. The consistency of the measurements was verified by comparing profiles provided by the two mechanical systems for $\phi = 18$ %. The scanning technique used for each porosity is listed in Tab. 3.2. These measurements provide 3D maps of the surface and thus surface elevation profiles of the type shown in Fig. 3.3.

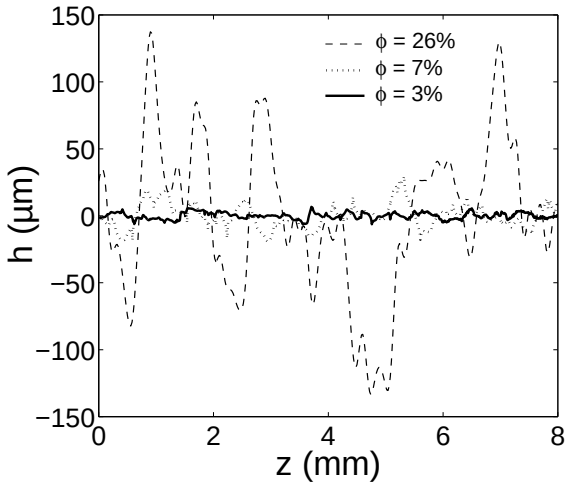


Figure 3.3: Height profiles extracted from fracture surfaces of three sintered glasses with three different porosities but with beads with the same diameter $104 - 128$ μm.

Preparation of fracture surfaces in sandstones : Fracture surfaces of a natural sandstone are also analyzed. Mode I fracture tests have been performed on samples cut out from the same block of Fontainebleau sandstone. The latter is characterized by the distribution of grain diameter plotted in Fig. 3.4 a. It was possible to measure its granulometry after that a small piece of the block has been crushed. The mean grain size is $d \simeq 240$ μm. The porosity of the sandstone is measured from SEM images performed on thin strips of sandstone. A typical example of these images

is represented in Fig. 3.4 b. We measure $\phi = 10\ \% \pm 1\ \%$. Its grain composition measured through X-ray is quartz at 99 %.

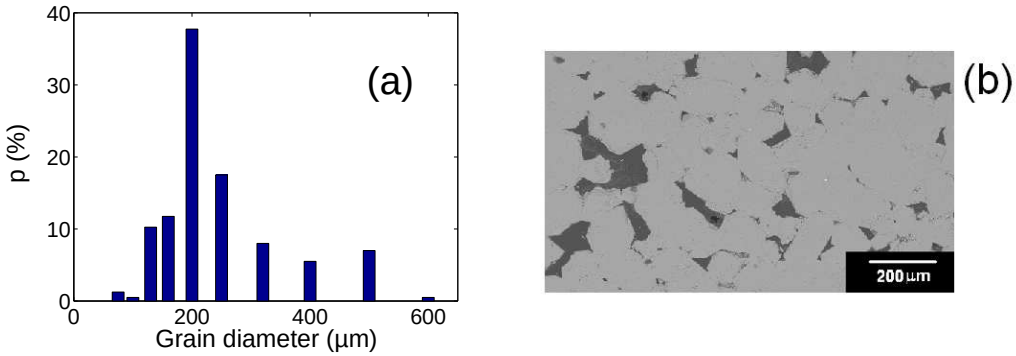


Figure 3.4: (a) : Diameter distribution of grains composing the sandstone. The mean grain size is $d \simeq 240\ \mu$m; (b) : Typical example of SEM images of thin strip of sandstone. The analysis of various images corresponding to different zones of the sandstone block leads to a mean porosity $\phi = 10\ \%$.

Fracture surfaces are induced by fast growing cracks, using a modified Brazilian fracture test (inner and outer radii equal to 13 mm and 50 mm respectively) in the same spirit as the tests performed on glass ceramics (see preceeding paragraph). Samples of width ranging from 7.8 mm to 52 mm are studied. One uses then the point by point mechanical profilometer previously used to scan the fracture surfaces of glass ceramics for porosities $\phi > 15\ \%$.

Sample	L	d_z (μm)	d_x (μm)	n_z	n_x
♯ 1	8 mm	25	250	272	133
♯ 1	8 mm	50	500	95	45
♯ 2	14 mm	50	250	263	136
♯ 2	14 mm	25		526	1
♯ 3	26 mm	100	100	248	252
♯ 3	26 mm	25	25	972	8
♯ 4	52 mm	50	1000	1007	30
♯ 4	52 mm	25		1991	1

Table 3.1: Elevation maps recorded on fracture surfaces of sandstone with various sample width L. For each scan of the surfaces, the pixel size $d_z \times d_x$ as well as the size $n_z \times n_x$ of the scan (in number of pixels) are given.

For each sample, the fracture surface is scanned twice: First, a height map of the whole fracture surface ($L \times 37$ mm) is recorded. The pixel size $d_z \times d_x$ – the distance

between two successive points of the scan along the z and x-axis respectively – as well as the size $n_z \times n_x$ of the scan (in number of points) are listed in Tab. 3.1. Moreover, a small part – generally one profile – of the surface is also scanned with a smaller pixel size (see Tab. 3.1). Therefore, it is possible to test the robustness of our analysis by studying height maps with different sizes. To avoid any influence of the transient roughening regime, only the part of the surface far enough from the initiation (some millimeters) is then analyzed. The full procedure is described in Section 3.3. A typical snapshot of a fractured sandstone surface corresponding to a specimen width of $L = 26$ mm is shown in Fig. 3.5. The in-plane (along x and z) and out-of-plane (along h) length scales of the largest features observed on this surface are of the order of 5 mm and 300 μm respectively.

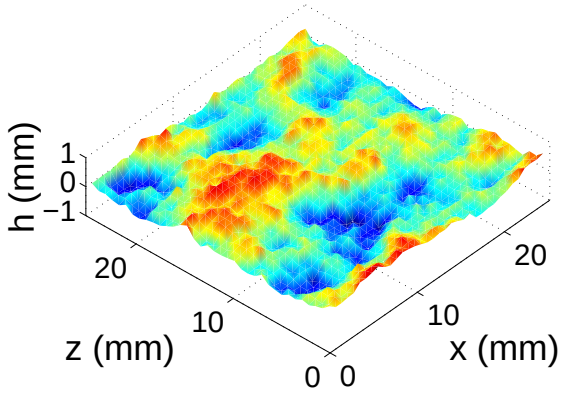


Figure 3.5: Topographic image of a fractured sandstone surface. The x-axis and z-axis correspond to the crack propagation direction and to the crack front direction, respectively.

3.2 Fracture surfaces of glass ceramics

In a recent study [2], fracture surfaces of sandstone were observed to display a roughness exponent $\zeta \simeq 0.45$ remarkably lower than the "universal" exponent $\zeta \simeq 0.75$ (see Chapter 2). In this section, we study the fracture surfaces of an artificial sandstone, glass ceramics. This study is motivated by two main reasons: (i) We will test the scenario proposed in Ref. [2] for which the low roughness exponent observed for sandstone samples is a signature of their intergranular mode of rupture. This point will be discussed in Section 3.3 where a transition from trans to intergranular failure mode when ϕ is increasing will be observed, without, however, any effect on the value of the roughness exponent. (ii) We study materials with slightly different microstructures compared to sandstone. In other words, we test the robustness of the observations reported by Boffa *et al.* in an artificial material, glass ceramics,

which is also made of cemented grains, but with a microstructure that can be tuned experimentally. In particular, both the porosity and the grain size can be chosen independently, so that their influence on the morphology of fracture surfaces can be characterized.

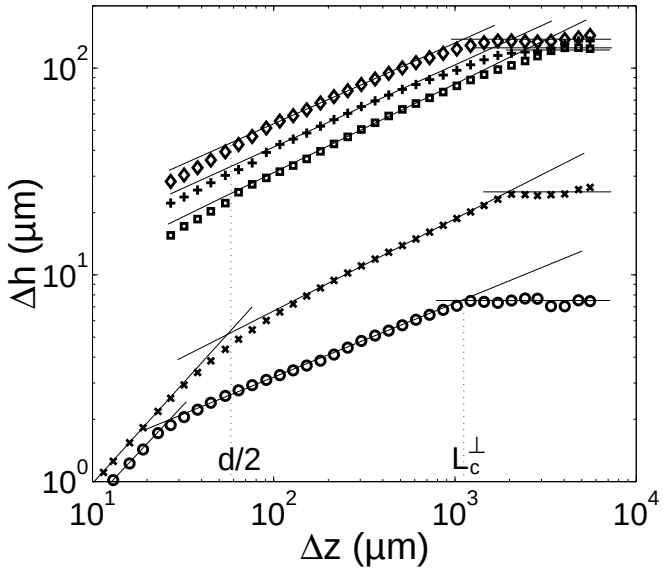


Figure 3.6: Log-log representation of Δh (averaged over profiles at different x values) as a function of Δz for surface roughness profiles of several sintered glass samples. - Samples fractured using the TDCB test with porosities $\phi = 7$ % ($\times$), 15 % ($\square$) and 26 % ($+$) - Samples fractured using the Brazilian test with porosities $\phi = 3$ % ($\circ$) and 25 % ($\Diamond$) - Range of bead diameters used to realize samples : $104 - 128$ μm - Straight lines: linear fits with slope ζ (Table 3.2).

One-dimensional scaling properties : Figure 3.6 displays the variations of the 1D correlation function $\Delta h(\Delta z)$ as a function of Δz in a log-log scale for several samples with different porosities ranging from 3 % to 26 %. They have been fractured either quasistatically (v_{crack} ranging from 50 $\mu\text{m}\,\text{s}^{-1}$ to 40 mm^{-1}) mode or after a fast crack propagation (v_{crack} of the order of $\simeq 1$ $\text{m}\,\text{s}^{-1}$). The curves correspond to an average of $\Delta h(\Delta z)$ over profiles corresponding to different distances x to the initiation and lying within the region where the statistics of the roughness is stationary.

Let us examine, for instance, the lowest curve corresponding to a 3 % porosity sample fractured using the modified Brazilian test procedure. The variation can clearly not be fitted by a single power-law over the full range of Δz values investigated: three domains of variation are visible and correspond to exponents respectively equal to 1, 0.36 and 0 (straight lines). The last value indicates that the surface appears

as a plane at large length scales and the first one reflects the Euclidean geometry of individual grains. The surface profile is therefore self-affine (here with an exponent $\zeta = 0.36$) only in the intermediate domain between two limiting length scales : In the log-log plot of Fig. 3.6, these boundaries correspond to the intersections between the straight lines fitted in the different domains. The lower boundary is of the order of the bead radius $d/2$ and the upper one is referred to as $L_c^{\perp}$.

This result is generalized by comparing the different curves in Fig. 3.6 corresponding to samples of various porosities and fractured both in the quasistatic and fast propagation modes. All the curves have the same general shape and, in log-log coordinates, their slopes are nearly the same in the intermediate domain: This shows that the roughness exponent is very similar in all cases while the vertical shift between the curves reflects different roughness amplitudes.

	$\phi = 3$ %	$\phi = 7$ %	$\phi = 15$ %	$\phi = 18$ %	$\phi = 25$ %	$\phi = 26$ %	Average value
	B.D.1	B.D.1	B.D.1	B.D.2	B.D.1	B.D.1	
	Dyn.	Q.S.	Q.S.	Dyn.	Dyn.	Q.S.	
Tech.	$1-2$	2	3	$2-3$	3	3	
ζ	0.36	0.43	0.43	0.40	0.39	0.39	0.40 ± 0.03
ζ_{FT}	0.38	0.44	0.38	0.37	0.39	0.39	0.39 ± 0.02
β	0.43	0.48	0.51	0.43	0.42	0.45	0.46 ± 0.03
ζ_{2D}	0.42	0.41	0.37	0.36	0.36	0.42	0.40 ± 0.03
β_{2D}	0.44	0.52	0.53	0.42	0.46	0.51	0.49 ± 0.04
z	0.91	0.79	0.73	0.84	0.76	0.83	0.81 ± 0.06
$\Delta h(d)$	3.3	7.9	32	15	54	44	
$L_c^{\perp}$	1.1	1.9	2.4	0.8	1.1	1.6	

Table 3.2: Physical and statistical characteristics of the glass ceramics - (ϕ) sample porosity; glass beads diameter range (B.D.1) $104-128$ μm, (B.D.2) $50-65$ μm; crack propagation mode (*Rap.*) rapid, (*Q.S.*) quasi-static; (Tech..) surface measurement technique (1) interferometric, (2) stylus profilometer (3) point by point. - Statistical characteristic parameters of 1D profiles normal to crack propagation (ζ , ζ_{FT}) self-affine exponent values obtained respectively from the variation of Δh with Δz and from the Fourier power spectrum; ($\Delta h(d)$) roughness amplitude in μm; ($L_c^{\perp}$) upper boundary of self-affine domain along the z-axis in mm.

The numerical values of the parameters characterizing all these curves are listed in Table 3.2 for all samples investigated in the present work. Table 3.2 confirms that ζ has a very similar value $\zeta = 0.40 \pm 0.04$ for all samples independent of the bead size, of the porosity and of the crack propagation velocity: this common value is much lower that the value 0.75 reported for many materials and closer to the value 0.45 obtained for sandstone in paragraph 3.4. This result is robust with respect to the method used

to determine ζ as shown by the comparison with the values $\zeta_{\rm FT}$ in Table 3.2 obtained from the analysis of power spectra [57]. The upper boundary $L_c^{\perp}$ of the self-affine domain is of the order of 1 mm for toroidal samples, *i.e.* a twentieth of the sample width. The variation of the upper limit of the self-affine domain as a function of the sample width is systematically studied in Section 3.4 for sandstone. The ratio of the cut-off length over the width is found to be slightly larger for the TDCB geometry, of the order of a tenth. Finally, let us note that the roughness amplitude $\Delta h(d)$ depends strongly on the porosity. This will be quantitatively analyzed in Section 3.3.

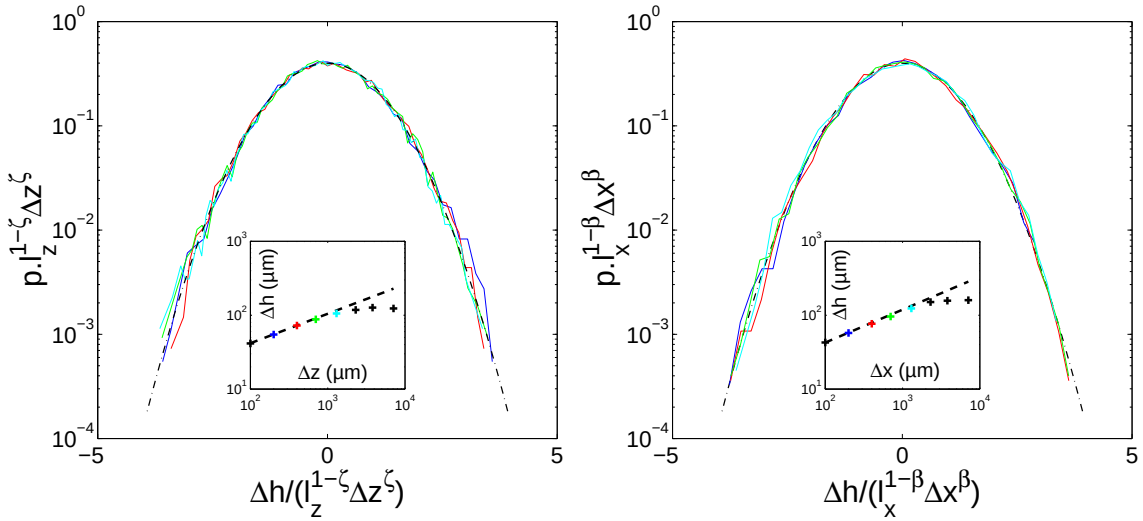


Figure 3.7: Normalized distribution of height variations on a fracture surface of glassy ceramics with a porosity $\phi = 26$ % in a semi-logarithmic representation for profiles parallel (a) to the crack front and (b) to the crack propagation for Δz (respectively Δx) equal to 200 μm (blue), 400 μm (red) 700 μm (green) and 1.1 mm (cyan). The master curves obtained with $\zeta = 0.39$ and $\ell_z = 23$ μm (resp. $\beta = 0.45$ and $\ell_x = 21$ μm) along the z-axis (resp. the x-axis) are found to be Gaussian distributions $p(x) = 1/\sqrt{2\pi}e^{-x^2/2}$ (dashed line). The variation of the 1D correlation functions, *i.e.* the standard deviation of the distribution, is shown in the inset. The dashed lines are power-law fits from which the values of ζ, β, ℓ_z and ℓ_x are determined

Statistics of height variations : In order to analyze further the geometry of the profiles, we shall now focus on the distribution of height variation $P(\Delta h)$. This distribution is computed at various scales Δz and Δx parallel to the crack front (z-axis) and to the crack growth (x-axis) respectively. After normalization, the distributions $\Delta z^{\zeta} P(\Delta h/\Delta z^{\zeta})$ and $\Delta x^{\beta} P(\Delta h/\Delta x^{\beta})$) collapse on the same curve shown in Fig. 3.7 a and b. In other words, the profiles studied do not exhibit multiscaling and one scaling exponent ($\zeta = 0.39$ or $\beta = 0.45$ in the present case depending on the direction

investigated) is enough to describe the statistics of the variations of height. These exponents can be calculated by normalizing these distributions to get a collapse but also from the power-law variation of any of their moment. For example, the variation of the square root of the second order moment referred to as the 1D correlation function $\Delta h(\Delta z)$ and $\Delta h(\Delta x)$ is shown in the insets of Fig. 3.7 a and b along the z-axis and x-axis respectively. The fit of these variations to a power-law leads also to the values $\zeta = 0.39$ and $\beta = 0.45$. The scaling exponents measured through this second technique are listed in Table 3.2 for various samples: the exponent $\beta = 0.46 \pm 0.03$ is found systematically larger than the other one $\zeta = 0.40 \pm 0.03$ irrespective of the sample porosity, its bead diameter as well as the crack growth velocity. However, and in spite of different scaling properties, profiles parallel to the z and x-axis display both Gaussian distributed height variations.

Two-dimensional structure : To capture the physical origin of this anisotropic scaling, one suggests to study in detail the two-dimensional structure of the glass ceramics fracture surfaces. The appropriate statistical tool is the 2D height−height correlation function $\Delta h(\Delta z, \Delta x)$ defined in Formula 2.4 as the typical difference of height[3] between two points separated by the distance Δz and Δx along the crack front and the crack growth direction respectively. Figure 3.8 displays the variations of the normalized function $\Delta h_{\Delta x}/\Delta x^{\beta}_{\rm 2D}$ as a function of the normalized variable $\Delta z/\Delta x^{1/z}$ for different values of Δx. All curves collapse onto a single master curve with a plateau behavior at small distances and then a power-law variation. In other words, the scaling of the correlation function can be described by Eq. (2.5) referred to as a Family−Vicsek scaling [66]:

$$\begin{aligned} &\Delta h(\Delta z, \Delta x) \sim \Delta x^{\beta_{\rm 2D}} f(\Delta z/\Delta x^{1/z}) \\ &\text{where} \quad f(u) = \begin{cases} 1 & \text{if u}\ll 1 \\ u^{\zeta_{\rm 2D}} & \text{if u}\gg 1 \end{cases} \end{aligned} \tag{3.1}$$

The set of scaling exponents used to obtain the collapse of the curves is $\beta_{\rm 2D} \simeq 0.5$ and $z \simeq 0.8$ and the exponent of the power-law behavior of the collapsing curve is $\zeta_{\rm 2D} \simeq 0.4$. Their numerical value obtained for each sample investigated is listed in Table 3.2: This indicates that the two-dimensional scaling properties depend very weakly on the microstructural properties of the glassy ceramics.

These results are in agreement with the values of the scaling exponents ζ and β obtained from the scaling of the 1D correlation function. Letting Δz tend to zero in

[3]The typical difference of height is defined here as the square root of the second order moment of the distribution $P(\Delta h)$ of the variations of height between two points of the surface separated by the distance Δz along the z-axis and Δx along the x-axis. With this definition, $\Delta h(\Delta z, \Delta x = 0)$ and $\Delta h(\Delta z = 0, \Delta x)$ coincide with the 1D correlation function computed along the z-axis and the x-axis respectively.

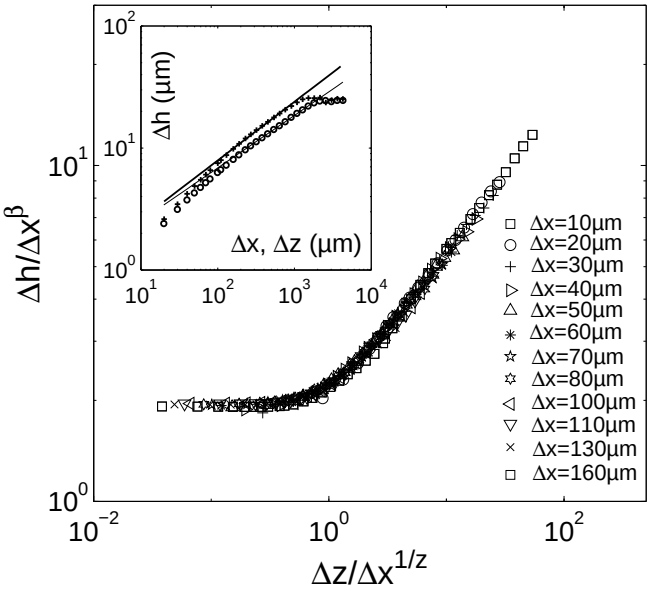


Figure 3.8: The inset displays the 1D correlation functions computed along the crack front direction ($\circ$) and the crack propagation direction ($+$). The main panel shows the 2D height−height correlation functions $\Delta h_{\Delta x}(\Delta z)$ corresponding to different values of Δx vs Δz for a fracture surface of glassy ceramic with porosity $\phi = 6\%$. The data collapse was obtained using Eq. (2.5) with exponents $\zeta \simeq 0.4$, $\beta \simeq 0.5$, and $z = \zeta/\beta \simeq 0.8$.

Eq. (3.1) leads to $\Delta h \sim \Delta x^{\beta_{2D}}$ so that $\beta_{2D} = \beta$ is expected. Letting Δx tend to zero in formula 3.1, one obtains $\Delta h \sim \Delta x^{\beta_{2D}-\zeta_{2D}/z}\Delta z^{\zeta_{2D}}$ so that, in addition $\beta_{2D} = \beta$ and $z = \zeta_{2D}/\beta_{2D}$. The last column of table 3.2 giving the mean value of the various scaling exponents confirms that these relations are respected.

To conclude this first section, let us insist on the high robustness of the roughness properties investigated here: The distribution of the variations of height, the 2D structure of the surface and the value of its three scaling exponents are observed to depend nor on the characteristic length scale of the microstructure neither on the porosity. The comparison of these scaling properties with a natural material with a similar microstructure, a sandstone, is performed in Section 3.4. But at first, let us focus on characteristics of fracture surfaces that depend on the microstructure.

Up to now, the discussion has been focused on the scaling laws verified by the roughness at different length scales. We shall now be concerned with the overall amplitude of the roughness and with its dependence on the characteristic parameters of the material.

3.3 Roughness amplitude

The previous section has been devoted to the study of the self-affine properties of fracture surfaces. For instance, the 1D correlation function Δh computed on profiles perpendicular to the crack growth direction was found to be proportional to Δz^{ζ}. One can replace this proportionality relation by the following equality:

$$\frac{\Delta h}{\Delta h(d)} = \left(\frac{\Delta z}{d}\right)^{\zeta}, \tag{3.2}$$

where d can be taken equal to the characteristic length scale of the microstructure of the material (we will take the mean grain size). As a consequence, the amplitude of the roughness may be characterized by the value of $\Delta h(d)$ (amplitudes corresponding to other Δz values can then be obtained from Eq. (3.2)). In the following, we will use the normalized amplitude $\Delta h(d)/d$ because its value can be interpreted in terms of fracture mode (trans- and inter-granular rupture) as will be discussed at the end of this section. The amplitude defined in such a way is directly linked to the topothesy ℓ_z, *i.e.* the scale at which Δh is equal to Δz, by the relation $\Delta h(d)/d = (\ell_z/d)^{1-\zeta}$.

If an important effort has been devoted in the past to the scaling properties of fracture surfaces, very few studies have dealt with the amplitude of the roughness in spite of its obvious practical interest and its possible relevance to understand the underlying mechanisms of failure of materials. The series of sintered materials we are using allows, for the very first time, to study specifically the influence of microstructural parameters (the porosity ϕ and the typical microstructural length scale d) on the roughness amplitude. But in order to estimate quantitatively the effect of the microstructure on this quantity, we will study at first the influence of the fracture test geometry as well as of the distance to the crack initiation.

Effect of the crack initiation : Various authors [70, 29] have reported that roughness properties were not stationary in a small zone of the fracture surface near the initiation of the crack. This transient regime is studied in Fig. 3.9 for a fracture surface of glassy ceramics with $\phi = 3$ % broken in the modified Brazilian geometry. In this figure, data points correspond to single profiles parallel to z at a given distance x from the side of the sample where the crack was initiated. The local roughness is characterized by its normalized amplitude $\Delta h(d, x)/d$. A transient regime in which $\Delta h(d, x)/d$ decreases with the distance x is indeed observed: The width of this zone is $x_c \simeq 1$ mm. At larger distances, $\Delta h(d, x)/d$ merely fluctuates around an average value (dashed line). This mean value will correspond to the roughness amplitude and the corresponding error will be taken equal to three times the standard deviation of the fluctuations observed, *i.e.* representing an interval of confidence of 95%. For the other glass ceramics and sandstone samples investigated, the width x_c of the transient regime zone has the same order of magnitude.These results allow to restrict (as in the

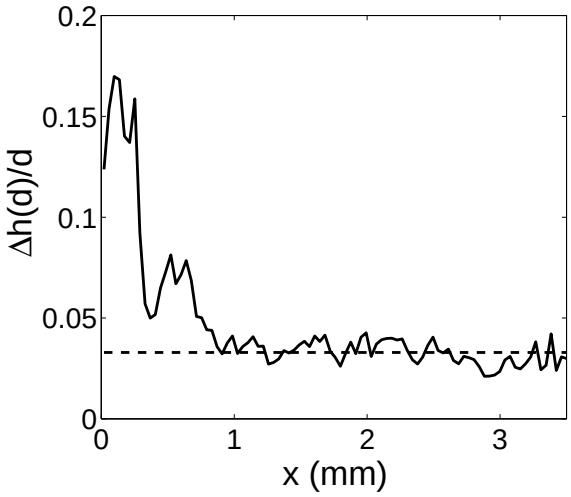


Figure 3.9: Variations of the roughness characteristic exponent ζ and amplitude $\Delta h(d)$ with the distance x to the initiation notch for the same sample ($\phi = 3$ %) as in Fig. 3.6.

previous sections) the statistical analysis to distances larger than 1 mm where the roughness is statistically stationary : This justifies our use in Fig. 3.14 and Fig. 3.6 of curves obtained from an average over several profiles corresponding to different x values.

Effect of the sample width : After a brief study of the transient regime near the crack initiation, let us study the effect of the sample width on the roughness amplitude. The effect of the specimen geometry on its roughness has only been studied for fractured sandstone surfaces. The detailed analysis of these surfaces is shown in the next section.

Studying the transient roughening development during fracture test starting from a straight notch, Lopez and Schmittbuhl [71] have observed on granite fracture surfaces that this amplitude *depends* on the distance to the initiation. This evolution has been described through a scaling law referred to as *anomalous* involving the existence of a second exponent ζ_g referred to as *global* roughness exponent different from the *local* roughness exponents ζ measured until now. This anomalous scaling of the transient roughening has then been observed on other quasi-brittle materials such as mortar [30] and wood [29]. The local exponent was measured to be $\zeta \simeq 0.75$ for these three materials whereas the value of the global exponent was shown to change from material to material. As reported in [72], the anomalous scaling can also be measured in the stationary part of the fracture surface, *i.e.* far enough from the initiation so that the roughness amplitude can be considered as independent of the distance to the initiation. Indeed, the value of the amplitude *depends* on the width L of the broken

sample and scales as:

$$\Delta h(\Delta z = cst) \sim L^{\zeta_g - \zeta} \tag{3.3}$$

Here, we have investigated such a scaling for fractured sandstone surfaces. Fig. 3.10 presents the variations of the roughness amplitude with the width L of the sample. In order to test the robustness of the measurement, the amplitude $\Delta h(\Delta z)$ is measured at two different length scales $\Delta z = 100$ μm and $\Delta z = 1$ mm. The mean value of the amplitude is found to fluctuate by less than 5% from sample to sample at the two scales studied: The roughness amplitude remains therefore independent of the sample width in the range investigated. This result can also be qualitatively observed in Fig. 3.14 a where the correlation functions $\Delta h(\Delta z)$ corresponding to various sample widths are plotted on the same graph: the curves superimpose each other in the domain of length scales where they are all evolving as a power-law. As a consequence, sandstone fracture surfaces do not exhibit anomalous scaling as defined by Eq. (3.3).

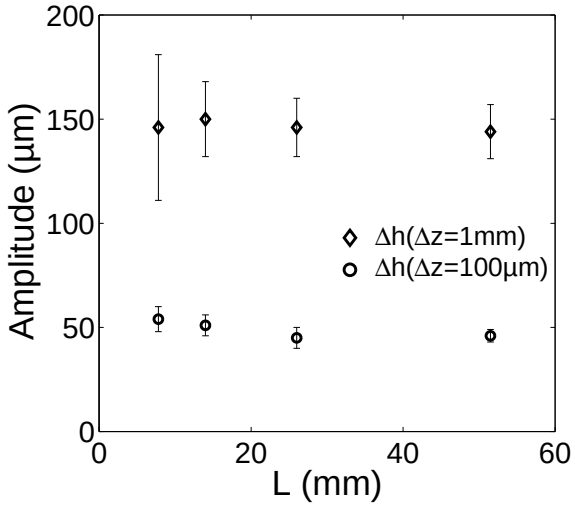


Figure 3.10: Absence of variation of the roughness amplitude of fracture surfaces of sandstone with the width L of the sample – the roughness amplitude is measured as the value of the 1D correlation function $\Delta h(\Delta z)$ for two values of Δz.

This result suggests strongly that the roughness amplitude does not depend on the geometry of the fracture test (even if we only studied the influence of the sample width) if it is measured in the stationary part of the fracture surface. This suggests that the only parameter that may change its value is the crack growth velocity and the microstructure of the material.

Effect of the crack growth velocity : The effect of the crack growth velocity on the amplitude of crack roughness has been studied by Backers *et al.* [73] for sandstone

samples. Analyzing fracture surfaces resulting from crack growth velocities ranging from 1 μm s^{-1} to 10 mm s^{-1}, they only observed fluctuations – on the order of 15 % – of the roughness amplitude around the mean value. This suggests that for a very similar material such as glass ceramics, the crack roughness may be also independent of the crack velocity. This is confirmed by our experimental results: the amplitude roughness corresponding to glass ceramics samples with $\phi \simeq 25 - 26$ % differs from 20 % (see Table 3.2) when the crack growth velocity is changed by almost 3 decades. In the following section, we will see that the roughness amplitude of all the samples follow the same function of the porosity and the bead diameter, irrespective of the broad range of velocities investigated in this study. This is an additional argument in favor of the weak influence of the crack velocity on the roughness amplitude.[4]

Effect of the microstructure : As stressed in the previous sections, the roughness amplitude depends strongly on the microstructure and very weakly on the other parameters such as crack growth velocity and sample width. In this section, we identify the microstructural parameters that set the amplitude and give the quantitative relation between glassy ceramics microstructure and amplitude of their crack roughness.

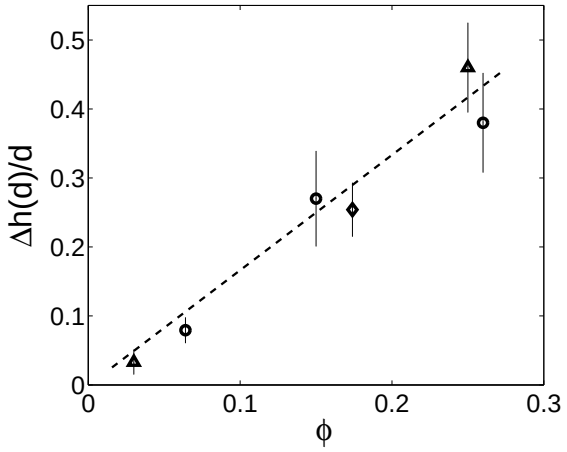


Figure 3.11: Variation of $\Delta h(d)/d$ as a function of porosity ϕ for the glass ceramics samples: Range of bead diameters used to realize samples - $104 - 128$ μm ($\triangle$) : dynamic fracture ($\circ$) : quasistatic fracture - $50 - 65$ μm ($\Diamond$) rapid fracture. The slope of the dashed line is 1.7.

In Fig. 3.11, the normalized amplitude $\Delta h(d)/d$ obtained for all the glass ceramics and sandstone samples studied is plotted as a function of their porosity. The fracture surfaces have been obtained either after a quasistatic rupture ($\circ$) or a dynamic

[4]From a theoretical point of view, we will see in Section 4.2 that an effect of the crack growth velocity is only expected for v_{crack} of the same order than the sound velocity.

one ($\triangle$). Except one glass ceramics sample which is composed of glass beads with $d \simeq 58$ μm ($\diamond$), the samples are made of grains with $d \simeq 116$ μm.

Let us consider at first the sample of glass ceramics made of small beads ($d \simeq 58$ μm and $\phi = 18$ %). Although d is two times smaller than in the other samples, its normalized roughness amplitude $\Delta h(d)/d$ is close to the one of a glass ceramics with a similar porosity ($\phi = 15$ %) but with larger beads ($d \simeq 116$ μm). This result suggests that the roughness amplitude $\Delta h(d)$ is roughly proportional to the typical size of the microstructure.[5]

On the other hand, the normalized amplitude seems to evolve linearly with the porosity ϕ. A linear fit of the experimental data leads to

$$\Delta h(d)/d \simeq 1.7\,\phi \tag{3.4}$$

This result is quite remarkable in view of the large range of crack velocities investigated as well as the two fracture test geometries used in this study. In other words, within our domain of study of the various experimental parameters, the amplitude is found to be given by the very simple proportional law given in Eq. 3.4.

The increase of $\Delta h(d)/d$ with ϕ may be related to phenomena at the scale of a bead diameter. For high porosity samples, the crack propagates by breaking cemented necks binding two beads : the difference in height between neighboring beads is then of the order of their radius and $\Delta h(d)/d \simeq 0.5$. For low porosity samples, neighboring beads are more strongly welded to each other and the crack propagates through the beads : The deflections of the surface are weaker compared to the bead radius and $\Delta h(d)/d$ is lower. This is consistent with the increase of $\Delta h(d)/d$ from 0 to 0.5 shown in Fig. 3.11 when ϕ is increasing from 0 to 30 %. These differences in the propagation of the cracks are confirmed by scanning electron microscope (SEM) images of fractured samples: These display a transition from transgranular to intergranular propagation as the porosity increases. It is remarkable that this transition has no influence on the characteristic exponent ζ.

Concluding remarks : This study on the roughness amplitude of glass ceramics has allowed to identify the relevant parameter that sets its value: the microstructure of the material. In particular, we have shown that the amplitude defined as the value $\Delta h(d)$ of the correlation function at a distance of the order of the grain diameter d is proportional both to the grain diameter d and the porosity ϕ. An important implication of this observation is the inter- to trans-granular propagation of cracks as the porosity increases. At the opposite, the scaling properties of crack surfaces – and in particular the roughness exponent $\zeta = 0.4$ – was shown to be independent of the porosity (see Section 3.2). These results question the scenario proposed in Ref. [2] that suggested that a transgranular rupture could explain the low roughness exponent measured on porous materials. The origin of this exponent will be the challenging

[5]Even though one single example of glass ceramics with d different from 116 μm has been studied.

question addressed in Chapter 4. But at first, let us study in detail the properties of sandstone surfaces.

3.4 Morphology of fractured sandstone surfaces

Why did we study the morphology of fracture surfaces of natural sandstone while glass ceramics present the advantage to have a microstructure that can be tuned in a control manner? At first, it is important to verify that the scaling properties of the two materials are similar. Moreover, because sandstone is an abundant natural material, it is possible to investigate relatively large samples. Therefore, in this section devoted to fracture sandstone surfaces, we will investigate the influence of the system size on the roughness of crack surfaces.

Statistics of height variations : We will start this study by the analysis of profiles parallel to the z-axis (*i.e.* to the crack front) and located far enough from the initiation region so that the roughness properties are statistically stationary. We will reproduce for fractured sandstone surfaces the same approach than for glass ceramics. The scaling properties of these profiles are characterized by their 1D height−height correlation function, $\Delta h(\Delta z) = \langle (h(z+\Delta z) - h(z))^2 \rangle_z^{1/2}$. This function ($\circ$) is plotted in the main panel of Fig. 3.12 in a log-log scale for the sample of width $L = 8$ mm. One can see a nice power-law behavior characterized by a roughness exponent $\zeta = 0.43$up to a cut-off length scale $L_c^\perp$, and a plateau above $L_c^\perp$ (straight and dotted lines respectively). In other words, the surface appears as a plane at length scales larger than $L_c^\perp = 1.7$ mm defined as the abscissa of the intersection between the power-law fit and the plateau. At length scales $\Delta z < L_c^\perp$, the profiles are self-affine with an exponent $\zeta = 0.43$. The variation ($+$) of the correlation function computed on the second height map scanned on the same fracture surface (see Tab. 3.1) is represented on the same graph. This scan contains 45×95 pixels and represents a field of 23×5 mm^2 while the first analysis was performed on a larger map (133×273 pixels representing a field of $\simeq 33 \times 7$ mm^2). As it appears on Fig. 3.12, changing the number of pixels do not change the general shape of the correlation function as well as the value of the cut-off length $L_c^\perp$. In other words, the finite number of data points is not responsible for the saturation of the correlation function observed at large scales.

The inset of Fig. 3.12 that represents the variation of the local slope of the logarithm of the correlation function – defined as $\frac{\partial \log(\Delta h)}{\partial \log(\Delta z)}$ – computed on the larger height map ($\circ$), confirms this self-affine property which is reflected by a domain of constant slope in this representation. However, if we look carefully at this curve, one can observe slight deviations to the self-affine behavior for $\Delta z < d \simeq 240$ μm. This precise point requires a deeper analysis of the profile morphology.

The whole distribution $P(\Delta h)$ of height variation for a given distance Δz is now analyzed. For perfectly self-affine profiles, one would expect that the distributions

corresponding to various Δz values collapse onto a single curve when they are normalized according to the formula 2.2. Fig. 3.13 displays these normalized distributions for various values of Δz in a log-lin scale. Within the range $d < \Delta z < L_c^{\perp}$ (solid lines), the curves collapse nicely onto a same Gaussian distribution (dashed line). For Δz values lower than the grain diameter d (dotted lines), the curves and, more precisely, their tail do not collapse. The surface profiles are therefore self-affine (here with an exponent $\zeta = 0.43$) only in the intermediate domain between the two limiting length scales d and $L_c^{\perp}$ although the 1D correlation function behaves as a power-law even for length scales smaller than d (see Fig. 3.12). Let us note that the effect of the grain size on the analysis of the roughness of fracture surfaces can lead to a misunderstanding of their properties. The "effective multi-scaling" observed here is an artifact related to the presence of a typical length scale in the microstructure of our system – the grains here. Finally, the investigation domain for the scaling behavior is relatively small (between $d = 240$ μm and $L_c^{\perp} = 1.7$ mm) for the sample studied here. In the next paragraph, we show that $L_c^{\perp}$ increases with the sample width. This leads to larger self-affine domains for larger samples that will confirm the results obtained here.

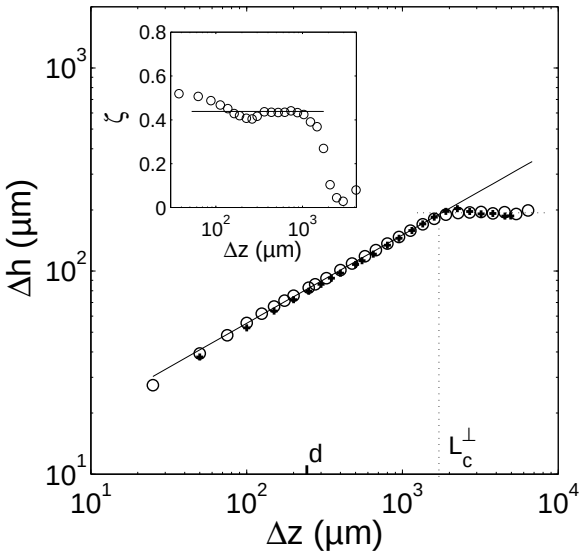


Figure 3.12: Height−height correlation function computed along the crack front direction (z-axis) on two different scans of the same fractured sandstone surface. (∘): 133×273 pixels representing $\simeq 33 \times 7$ mm^2; (+) : 45×95 pixels representing $\simeq 23 \times 5$ mm^2. The straight line is a power-law fit of the larger height map (∘) in the self-affine regime for $\Delta z > d = 240$ μm. Its slope is found to be $\zeta = 0.43$. The inset displays the variations of the local slope – defined as $\frac{\partial \log(\Delta h)}{\partial \log(\Delta z)}$ – of the logarithm of the correlation function computed on the larger height map (∘).

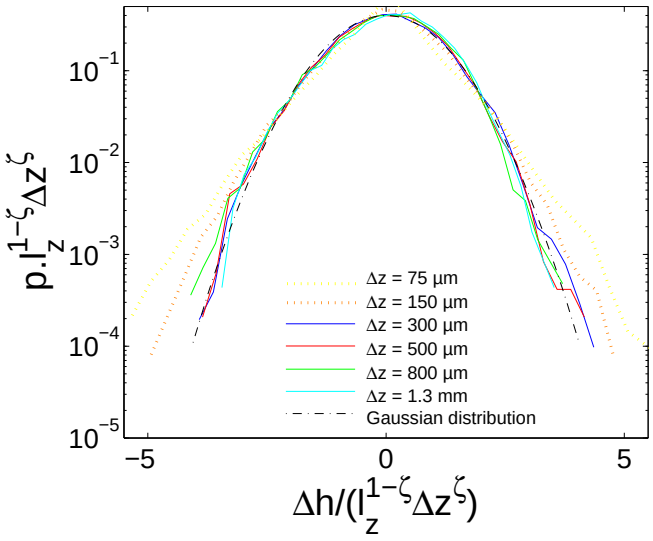


Figure 3.13: Normalized distribution of height fluctuations in a semi-logarithmic representation. For $\zeta = 0.43$ and $\ell_z = 35$ μm, all variation curves corresponding to $\Delta z > d = 240$ μm collapse onto a single Gaussian distribution $p(x) = 1/\sqrt{2\pi}e^{-x^2/2}$ displayed as a dashed line. It is worth noting that for $\Delta z < d = 240$ μm, data points do not collapse any more onto the master curve (dotted lines).

Effect of the sample size on the scaling properties : The dependence of this self-affine range with the size of the samples will now be studied on samples with four different widths: 1D height−height correlation functions computed for these four samples on profiles parallel to the crack front are displayed in Fig. 3.14 a. For each fracture surface, Δh varies first following a power-law of Δz and becomes constant. All curves are superimposed in the self-affine regime which is characterized by the roughness exponent $\zeta \simeq 0.47$ corresponding to the slope of the global power-law fit on data from all samples in the range $d < \Delta x < L_c^{\perp}(L)$. The roughness exponent measured on each sample is listed in Tab. 3.3. The variations from sample to sample lead to the following error bar for the global roughness exponent $\zeta = 0.47 \pm 0.04$ measured through the 1D correlation function. This value is in agreement with other experimental studies performed on sandstone fracture surfaces [2, 35]. The roughness exponent measured here is remarkably lower than those measured on various other materials and which were discussed in Chapter 2. In order to confirm this low value by an independent determination of the self-affine exponent, the Fourier power spectrum of the profiles has been computed and is shown in Fig. 3.14 b for the various samples. A power-law fit is made on all data points in the range $1/L_c^{\perp}(L) < f < 1/d$. The slope of the fit (dashed line) is found to be $-(1 + 2\zeta)$ with $\zeta = 0.46$ in agreement with the other method.

The Fourier power spectrum displays a power-law behavior up to a higher length

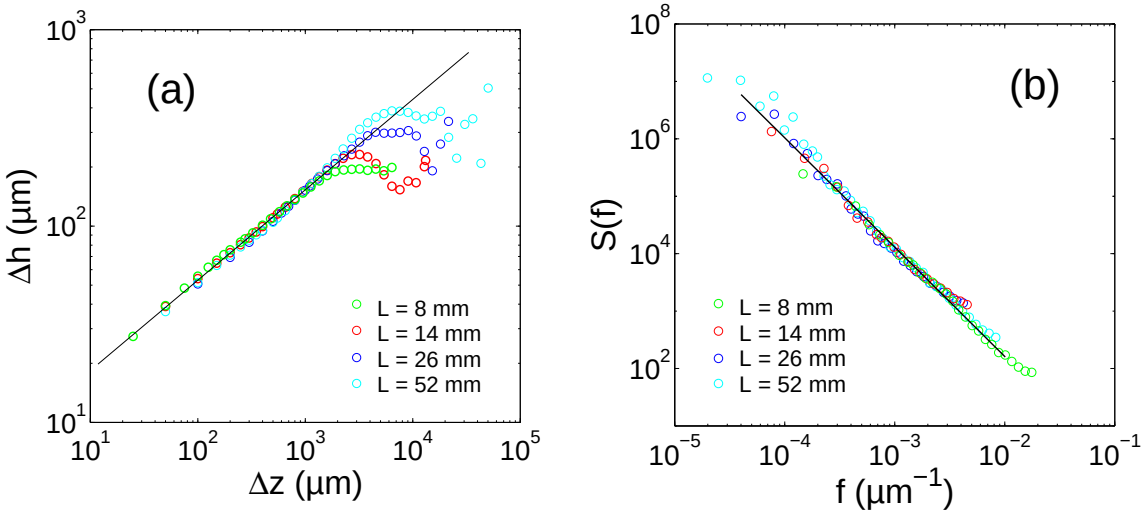


Figure 3.14: (a): Height−height correlation function for profiles parallel to the crack front direction (z-axis) on fractured sandstone samples of various widths. The straight line is a power-law fit to all curves in the self-affine regime for $\Delta z > d \simeq 240$ μm, with slope $\zeta_{1D} = 0.47$. (b) Fourier power spectrum of profiles parallel to the direction of the crack front. The slope of the power-law fit is found to be $-(1 + 2\zeta_{FT})$ with $\zeta_{FT} = 0.45$.

scale value than the upper bound of the self-affine domain determined by the analysis of the correlation function. The latter is more reliable to measure a cut-off length scale than the Fourier analysis (see Ref. [54]). Thus, we will use only Fig. 3.14 a that displays correlation function variations for studying the plateau regime observed at large scales. One can observe that these regimes clearly do not coincide for the various sample widths.

Table 3.3: Scaling exponents measured from the calculation of the 1D correlation function (ζ_{1D} and β_{1D}), the Fourier analysis (ζ_{FT} and β_{FT}) and the 2D correlation function (ζ_{2D}, β_{2D} and z) on fracture surfaces of sandstone for samples with various widths L.

Sample	L	ζ_{1D}	β_{1D}	ζ_{FT}	β_{FT}	ζ_{2D}	β_{2D}	z
♯ 1	8 mm	0.43	0.40	0.45	0.46	0.38	0.38	1.03
♯ 2	14 mm	0.46	0.51	0.43	0.50	0.43	0.50	0.90
♯ 3	26 mm	0.48	0.46	0.46	0.47	0.42	0.43	0.99
♯ 4	52 mm	0.51	0.53	0.50	0.48	0.50	0.56	0.90
Average		0.47	0.48	0.46	0.48	0.43	0.47	0.95
$\zeta = 0.45 \pm 0.06$			$\beta = 0.48 \pm 0.05$			$z = 0.95 \pm 0.1$		

The cut-off length $L_c^{\perp}$ is plotted in Fig. 3.15 as a function of the specimen width. This quantity $L_c^{\perp}$ can be interpreted as the in-plane size of the largest features observed on the fracture surfaces. This length is observed to increase linearly with the specimen width as $L_c^{\perp} = 0.15L$.

This observation suggests that there is no intrinsic upper bound to the scale invariance behavior of fractured sandstone surfaces – and more generally on surfaces with a low roughness exponent. This observation represents a major difference with fracture surfaces characterized by $\zeta \simeq 0.75$. Indeed, we will show in Chapter 4 that the upper bound of the self-affine domain is an intrinsic quantity of the material (and do not depend on the sample width when the latter is large enough). The implications of this result on the origin of the self-affine geometry of fracture surfaces are largely debated in the next chapter.

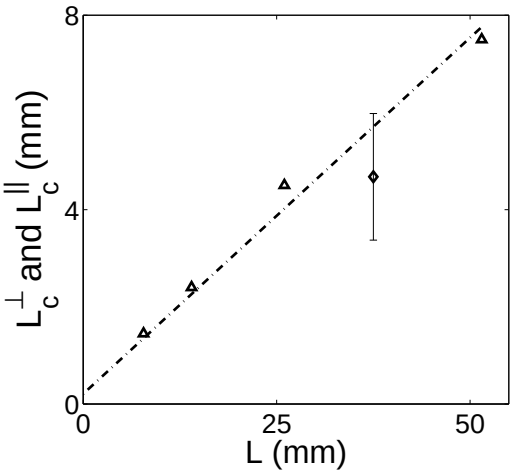


Figure 3.15: The correlation length $L_c^{\perp}$ ($\triangle$) (resp. $L_c^{\parallel}$ ($\diamond$)) is plotted as a function of the specimen width (resp. the specimen length). The slope of the dashed line is 0.15.

2D scaling properties : In chapter 2, we have shown that the analysis of profiles parallel to the z-axis was insufficient to fully describe the 2D scaling properties of fracture surfaces. The full characterization calls for the use of the 2D height−height correlation function.

We will now use the same type of analysis to study the 2D properties of the sandstone fracture surfaces in order to determine whether their properties are isotropic or not. Figure 3.16 displays the 1D correlation functions $\Delta h(\Delta z)$ and $\Delta h(\Delta x)$ computed along the crack front (z-axis) and parallel to crack growth (x-axis), respectively (sample width $L = 14$ mm). Both variations can be fitted to a power-law. However, the curves do not exactly coincide. The roughness amplitude is slightly larger along the crack front direction. This has been systematically observed on all samples. Moreover, the scaling exponents corresponding to the slope of the power-law fits performed

in the self-affine domains [d, $L_c^{\perp}$] and [d, $L_c^{\parallel}$] are found to be slightly different: The roughness exponent $\zeta = 0.46$ measured parallel to the direction of the crack front is found to be slightly smaller than $\beta = 0.50$ measured along the direction of the crack growth. However, fluctuations of the same order of magnitude as the value of these exponents are observed for samples of different widths – ζ_{1D} and β_{1D} measured on each sample are listed in Table 3.3. The difference measured between the two scaling exponents is therefore not large enough to determine whether the surfaces are isotropic or not. As shown in Chapter 2, the analysis of the 2D correlation function brings more precise information because it involves a larger statistical ensemble.[6]

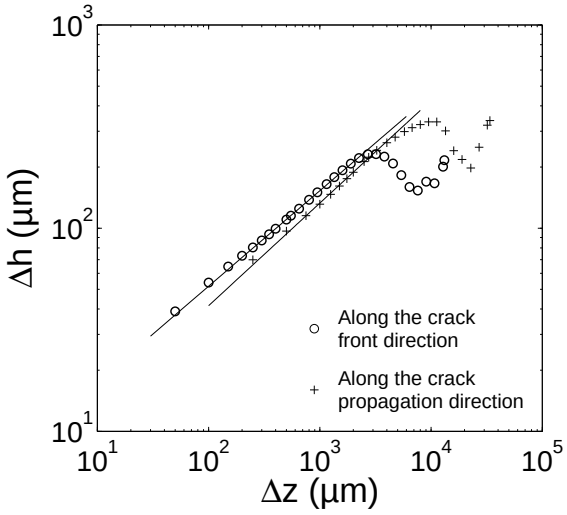


Figure 3.16: 1D height−height correlation functions measured parallel to the direction of crack propagation and to the crack front for the surface of a fractured sandstone sample with $L = 14$ mm. The straight lines are power-law fits in the self-affine domain for $\Delta z > d \simeq 240$ μm. The scaling exponents, corresponding to the slope of these lines, are respectively equal to 0.46 and 0.50 parallel to the crack front and to the crack propagation.

The 2D correlation function computed on the sandstone fracture surface analyzed previously is shown in the insets of Fig. 3.17. At first, we look for the two exponents β and z that optimize the collapse of the curve after normalization of the axis using the Eq. (2.5). These are found to be $\beta = 0.43$ and $z = 0.90$. The obtained collapse is shown in Fig. 3.17 a. As a comparison, one sets z equal to unity, and looks for the value of β that optimizes the collapse, also following the Eq. (2.5). The best possible

[6]If the surface studied is composed of $n \times n$ data points, the method based on the power-law fit of the 1D correlation function involves about n points ($\Delta h(\Delta r)$) each computed as the mean of n^2 experimental points while the method based on the calculation of the 2D correlation function involves the collapse of n^2 points ($\Delta h(\Delta z, \Delta x)$) each computed from n^2 experimental points.

collapse, obtained for $\beta = 0.47$, is shown on Fig. 3.17 b. The good collapse of the curves obtained using the first procedure (figure a) and the poorer one obtained in the second case by setting $z = 1$ (figure b) suggests that the anisotropy effect indeed exists and that the 2D correlation function follows the Family−Vicsek scaling given in Eq. (2.5) with $z < 1$. According to Eq. (2.5), the roughness exponent corresponds to the scaling exponent of the power-law regime of the collapsing curve. By fitting the experimental variations, one obtains $\zeta = 0.43$. Computing the 2D correlation function on the other fracture surfaces of samples with other widths, one observes systematically that the exponent ζ is smaller than β.[7] In addition to ζ_{1D} (resp. ζ_{FT}) and β_{1D} (resp. β_{FT}) calculated from the calculation of the 1D correlation function (resp. 1D Fourier power spectrum) of each investigated surface, the two exponents β_{2D} and z that optimize the collapse of the curves as well as the exponent ζ_{2D} corresponding to power-law behavior of the collapsing curve are listed in Table 3.3. Compiling the three different techniques, one finds $\zeta = 0.45 \pm 0.06$, $\beta = 0.48 \pm 0.05$ and $z = 0.97 \pm 0.08$.

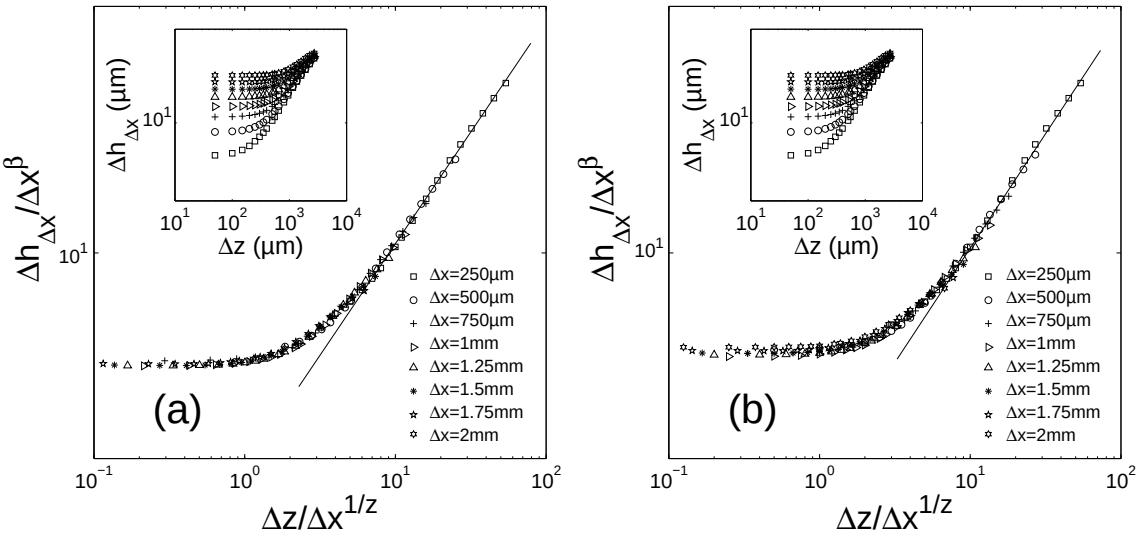


Figure 3.17: Normalized 2D variations with Δz of the height−height correlation function at various values of Δx for the surface of the fractured sandstone sample of width $L = 14$ mm: (a) $\beta = 0.50$ and $z = 0.90$ are chosen to optimize the data collapse using Eq. (2.5). The straight line that corresponds to the fit of the power-law regime of the collapsing function has a slope of $\zeta = 0.43$; (b) Best data collapse obtained by setting $z = 1$.

[7] Even though their values lie within the error bars of each of them.

3.5 Concluding remarks

In this chapter, the morphology of fracture surfaces of materials made of cemented grains has been investigated. This study was motivated by the observation of a roughness exponent $\zeta \simeq 0.4 - 0.5$ on sandstone fracture surfaces [2, 35] much lower than the universal roughness exponent $\zeta \simeq 0.75$ (see Chapter 2). A series of fractured glass ceramics samples realized by the same process but displaying very different characteristics (porosity, grain size, fracture propagation velocity) has been studied systematically: The fact that the same roughness exponent was found in these materials as in natural sandstone samples in a broad range of porosities ($3\ \% < \phi < 26\ \%$) and of grain diameters ($50\ \mu\text{m} < d < 240\ \mu\text{m}$) has demonstrated the robustness of this low value.

More precisely, fracture surfaces of artificial and natural sandstone were observed to exhibit self-affine properties with a roughness exponent $\zeta \simeq 0.42 \pm 0.05$ measured along the crack front direction in both the quasi-static and rapid failure regimes. Moreover, the fracture surfaces investigated were shown to display clear Gaussian distribution of the height variation in the self-affine domain of length scales ranging from the grain size to a given fraction of the sample width. In other words, the whole geometry of profiles parallel to the crack front is entirely described by one exponent up to a cut-off length scaling with the system size. The two-dimensional geometry of the two-dimensional fracture surface is rather more complex: Profiles parallel to the crack growth direction are also mono-affine with Gaussian height fluctuations but characterized by a slightly larger scaling exponent $\beta \simeq 0.48 \pm 0.05$. More generally, these anisotropic fracture surfaces are well described by their 2D height−height correlation function that follows a Family−Vicsek scaling (see Eq. (3.1)).

The roughness amplitude was observed to depend very weakly on both the fracture test geometry and the crack growth velocity, and to increase linearly with both the grain diameter and the porosity. This result suggests that the transition from trans- to inter-granular fracture propagation that occurs with increasing porosity does not affect the value of the scaling exponents.

In the following chapter, we will suggest an explanation for the observed low value of the roughness exponent. In particular, we will explain why the materials studied in Chapter 2 display a roughness exponent $\zeta \simeq 0.75$ and while those studied in chapter 4 display a lower value $\zeta \simeq 0.4$. As a starting point, we will study the propagation of a crack in a perfectly brittle heterogeneous material and will give the properties of the fracture surface roughness expected in that case. The effect of the damage at the crack tip on the fracture surface morphology will be also discussed.

Chapter 4

Fracture surfaces for model linear elastic disordered materials

Contents

4.1 Model of crack propagation in ideal linear elastic disordered materials 72

4.2 Fracture surface of porous materials: Interpretation . . 82

4.3 Fracture surfaces of other brittle materials 97

4.4 Fracture surfaces of ductile materials : Interpretation . 101

In the previous chapters, the minimal set of relevant parameters necessary to characterize the 2D scaling properties of fracture surfaces was identified: Their 2D scaling properties can be described by the so-called Family−Vicsek scaling characterized by two independent roughness exponents, ζ and β, measured respectively perpendicularly and parallel to the direction of the crack growth. The second important experimental result is the existence of *two* sets of exponents, namely $\zeta \simeq 0.75$ and $\beta \simeq 0.60$ for fractured aluminum alloy, silica glass, mortar, wood and quasi-crystal samples and $\zeta \simeq 0.40$ and $\beta \simeq 0.50$ for glassy ceramics and sandstone samples. The value of the exponents is robust as it depends neither on the crack growth velocity[1] nor on the details of the microstructure. This suggests the existence of, at least, *two* universality classes for failure problems in heterogeneous materials.

These experimental observations raise many questions: What is the origin of these two universality classes? What is the origin of their universal properties? The peculiar rupture mode of glass ceramics is a key element: In these materials, the crack is expected to propagate by breaking the solid bridges between the sintered grains sequentially, one after the other. In other words, the fracture of glass ceramics reproduces at the scale of the bead diameter the "classical" picture of perfectly brittle

[1] In the quasi-static limit.

rupture [8]. Annex A is devoted to the study of the mechanical properties of glass ceramics. Strong arguments in favor of a scenario of brittle fracture in these materials are given there. This suggests that a model of crack propagation in an ideal perfectly linear elastic brittle disordered material could explain the experimental measurements of Chapter 3. In the first section of this chapter, we will predict within the Linear Elastic Fracture Mechanics (LEFM) framework the surface properties of these ideal materials. We will show that - in this framework - fracture surfaces are expected to be anisotropic and to satisfy the Family−Vicsek scaling. Moreover, the predicted exponents are $\zeta = 0.39$ and $\beta = 0.49$, in very good agreement with the experimental observations reported for glass ceramics and sandstone samples. In the second section, model and experimental measurements will be compared *quantitatively*. The assumptions performed to predict theoretically the surface properties will be confronted independently with experiments. This analysis will establish the extent up to which the theoretical model describes the fracture of sandstone and glass ceramics. Finally, the second universality class $\{\zeta \simeq 0.75$ and $\beta \simeq 0.6\}$ for failure problems will be investigated. As the archetype of minimal elastic material, the fracture of silica glass will be studied in detail: Mechanisms that are not taken into account in the theoretical description of brittle fracture will be shown to take place at length scales consistent with those at which the self-affinity with exponents $\zeta \simeq 0.75$ and $\beta \simeq 0.60$ is observed. In other words, the geometry of surfaces of fractured silica glass at the nanometer scale does not result from brittle failure. The case of the aluminum alloy, mortar, wood and quasi-crystal fracture will be also discussed. A scenario where damage processes play a central part is suggested to explain the value of the exponents measured on these materials.

4.1 Model of crack propagation in ideal linear elastic disordered materials

The objective of this section is to predict the morphology of crack surface in a perfectly linear elastic disordered material. In the next section, the predictions will be compared to the experimental results obtained for glass ceramics representing a good example of such a material (see Annexe A). We consider a single crack propagating in an ideal linear elastic disordered material. We restrict the following analysis to the case where the crack speed is small enough compared to the sound speeds[2] in the material so that the quasi-static approximation is relevant. We will focus here on a mode I loading corresponding to the experimental situations studied in chapter 2 and 3. The crack front (oriented along the z-axis) is thus confined roughly to a plane (x, z) perpendicular to the tensile forces (along the y-axis) and propagates along the x-axis. In a homogeneous material, the crack would propagate at uniform velocity and would

[2]Speed of longitudinal, transverse and Rayleigh waves.

lead to a planar fracture surface (the plane (z, x)). But the heterogeneities of the material induce both *in-plane* (along x) and *out-of-plane* (along y) perturbations of the shape of the edge. Schematic views of the in-plane $f(z,t)$ and out-of-plane

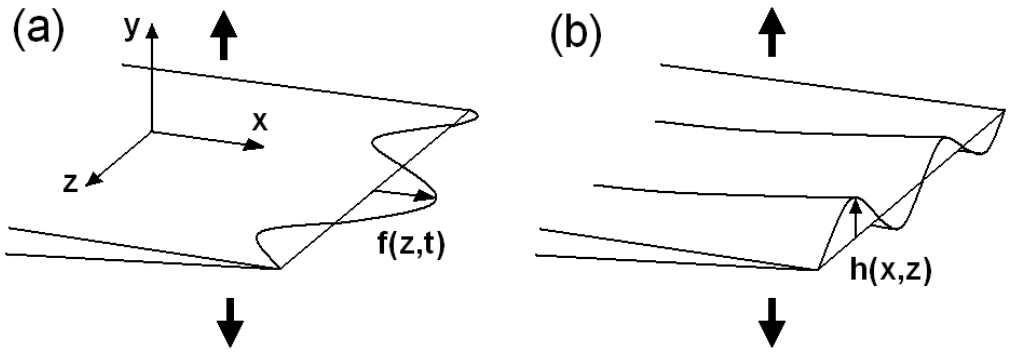


Figure 4.1: Geometry of perturbed cracks subject to mode I loading (large arrows indicating the direction of macroscopic loading). (a): In-plane perturbations. (b): Out-of-plane perturbations. The shape of the fracture surface is effectively the history of the out-of-plane perturbations of the crack front. (Taken from Ref. [40]).

$h(x = x_0 + f(z,t), z)$ displacements are shown in Fig. 4.1. For simplicity, the out-of-plane perturbations are represented for a crack front without in-plane perturbations ($f(z,t) = 0$). The fracture surface is the print of the out-of-plane perturbations $h(x,z)$ of the crack front. In the following, we will see that, for small enough perturbations, the out-of-plane displacements are independent of the in-plane displacements so that the shape of the fracture surface can be predicted independently of $f(z,t)$. This implies that the dynamical properties of the crack – the local velocities of the crack front $\frac{\partial f}{\partial t}(z,t)$ – are decoupled from the crack trajectory $h(x,z)$. An experimental argument based on the analysis of fracture surfaces will also support this statement (see Section 4.2).

Stress field in the vicinity of a slightly perturbed crack front : We consider now a point M of the crack front characterized by its position $(x = x_0 + f(z,t), y = h(x,z), z)$. The local stress field around M determines its trajectory. The stress at a distance r ahead of the point M in the direction θ can be written as the sum of the contributions of each of the three fracture modes (see Section 1.1), each mode being developed as a $r^{k/2}$ expansion with $k \geq -1$

$$\sigma_{ij} = \sum_{p=I}^{III} \frac{K_p}{\sqrt{2\pi r}} g_p^{ij}(\theta) + T_p k_p^{ij}(\theta) + A_p l_p^{ij}(\theta)\sqrt{r} + ... \tag{4.1}$$

where K_p (the so-called stress intensity factors), T_p (T-stress) and A_p are constants depending on the loading and the geometry of the sample. g_p^{ij}, k_p^{ij} and l_p^{ij} are universal

functions of θ (see Eq. (1.2) for the complete expression of $g_I^{ij}(\theta)$ for example).

Even though we focus here on a dominantly mode I loading situation, K_{II} and K_{III} are not equal to zero. The perturbations h and f of the crack shape induce small shearing loading around the crack front. Assuming h and f to be small, the value of the stress intensity factors K_p can be developed to first order as

$$K_I = K_I^{(0)} + K_I^{(1)} + ... \tag{4.2}$$

$$K_{II} = K_{II}^{(0)} + K_{II}^{(1)} + ... \tag{4.3}$$

$$K_{III} = K_{III}^{(0)} + K_{III}^{(1)} + ... \tag{4.4}$$

The first terms $K_p^{(0)}$ in these developments are equal to the stress intensity factors in the unperturbed planar case with a straight crack front while the second terms $K_p^{(1)}$ in the developments are linear in h or f. We assume that the perturbations f and h are small so that terms of higher order than 1 can be neglected. $K_p^{(0)}$ is set by boundary loading conditions supposed far from the crack front. The external loading is of mode I type so that $K_I^{(0)} = K_I^{\text{ext}}$ and $K_{II}^0 = K_{III}^0 = 0$. The dependence of the term $K_I^{(1)}$ on f has been studied in Ref. [74] and then in Ref. [75]. The terms $K_{II}^{(1)}$ and $K_{III}^{(1)}$ were analyzed in Ref. [76]. They showed the existence of two terms depending on h. The study of Mochvan *et al.* [77] confirmed only the form of the first one. The second term, so-called "memory term" because it gives the dependence of the stress intensity factor with the whole shape of past trajectory of the crack front, was shown to be much more complicated than the expression proposed in Ref. [76]. The authors derived also an another term linear in h (the last term of Eq. (4.6)). All these results calculated through linear elasticity for an infinite sample of Poisson's ratio ν broken under a mode I loading in the quasi-static limit can be summarized as

$$K_I = K_I^{(0)} + \frac{K_I^{(0)}}{2\pi} \int_{-\infty}^{+\infty} \frac{f(z') - f(z)}{(z'-z)^2} dz' \tag{4.5}$$

$$K_{II} = \frac{K_I^{(0)}}{2} \frac{\partial h}{\partial x} - \frac{K_I^{(0)}}{2\pi} \frac{2-3\nu}{2-\nu} \int_{-\infty}^{+\infty} \frac{h(x,z') - h(x,z)}{(z'-z)^2} dz' + \Delta K_{II}^{\text{memory}} + \sqrt{\frac{\pi}{2}} A_I h(x,z) \tag{4.6}$$

$$K_{III} = K_{III}^{(1)}(h, z, K_I^{(0)}) \tag{4.7}$$

where the "memory" term K_{II}^{memory} is given by

$$\begin{aligned} \Delta K_{II}^{\text{memory}}(x,z) &= -\int_{-\infty}^{x} \int_{-\infty}^{+\infty} \left\{ w_x^{II}(x-x', z-z') \left(\frac{\partial (hT_{xx})}{\partial x}|_{(x',z')} + \frac{\partial (hT_{xz})}{\partial z}|_{(x',z')} \right) \right. \\ &+ \left. w_z^{II}(x-x', z-z') \left(\frac{\partial (hT_{xz})}{\partial x}|_{(x',z')} + \frac{\partial (hT_{zz})}{\partial z}|_{(x',z')} \right) \right\} dx' dz' \end{aligned} \tag{4.8}$$

with

$$\begin{aligned} w_x^{II}(x,z) &= \frac{\sqrt{-2x}H(x)}{\pi^{3/2}*(x^2+z^2)}\left(1+\frac{2\nu}{2-\nu}\frac{1-(z/x)^2}{1+(z/x)^2}\right) \\ w_z^{II}(x,z) &= \frac{\sqrt{-2x}H(x)}{\pi^{3/2}*(x^2+z^2)}\frac{2\nu}{2-\nu}\frac{2z/x}{1+(z/x)^2} \end{aligned} \tag{4.9}$$

where $H(x)$ is the Heaviside function.

Equation of the crack path in a homogeneous material : From these three equations and Eq. (4.1), one can calculate the diverging part of the stress field in the vicinity of a crack front for given distortions h and f. This stress field determines the crack trajectory. Indeed, the path chosen by a crack propagating in an elastic isotropic material is the one for which the local stress field is of mode I type ("criterion of local symmetry" [9, 10, 11]).[3] In other words, the net mode II stress intensity factor should vanish in each location z along the crack front and any position x of the mean line. Taking the right part of Eq. (4.6) equal to zero, one gets

$$\frac{\partial h}{\partial x} = \frac{1}{\pi}\frac{2-3\nu}{2-\nu}\int_{-\infty}^{+\infty}\frac{h(x,z')-h(x,z)}{(z'-z)^2}dz' - 2\frac{\Delta K_{II}^{\text{memory}}}{K_I^{\text{ext}}} - \frac{A_I}{K_I^{\text{ext}}}\sqrt{2\pi}h \tag{4.10}$$

This means that the path – the angle $\frac{\partial h}{\partial x}(x,z)$ – followed by the crack in $M = (x, h(x,z), z)$ depends only on the out-of-plane perturbation h of the crack shape. This represents an important simplification of the problem because the knowledge of the in-plane displacement f is not necessary to predict to first order the fracture surface morphology. Moreover, Eq. (4.10) is time independent. In other words, this so-called *path equation* predicts the path followed by the crack is independent of the dynamics of the propagation. The dynamics, *i.e.* the local velocities of the crack front, is described by a decoupled *equation of motion* satisfied by f.

In the right part of Eq. (4.10), three terms are involved: The first one gives the dependence of the crack path on the full shape of the crack front at its current position x. The second term shows that the crack keeps the "memory" of the path followed in the past, its contribution resulting from an integral over the crack front shape on all x' and z' values such as $x' \leq x$ (see Eq. (4.8)). Finally, the third contribution is purely local and depends only on the position $h(x,z)$ of the point M. These three contributions are in fact not equivalent. In order to compare the various terms involved in the right part of Eq. (4.10), one calculates their Fourier transform. Denoting by $\hat{h}(k_x,k_z)$, $\hat{w}_x^{II}(k_x,k_z)$, and $\hat{w}_z^{II}(k_x,k_z)$ the Fourier transform of $h(x,z)$, $w_x^{II}(x,z)$, and $w_z^{II}(x,z)$, respectively, the first term leads to $\frac{2-\nu}{2-3\nu}|k_z|\,\hat{h}(k_x,k_z)$, the second to

[3]The "criterion of local symmetry" was proposed to predict the crack path for two-dimensional problems invariant along the z-axis. In the three-dimensional case treated here, we make the assumptions – widely used in the literature [41, 40] – that the crack only propagates along the x-axis and that the criterion of local symmetry is still valid. This assumption neglects the effects of the mode III contribution for which we ignore until now the consequence on the crack path.

$\left[\hat{w}_x^{II}(k_x,k_z)\left(\frac{T_{xx}}{K_I^{\rm ext}}k_x+\frac{T_{xz}}{K_I^{\rm ext}}k_z\right)+\hat{w}_z^{II}(k_x,k_z)\left(\frac{T_{xz}}{K_I^{\rm ext}}k_x+\frac{T_{zz}}{K_I^{\rm ext}}k_z\right)\right]2i\hat{h}(k_z,k_x)$[4] and the third one to $-\sqrt{2\pi}\frac{A_I}{K_I^{\rm ext}}\,\hat{h}(k_x,k_z)$. The ratio – in absolute value – of the second and the third term to the first one leads to[5]

$$\frac{(2)}{(1)}\leq\frac{(|T_{xx}|+2|T_{xz}|+|T_{zz}|)\,\sqrt{c}}{K_I^{\rm ext}}\left(\frac{1}{\sqrt{|k_x|c}}+\frac{1}{\sqrt{|k_z|c}}\right)\qquad\frac{(3)}{(1)}\simeq\frac{|A_I|\,c}{K_I^{\rm ext}}\frac{1}{|k_z|c}\quad(4.11)$$

Thus, as soon as the scale of interest $\Delta z=\frac{2\pi}{k_z}$ along the crack front is smaller than a typical length scale c of the system, *e.g.* the crack length, the first term is dominant compared to the third one.[6]

This is a great simplification because the path followed by the crack depends only, to first order, on the perturbation of the crack edge and does not keep memory on its past, *i.e.* of its trajectory. Let us note that the term $\frac{\partial h}{\partial x}$ is of the same order than (1) that's why it is also relevant compared to (2) and (3). A direct experimental confirmation of this hierarchy will be given in Section 4.2.

Effect of the imperfect mode I loading : Until now, the model predicting the crack path, and especially the stress field in the vicinity of the crack tip, has been

[4] T_{xx}, T_{zz} and T_{xz} have been supposed to have weak dependence in x and z compared to h so that the second term in the expressions $\frac{\partial hT_{ij}}{\partial x}=T_{ij}\frac{\partial h}{\partial x}+h\frac{\partial T_{ij}}{\partial x}$ and $\frac{\partial hT_{ij}}{\partial z}=T_{ij}\frac{\partial h}{\partial x}+h\frac{\partial T_{ij}}{\partial x}$ can be neglected in Eq. (4.8). In view of the important fluctuations of height, this assumption seems justified.

[5] The details of the calculation of the Fourier transform (2) of the second term in Eq. (4.10) are the following. First, the calculation of the Fourier transform of w_x^{II} and w_z^{II} leads to $\hat{w}_x^{II}=\frac{1}{\sqrt{|k_x|}}\alpha(\frac{k_z}{k_x})$ and $\hat{w}_z^{II}=\frac{1}{\sqrt{|k_x|}}\beta(\frac{k_z}{k_x})$ with $\alpha(X)=\int\int_{-\infty}^{+\infty}e^{-iu}e^{-ivX}w_x^{II}(u,v)dudv$ and $\beta(X)=\int\int_{-\infty}^{+\infty}e^{-iu}e^{-ivX}w_z^{II}(u,v)dudv$. Numerical integration of the preceding expressions leads to $\alpha(X)\overset{X\sim 0}{\sim}\beta(X)\overset{X\sim 0}{\sim}X$, $\alpha(X)\overset{X\sim 1}{\sim}\beta(X)\overset{X\sim 1}{\sim}1$ and $\alpha(X)\overset{X\sim+\infty}{\sim}\beta(X)\overset{X\sim+\infty}{\sim}\frac{1}{\sqrt{X}}$. Therefore, one deduces the asymptotic behaviors (2) $\overset{k_z\ll k_x}{\sim}\frac{k_z}{K_I^{\rm ext}}\left(\frac{T_{xx}+T_{xz}}{\sqrt{|k_x|}}+\left(\frac{k_z}{k_x}\right)\frac{T_{xz}+T_{zz}}{\sqrt{|k_x|}}\right)\simeq k_z\frac{(T_{xx}+T_{xz})\sqrt{c}}{K_I^{\rm ext}}\frac{1}{\sqrt{|k_x|c}}$, (2) $\overset{k_z\sim k_x}{\sim}k_z\frac{(T_{xx}+2T_{xz}+T_{zz})\sqrt{c}}{K_I^{\rm ext}}\frac{1}{\sqrt{|k_z|c}}$ and (2) $\overset{k_z\gg k_x}{\sim}\frac{k_z}{K_I^{\rm ext}}\left(\frac{T_{xz}+T_{zz}}{\sqrt{|k_z|}}+\left(\frac{k_x}{k_z}\right)\frac{T_{xx}+T_{xz}}{\sqrt{|k_z|}}\right)\simeq k_z\frac{(T_{xz}+T_{zz})\sqrt{c}}{K_I^{\rm ext}}\frac{1}{\sqrt{|k_z|c}}$. Finally, whatever the value of k_x and k_z, one gets $(2)\leq k_z\frac{(|T_{xx}|+2|T_{xz}|+|T_{zz}|)\sqrt{c}}{K_I^{\rm ext}}\left(\frac{1}{\sqrt{|k_x|c}}+\frac{1}{\sqrt{|k_z|c}}\right)$. This leads to the ratio $\frac{(2)}{(1)}$ given in Eq. (4.11).

[6] We assume here that both $T_{ij}\sqrt{c}$ and A_Ic are of the same order as the applied stress intensity factor $K_I^{\rm ext}$. For example, considering for pedagogical reasons the case of the semi-infinite sample with a notch and submitted to a constant loading $\sigma_{\rm ext}$, one can show [78] that $K_I^{\rm ext}=\sqrt{\pi c}\,\sigma_{\rm ext}$, $T_{xx}\sqrt{c}=T_{zz}\sqrt{c}=-(1-\nu)\sigma_{\rm ext}$, $T_{xz}=0$ and $A_I=0$. This leads to ratios in Eq. (4.11) inferior to one for all length scales Δx and Δz smaller than the crack length c. In this geometry, the terms (2) and (3) of Eq. (4.10) are negligible at all length scales. Finite element calculations have shown that this result can be generalized to various geometries, and in particular remains valid for the fracture test geometries used experimentally for the work of chapter 3.

derived in the ideal case of a mode I loading ($K_I^{(0)} = K_I^{\text{ext}}$ and $K_{II}^{(0)} = K_{III}^{(0)} = 0$). From an experimental point of view, a pure mode I loading is hypothetic. Resulting from unavoidable imperfections of the loading system or in crack alignment, the sample is submitted to small mode II and mode III loadings that imply $K_{II}^{(0)} = K_{II}^{\text{ext}}$ and $K_{III}^{(0)} = K_{III}^{\text{ext}}$ that are small compared to K_I^{ext}. In particular, the expression of K_{II} given in Eq. (4.6) does not reduce to the lonely term $K_{II}^{(1)}$. Another term $K_{II}^{(0)} = K_{II}^{\text{ext}}$ has to be added. Using the same argument as in the previous paragraphs to derive the path of the crack front ($K_{II} = 0$), one gets

$$\frac{\partial h}{\partial x} = \frac{1}{\pi}\frac{2-3\nu}{2-\nu}\int_{-\infty}^{+\infty}\frac{h(x,z') - h(x,z)}{(z'-z)^2}dz' + F_0 \tag{4.12}$$

where $F_0 = -2\frac{K_{II}^{\text{ext}}}{K_I^{\text{ext}}}$. Although this term is very small[7], we will see in the next paragraphs that it is relevant for setting the scaling properties of fracture surfaces.

Effect of disorder : Until now, the elastic material has been considered as perfectly homogeneous. In that case, we have shown that the out-of-plane displacement of the crack front - which determines the shape of the fracture surface - satisfies Eq. (4.10) where the two last terms can be neglected at small scales compared to the system size. The second term of this equation acts as a restoring force: Any perturbation of the straight crack vanishes and the resulting fracture surface is flat.[8] The elasticity competes with the effect of the disorder which makes the crack front rough: Even though elasticity theory predicts a straight propagation of the crack front, the disorder of the material can favor some directions because they correspond to "weak planes" in which the bonds are easier to break. In other words, the crack front takes advantage of the disorder of the material by wandering between stronger zones. One can model this effect by adding a new term K_{II}^{dis} to the stress intensity factor in mode II in Eq. (4.6). Using then the equation of trajectory $K_{II} = 0$, one gets another term $\eta = 2\frac{K_{II}^{\text{dis}}}{K_I^{(0)}}$ in Eq. (4.10). In other words, the direction of propagation of a point M of the crack $\frac{\partial h}{\partial x}$ predicted by the linear elasticity deviates from $\eta(x, h(x,z), z)$ because of the disorder. This additional noise depends on the position of this point M and has a zero mean value since the heterogeneities of the material do not favor particularly the deviation of the crack front toward either positive or negative h values. Finally, from

[7] From the measurement of the slight deviation α of the mean plane of the fracture surface with respect to the plane perpendicular to the direction of the external mode I loading, it is possible to estimate $F_0 = -2\frac{K_{II}^{\text{ext}}}{K_I^{\text{ext}}} = -3\alpha$. Measured values of $\alpha \simeq 2\,^\circ$ leads to $|F_0| \simeq 0.07$.

[8] The presence of the first term in the right part of Eq. (4.10) ensures the stability of the crack for perturbations of small sizes. To ensure the stability of the crack with respect to perturbations of all sizes, the second term is required. This stability condition is fulfilled if the T-stress is negative [10].

Eq. (4.10) derived for a homogeneous material, one obtains the following equation for the crack trajectory

$$\frac{\partial h}{\partial x} = A(\nu) \int_{-\infty}^{+\infty} \frac{h(x,z') - h(x,z)}{(z'-z)^2} dz' + \eta(x, h(x,z), z) + F_0 \qquad (4.13)$$

where $A(\nu) = \frac{1}{\pi} \frac{2-3\nu}{2-\nu}$ is a constant depending only on the Poisson's ratio of the material.

It must be emphasized that time does not play any role in this equation. In particular, the x coordinate is not necessarily proportional to time. Equation (4.13) only provide the path followed by the crack but give no information on the time dependence of the crack front position. In contrast with models as in [36] where the fracture surface is described as the trace left by the crack front, the dynamics of which is described through a Langevin equation, the *path* equation proposed here gives no information on the motion – the dynamics – of the crack front. The important consequences for the expected fracture surface morphology are discussed in the following.

Family−Vicsek scaling of fracture surfaces : Equation (4.13) describes the path followed by a crack in a brittle disordered material in the quasi-static limit for small perturbations h and at small scales compared to the system size. Its solution $h(x,z)$ is the map of the heights of the fracture surface under these hypotheses.

This equation describes the propagation of an elastic line in a random potential. A general property of the solution of such equations is already known [39, 38]: $h(x,z)$ follows the so-called Family−Vicsek scaling [66]

$$\langle (h(x+\Delta x, z+\Delta z) - h(x,z))^2 \rangle_{x,z}^{1/2} \sim \Delta x^{\beta} g(\Delta z / \Delta x^{1/z}) \qquad (4.14)$$

where $g(u)$ is a scaling function equal to a constant when $u \ll 1$ and to u^{ζ} when $u \gg 1$. The roughness exponent ζ, the growth exponent β and the dynamic exponent z are related by $\zeta = \beta z$. The general solution of this equation is in agreement with the 2D scaling properties of fracture surfaces: They follow the Family−Vicsek scaling and are characterized by two different exponents ζ and β, perpendicularly and parallel to the crack growth direction, respectively. In other words, fracture surfaces resulting of brittle failure are expected to be anisotropic.

The properties of the noise $\eta(x,h,z)$ will set the value of these scaling exponents. Equations similar to Eq. (4.13) are rather well understood in cases where 2D random potentials – either $\eta(x,z)$ or $\eta(h,z)$ – are involved. But the effect of a 3D random potential $\eta(x,h,z)$ on the value of the scaling exponents is still an open question. In the next paragraph, we will give simple arguments that demonstrate some links between the two problems. They will be used to interpret the value of the experimental exponents measured on fracture surfaces of brittle materials but cannot be considered as sufficient to solve the difficult theoretical question of the line propagation in a 3D random potential.

Quenched versus thermal disorder : We focus here on the properties of the 3D random potential. Although its three arguments are the three variables of space, they are not equivalent. In particular, the variable x may be considered as representing time because it does not play any explicit role in Eq. (4.13). In this, the noise $\eta(x,h,z)$ do not appear as a three dimensional quenched noise[9], but rather as a two-dimensional noise $\eta(h,z)_x$ slowly varying with an effective "time" x.

In the following, we will use qualitative arguments to assess roughly the relative contribution of the quenched and thermal fluctuations. At first, let's analyze the variations of the noise η when a point $M(x_0,h_0,z_0)$ of the crack front is moving forward in the plane $(x,\ z)$[10] to another point $M'(x_0+\Delta x, h_0+\Delta h, z_0)$ (see Fig. 4.2). According to Eq. (4.14), when the point M of the crack front propagates over a distance Δx along the x-axis, its typical height moves over a distance $\Delta h = \ell_x^{1-\beta}\Delta x^\beta$ along the h-axis.[11] As a result, the variation of the normalized noise $\overline{\eta} = \frac{\eta}{\sqrt{<\eta^2>}}$ felt by the crack tip for a small increment Δx is

$$\overline{\eta}(M') - \overline{\eta}(M) = \vec{\bigtriangledown}\overline{\eta}_M.d\vec{M} = \frac{\partial\overline{\eta}}{\partial x}dx + \frac{\partial\overline{\eta}}{\partial h}dh = \frac{\partial\overline{\eta}}{\partial r}(dx + \ell_x^{1-\beta}dx^\beta) \simeq \frac{dx}{r_\eta} + \frac{\ell_x^{1-\beta}dx^\beta}{r_\eta} \tag{4.15}$$

The first term in the noise variation plays the role of the "thermal" contribution to the fluctuations while the second one corresponds to the "quenched" contribution. We consider here an isotropic material so that the spatial correlation length r_η of the noise $\eta(x,h,z)$ is the same in all directions. Thus, the gradient of the normalized noise $\frac{\partial\overline{\eta}}{\partial r} \simeq \frac{1}{r_\eta}$ is also the same in all directions.

Let's consider now a point M propagating over the distance r_η along the x-axis. It will thus feel a normalized "thermal" fluctuation of the order of unity. According to Eq. (4.15), it will also undergo a "quenched" fluctuation of amplitude $\frac{\ell_x^{1-\beta}r_\eta^\beta}{r_\eta}$ caused by its propagation along the h-axis. This incremental path is represented Fig. 4.2. As a consequence, the ratio $(\frac{r_\eta}{\ell_x})^{1-\beta}$ is a good estimate for the relative strength of the thermal noise compared to the quenched noise. Assuming that the noise η can be written without loss of generality as the sum of its thermal and quenched contribution, Eq. (4.13) becomes

$$\frac{\partial h}{\partial x} = A(\nu)\int_{-\infty}^{+\infty}\frac{h(x,z')-h(x,z)}{(z'-z)^2}dz' + \eta_q(h,z) + \eta_t(x,z) + F_0 \tag{4.16}$$

with $\langle\eta_q(h,z)\,\eta_q(h',z')\rangle = D\,\Delta(h-h')\,\Delta(z-z')$ and $\langle\eta_t(x,z)\,\eta_t(x',z')\rangle = D\,(\frac{r_\eta}{\ell_x})^{2(1-\beta)}$

[9]The expressions "quenched" and "thermal" will be used here to designate a noise that depends on the position and the time respectively.

[10]Using the "criterion of local symmetry" that is a two-dimensional criterion to derive the Eq. (4.13), we limited previously our model to cracks for which all the points of the front propagate in the plane (x,y). Motion along the z-axis are in fact forbidden.

[11]We use here the topothesy ℓ_x, or scale at which Δh is equal to Δx, in order to work with equalities and not proportionality relations.

$\Delta(x-x')\,\Delta(z-z')$. Here, D is the strength of the disorder $\eta(x,h,z)$ and $\Delta(u)$ is a rapidly decreasing function of u for $u>0$ with $\Delta(0)=1$ and decays exponentially to zero over a distance r_η.[12] The experimental measurement of r_η (typical length scale of the disorder in the material) and ℓ_x (related to the roughness amplitude) are of the same order for glass ceramics so that thermal and quenched contributions of the noise are also of the same order. The consequences on the fracture surface morphology are now discussed.

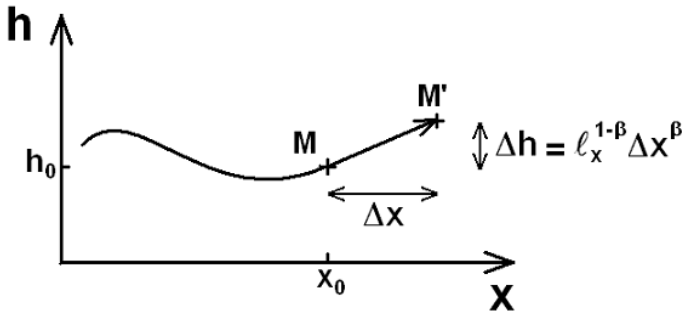


Figure 4.2: Trajectory of a point M of the crack front. While the point is moving over a distance Δx along the x-axis, it is also moving over the distance $\Delta h = l_x^{1-\beta}\Delta x^\beta$ along the y-axis (see Eq. (4.14)).

Fracture surface morphology : The morphology of the fracture surface is given by Eq. (4.13). We made the hypothesis that it can be written as Eq. (4.16). We have then shown that thermal and quenched noise have roughly the same amplitude. This last equation describes the motion of an elastic line $h(z)$ that "creeps" – the x coordinate playing the role of time – in a random potential η_q due to the thermal fluctuations η_t. The geometry of the line – and so the crack surface morphology – is described by its 2D correlation function $\Delta h(\Delta z,\Delta x)$ that follows a Family−Vicsek scaling (see Eq. (4.14)) involving two independent scaling exponents ζ and β. Let's focus at first on the value of ζ. Recent numerical works [79, 80] lead to the following picture: The line is characterized either by its properties at equilibrium ($\zeta_{\rm eq}=1/3$ [81]) or at the depinning threshold ($\zeta_{\rm dep}=0.39$ [82, 83]).[13] These properties are observed at different length scales and $\zeta_{\rm eq}=1/3$ (resp. $\zeta_{\rm dep}=0.39$) corresponds to small length scales (resp. large length scales). Moreover, one can also predict that the

[12] We suppose that the disorder is spatially uncorrelated in the material (see the discussion in Section 4.2).

[13] For an elastic line in a quenched random potential, the geometry that minimized its energy (elastic plus potential) is characterized by the roughness exponent at equilibrium $\zeta_{\rm eq}$. Considering now a line driven by an external constant force in a quenched potential, its motion is possible only for $F>F_c$. For $F=F_c$ corresponding to the depinning threshold, the line is characterized by the roughness exponent $\zeta_{\rm dep}$.

geometry of the line at very short distances is governed by its thermal fluctuations so that $\zeta = \zeta_{\rm th} = 0$ (logarithmic correlation of height). On the other hand, because of the finite velocity of the line, quenched disorder acts effectively as a thermal noise at very large length scales so that the roughness exponent is also $\zeta_{\rm th}$ at these distances [39]. These results can be summarized by the phase diagram shown in Fig. 4.3.

Two features of the equation governing the morphology of fracture surface are crucial here: (i) F_0 is very small so that the effect of the finite velocity (that tends to zero when the driving force tends to zero) acts at very large length scales; (ii) the thermal and quenched contributions of the noise are of the same order – at least for the case of glass ceramics – so that the effect of thermal fluctuations at short distances is confined to very small length scales.

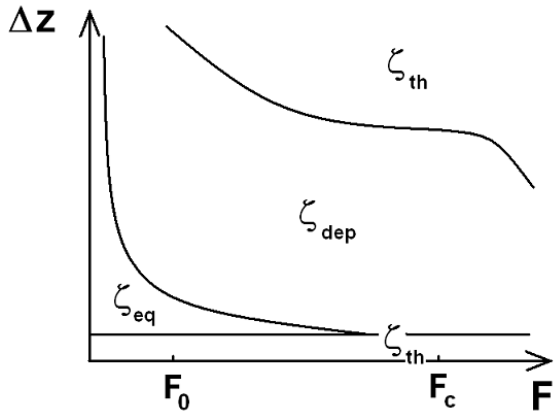


Figure 4.3: Phase diagram giving the geometry of an elastic line driven in random potential at finite temperature. The roughness exponent of the line -perpendicularly to the crack growth direction of the fracture surface - depends both on the length scale Δz and the driving force F. The relevant situation to predict the fracture surface morphology (Eq. (4.16)) corresponds to $F_0 \ll F_c$.

For these reasons, the expected roughness exponent resulting from the path equation of the crack front is $\zeta_{\rm eq}$ at small length scales and $\zeta_{\rm dep}$ at larger ones. Therefore, the large scale exponent expected on fracture surfaces of brittle materials corresponds to the one measured at the pinning/depinning transition ($\zeta_{\rm dep} = 0.39$). The corresponding growth and dynamic exponents are $\beta \simeq 0.50$ and $z \simeq 0.80$, respectively [84]. Their values coincide, within the error bars, with the experimental measurements $\zeta = 0.42 \pm 0.05$ and $\beta = 0.48 \pm 0.05$ made on glass ceramics and sandstone fracture surfaces, that are archetypes of brittle materials (see Annexe A).

Concluding remarks : Within the framework of the linear elastic fracture mechanics, we have shown that a single crack propagating quasi-statically in a brittle

material leads to a self-affine fracture surface with, at large scales, a roughness exponent $\zeta = 0.39$.[14] According to Eq. (4.14), the two-dimensional scaling of the fracture surface is also predicted: Its anisotropic scaling properties are characterized by a slightly larger scaling exponent $\beta = 0.50$ along the crack propagation direction. Its 2D correlation function is expected to follow Family−Vicsek scaling. These results are in agreement with the experimental measurements made on glass ceramics, archetype of brittle material, at least at scales larger than their bead size (see Annex A). We now compare the predictions of our theoretical model with the experimental facts on fracture surfaces established in Chapter 3.

4.2 Fracture surface of porous materials: Interpretation

In the previous section, the equation of the path of a crack propagating in a ideal elastic brittle disordered material has been derived from linear elastic fracture mechanics. Within the hypothesis of quasi-static crack propagation, the fracture surface is predicted to display anisotropic Family−Vicsek self-affine properties characterized by the scaling exponents $\zeta = 0.39$ and $\beta = 0.50$ along the crack front and the crack growth directions respectively. This result is consistent with the experimental measurements made on glass ceramics which is very close to an "ideal" elastic brittle material at scales larger than its bead diameter.

In this section, we go beyond the comparison between the experimental exponents and those predicted by the model. We will show that this model reproduces *quantitatively* many other statistical properties of experimental fracture surfaces. This section has two purposes: (i) To validate this model for describing crack propagation in brittle materials. In particular, many hypothesis of the theoretical analysis of brittle crack propagation will be directly confronted to the experimental fracture surfaces through appropriate statistical analysis of their roughness; (ii) To discuss the physical origin of the properties of crack roughness.

We will show that analyzing the roughness of crack surfaces through the proposed theoretical model can provide information on the broken material. Before this study, we return to the main hypothesis of this model of brittle cracks.

[14] Previous models discussed in Refs. [40] and [41] and based on the same theoretical framework predicted logarithmic correlations for the height fluctuation of fracture surfaces. The main difference between these models and the present analysis is the properties of the disorder: We have considered a more general case where the disorder of the material is three dimensional. Especially, the h-dependence of the mechanical properties of the material are not neglected as in Refs. [40] and [41]. This is crucial because in the latter case, the disorder would play the role of an effective temperature. Therefore, the crack surface morphology would be given by the line fluctuations at thermal equilibrium.

Effect of the crack growth velocity : One of the basic assumptions of the model proposed in Section 4.1 is the quasi-static propagation of the crack within the material, *i.e.* $v_{\text{crack}} \ll v_{\text{sound}}$. If the crack growth velocity v_{crack} is a non negligible fraction of the sound speed v_{sound}, inertial effects occur and another approach is required [85] (see for example [41] for the theoretical analysis of the implication on fracture surface roughness). In table 4.1, the crack growth velocities and the sound velocity are listed as a function of their porosity for the samples used in the present study. They have been measured using the experimental technique described in Annex A.

	$\phi = 3$ %	$\phi = 7$ %	$\phi = 15$ %	$\phi = 25$ %	$\phi = 26$ %
	Dyn.	Q.S.	Q.S.	Dyn.	Q.S.
v_{crack}	$\simeq 1$ m s^{-1}	40 mm s^{-1}	50 μm s^{-1}	$\simeq 1$ m s^{-1}	2 mm s^{-1}
v_{sound}	3.35 km s^{-1}	3.31 km s^{-1}	3.23 km s^{-1}	3.11 km s^{-1}	3.11 km s^{-1}

Table 4.1: Crack growth velocity v_{crack} and velocity of the sound v_{sound} for glass ceramics samples with various porosities ϕ and the same mean glass bead diameter $d = 116$ μm broken either in the Brazilian test geometry (*Dyn.*) or in the TDCB geometry (*Q.S.*). The hypothesis of quasi-static crack propagation ($v_{\text{crack}} \ll v_{\text{sound}}$) is always valid.

Sound velocity in the glass ceramics decreases slightly with the porosity but remains on the order of 3 km s^{-1}, three orders of magnitude larger than the crack growth velocity: This justifies the quasi-static approximation used to analyze the crack propagation in the theoretical investigation of the fracture surface morphology.

It must also be emphasized that a broad range of crack growth velocities has been investigated. As underlined in Chapter 3, this parameter apparently did not influence the scaling properties of the fracture surfaces for the various samples of glass ceramics investigated. This observation questions previous theoretical analysis [36] that described the crack front propagating in a disordered material as a moving line close to its depinning transition. In that case, one expects to observe two different self-affine regimes on the fracture surface: At small (resp. large) length scales, the scaling exponent correspond to an effective quenched noise (resp. thermal noise). The crossover length scale between these two regimes is expected to decrease with the crack growth velocity. This effect is not observed although the velocity investigated varies over more than five decades.

Moreover, the roughness amplitude depends very weakly on the velocity. Plotted on the same graph (see Fig. 3.11) as a function of the porosity, these amplitudes lie on the same linear curve although these measurements correspond to different crack growth velocities. This is in perfect agreement with one of the major prediction of the model presented in Section 4.1: The trajectory and velocity of the crack front are fully decoupled. The parameters involved in the path equation (Eq. (4.12)) -

some properties of the disorder in the material and its Poisson's ratio - depend on the material but not on crack growth velocity. This equation holds only in the quasi-static limit: As soon as the crack growth velocity approaches the velocity of sound, the dynamics of the crack front will influence its trajectory, leading for example to the patterns observed on mist and hackle zones on glass fracture surfaces.

Time symmetry of fracture surfaces : The morphology of the fracture surfaces has been observed to be independent of the crack growth velocity. This is in agreement with the theoretical argument showing the decoupling between the dynamic (or in-plane perturbations) and the trajectory (out-of-plane perturbations) of the crack. After discussion with J. P. Bouchaud from Service de Physique de l'Etat Condensé (CEA, Saclay), we decided to go deeper into this analysis and to tackle the following related problem: Because of clear geometrical reasons, the in-plane motion of the crack is oriented along the x-axis toward the positive value of x (see Fig. 4.1). Is there any signature of this directionality on the out-of-plane perturbations of the crack? In other words, is it possible to distinguish between backward and forward of crack propagation from the analysis of a fracture surface?

The issue of the determination of the orientation of the crack propagation from the fracture surface morphology has been already addressed in Section 2.3: It is possible to take advantage of the anisotropic scaling properties of the fracture surface to know after complete rupture the propagation orientation of the crack that led to the failure (see the patent in [62]). To test the possible presence of a signature of the direction of the crack propagation on the fracture surface, we will use statistical tools developed by Pomeau [86]: Instead of using the classical time two points correlation function $< h(t)\, h(t+\Delta t) - h(t) h(t-\Delta t) >_t$, we will compute a four points correlation function defined as

$$\psi(\Delta t) =< h(t)\, h(t+2\Delta t) - h(t+\Delta t)\, h(t+3\Delta t) >_t \qquad (4.17)$$

which is *a priori* not invariant under the transformation $\Delta t \to -\Delta t$ and thus sensitive to the propagation direction. In the following, the correlation function ψ will not be computed on $h(x=t,z)$ where x and z are the propagation and crack front direction respectively, but on its derivative $\frac{\partial h(x=t,z)}{\partial t}$.[15] The correlation function ψ is calculated for various values of z and then averaged over these z values.

To illustrate the properties of this correlation function, one can compute it on signals for which we know *a priori* their properties of symmetry. Fig. 4.4 displays the correlation function as defined in Eq. (4.17) for a signal $h(t,z)$ solution of the Edwards-Wilkinson equation [87] with either thermal ($\circ$) or quenched disorder ($\diamond$)

[15] We compute the correlation function on the derivative in time - or in x - of the studied signal in order to have a stationary signal with a constant mean value. This justifies the use of an average over the time t as required in the definition of ψ given in Eq. (4.17). Indeed, for the signals that will be studied in the following, *i.e.* elastic line propagating in a random medium, $h(t,z)$ is increasing in average while its derivative $\frac{\partial h}{\partial t}$ keeps a constant mean value.

(see footnote 9). While the equation with thermal disorder is invariant under the transformation Δt to $-\Delta t$, the solution of the equation with quenched disorder is expected to be asymmetric in time (see footnote 16). The signature of this asymmetry is obvious on its correlation function represented in Fig. 4.4.

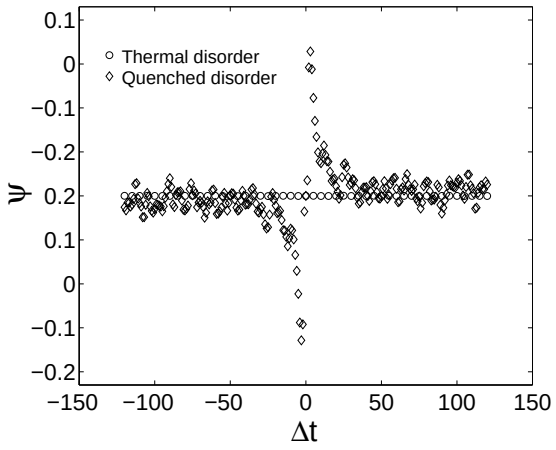


Figure 4.4: Correlation function as defined in Eq. (4.17) computed on simulated signals $\frac{h_z(t)}{\partial t}$ where $h_z(t)$ is solution of the Edwards-Wilkinson equation with thermal ($\circ$) and quenched disorder ($\diamond$). The equation of motion of the line is invariant under the transformation Δt to $-\Delta t$ only in the first case. The signature of these properties is obvious on the variation of correlation function ψ.

We use now this statistical tool to reveal possible signature of the propagation sense of the crack front on the roughness of fracture surfaces of porous materials. Fig. 4.5 displays the variations of this correlation function computed on the experimental height map $h(x, z)$ of the fracture surface of glass ceramics with porosities $\phi = 26$ % (a) and $\phi = 7$ % (b). In both cases, the mean bead diameter that corresponds also to the pixel size of the height map of the surface is $\simeq 100$ μm. We do not observe any significant signature of a time asymmetry as found on simulated signals in Fig. 4.4. Moreover, the slight deviations of ψ to the zero value were found to be uncorrelated with the physical direction of propagation measured during the fracture test. They are interpreted as statistical fluctuations.

This result agrees with the structure of the equation of trajectory proposed in Section 4.1. Indeed, the latter is invariant by the transformation $x \to -x$.[16] Finally,

[16]To realize it, let's come back at first on the Edwards-Wilkinson equations. With a thermal disorder, one can use the variable change $h = \hat{h} + F\,t$ so that the equation $\frac{\partial h}{\partial t} = \frac{\partial^2 h}{\partial z^2} + \eta(z,t) + F$ becomes $\frac{\partial \hat{h}}{\partial t} = \frac{\partial^2 \hat{h}}{\partial z^2} + \eta(z,t)$ which is invariant by the transformation t to $-t$. This change of variable in the case of the Edwards-Wilkinson equation with a quenched disorder $\eta(h,z)$ leads to a noise $\eta(\hat{h} + F\,t, z)$ which is not symmetric in time. The constant term F_0 in the equation of trajectory of the crack front (Eq. (4.13)) is so small that it can be neglected. Thus, the variable change

let us note that at scales smaller than the grain size where the surface is not self-affine, a signature of the propagation sense can be observed as shown in the insert of Fig. 4.5 b. It displays the variations of the correlation function computed on the height map of the same fracture surface that in the main panel, but with a better lateral resolution (pixel size of 20 μm). The curves are clearly asymmetric in the range $-100\ \mu\text{m} < \Delta x < 100\ \mu\text{m}$ similar to those observed in Fig. 4.4 for simulated signals with time-asymmetry properties.

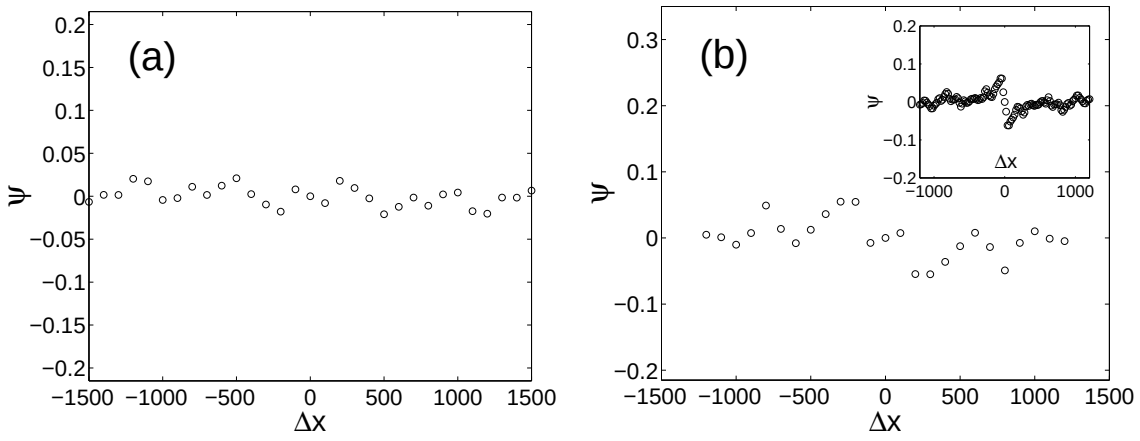


Figure 4.5: Correlation function ψ as defined in Eq. (4.17) computed on experimental signals $\frac{\partial h}{\partial x}$ and averaged over various values z where $h(x, z)$ is the fracture surface of glass ceramics with porosities $\phi = 26$ % (a) and $\phi = 7$ % (b). The x-axis corresponds to the direction of propagation. In the both cases, we do not observe any significant signature of a time asymmetry as found on simulated signals in Fig. 4.4. The analysis performed on a fracture surface with a smaller resolution (pixel size of 20 μm in insert instead of 100 μm in the main graph) suggests that a sense signature could be found on fracture surface, but for length scales that are not in the self-affine domain ($100\ \mu\text{m} < \Delta x$).

Three concluding remarks result from this statistical analysis of the fracture surfaces:

(a) Their roughness, *i.e.* the out-of-plane perturbations of the crack front, is found to be symmetric with respect to the direction of propagation. In contrast, the in-plane perturbations of the crack front are not symmetric by the transformation $x \to -x$. This confirms the decoupling – at least for small perturbations – between these two problems as predicted by the Linear Elastic Fracture Mechanics: The dynamics of the crack and its trajectory are independent.

(b) Fracture surfaces are symmetric by the transformation $x \to -x$. Therefore, the corresponding path equation of the crack front must be invariant by the

$h = \hat{h} + F\,t$ is not required and the equation is symmetric with respect to x.

transformation $x \to -x$. To derive this equation in Section 4.1, we compared the various contributions to the mode II stress intensity factor. It was shown that the effect of the fracture surface morphology – the "memory" term in Eq. (4.10) – on the path chosen by the crack is negligible. Contrary to the other terms involved in the path equation, this one is not symmetric when x is changing to $-x$. We confirm by the present analysis that the "memory" term is negligible.

(c) The roughness of the fracture surface cannot reveal all the history of the failure of a material. In particular, if the orientation of the crack propagation is possible through a statistical analysis of fracture surfaces [62], the determination of its direction is impossible, at least on length scales for which the fracture surface is self-affine. This result holds for fracture surfaces of porous materials that exhibit a low roughness exponent $\zeta \simeq 0.4$ but also for the broader range of materials studied in chapter 2 with $\zeta = 0.75$.[17] However, a determination of the crack propagation direction is possible when the path equation of the crack front does not hold, *i.e.* at scales smaller than typical disorder length scale in the material beyond the self-affine domain of crack surfaces.[18]

Inverse method on fracture surfaces : Here, we will compare quantitatively the model of brittle crack and the experimental fracture surfaces. After discussion with J. P. Bouchaud, we decided to follow this procedure: From the experimental fracture surfaces, we determine the coefficients of the Eq. (4.13) that describes its roughness. The values obtained for the coefficients are then compared to *a priori* expectations. This methodology is shown to be useful both for measuring the Poisson's ratio of a material as well as for quantifying some properties of its mechanical disorder. Let us note however that most results presented here are preliminary and that works to improve the method of coefficient determination described here are currently in progress.

Measure of the Poisson's ratio from the roughness of fracture surfaces : Here, we will give a method to determine the Poisson's ratio ν of a brittle material by measuring the coefficient of the elastic restoring force $A(\nu) = \frac{1}{\pi}\frac{2-3\nu}{2-\nu}$ involved in the path equation of the crack front. This coefficient is extracted from the experimental fracture surfaces through a method inspired by the work of Lam and Sanders [88]. They estimated the coefficients of Langevin equations $\frac{\partial h}{\partial t} = A.H(z,\{h\}) + \eta(z,t)$ from profiles $h(z,t)$ solution of these equations. We will use this inverse method in

[17] The time-symmetry of these surfaces is not shown here. This point will be discussed in the Section 4.4 devoted to these kinds of surfaces.

[18] One mentions also that once the field of local orientation of propagation on a fracture surface is determined through the method proposed in Ref. [62], the propagation sense can be deduced from the geometry of this field, the crack propagating from zone of high divergence to low divergence (see Ref. [62] for details).

a different context because the noise involved in Eq. (4.13) depends on the space variables x, h and z and not on the time t. The method is the following: At any time t and any position z (resp. any point on the fracture surface (x,z)), one can estimate both $H(z,\{h\})$ and $\frac{\partial h}{\partial t}$ (resp. $\frac{\partial h}{\partial x}$). According to the associated equation, the mean value of these quantities are proportional on providing that $\langle \eta(z,t) \rangle_{z,t} = 0$ (resp. $\langle \eta(z,h,x) \rangle_{z,h,x} = 0$), irrespective of the value of $\frac{\partial h}{\partial t}$ (resp. $\frac{\partial h}{\partial x}$). This assumption is clear for a thermal noise but could be questionable for a quenched noise for which the noise value at a point of the line can be strongly correlated with the local line geometry at this point. The assumption that this effect can be neglected is made *a posteriori* by comparing the results of the method with expected values. The coefficient of proportionality between $\frac{\partial h}{\partial x}$ and $H(z,\{h\}) = \int \frac{h(x,z')-h(x,z)}{(z'-z)^2} dz'$ gives an estimate of the coefficient A in front of the elastic interaction term $H(z,\{h\})$.[19] Fig. 4.6 shows

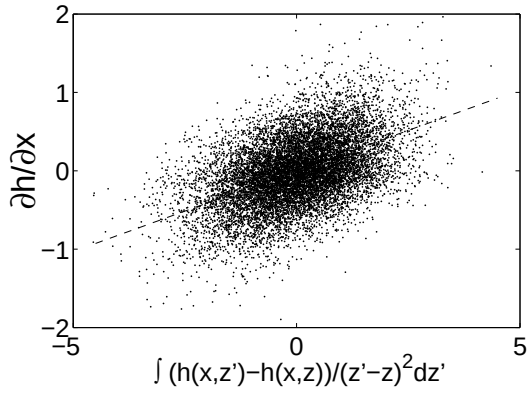


Figure 4.6: Variation of the angle $\frac{\partial h}{\partial x}$ with respect to the elastic restoring force $\int \frac{h(x,z')-h(x,z)}{(z'-z)^2} dz'$. These quantities are estimated on all the points of a fracture surface of glass ceramics with $\phi = 26\%$ for $\delta z = \delta x = 100$ μm. Even though the drawn quantities seems very slightly correlated - they are expected to be proportional (see Eq. 4.13) within the noise η which explained the important scattering of the data - , we make a linear fit of the points. It leads to $\frac{\partial h}{\partial x} = A \int \frac{h(x,z')-h(x,z)}{(z'-z)^2} dz'$ (dashed line) with $A \simeq 0.2$.

the variation of $\frac{\partial h}{\partial x}$ with respect to $\int \frac{h(x,z')-h(x,z)}{(z'-z)^2} dz'$ for a fracture surface of glass ceramics with a porosity $\phi = 26\%$. These two quantities are estimated in every point (z_i,x_i) of an experimental fracture surface made of N × N points representing a field of 100 N × 100 N μm^2 with $N \simeq 300$ by the relations $\frac{\partial h}{\partial x} = (h(x_{i+1},z_i) - h(x_i,z_i))/\delta x$ with $\delta x = 100$ μm and $\int \frac{h(x,z')-h(x,z)}{(z'-z)^2} dz' = \sum_{j=1}^{j=N} \frac{h(x_i,z_j)-h(x_i,z_i)}{(z_j-z_i)^2}$. Even though the drawn

[19] Note that the constant term F_0 of Eq. (4.13) cannot be measured through this method because the mean plane of the fracture surface is systematically subtracted to the height map.

quantities seems very slightly correlated - they are expected to be proportional (see Eq. 4.13) within the noise η which explained the important scattering of the data - , we make a linear fit of the points. It leads to $\frac{\partial h}{\partial x} = A \int \frac{h(x,z')-h(x,z)}{(z'-z)^2} dz'$ (dashed line) with $A \simeq 0.2$.

To test the robustness of the method, we apply the same procedure after having coarse grained the profiles over a length δz.[20] The coefficient A is expected to be independent of the coarse graining length scale δz, provided that the associated equation is correct [88, 89]. The value obtained for the coefficient A is plotted in Fig. 4.7 as a function of δz for four glass ceramics samples with different porosities. The coefficient A depends very slightly on the coarse graining length scale as long as this one lies within the self-affine domain 100 μm $< \delta z <$ 1 mm. This is a strong argument in favour of the proposed equation.

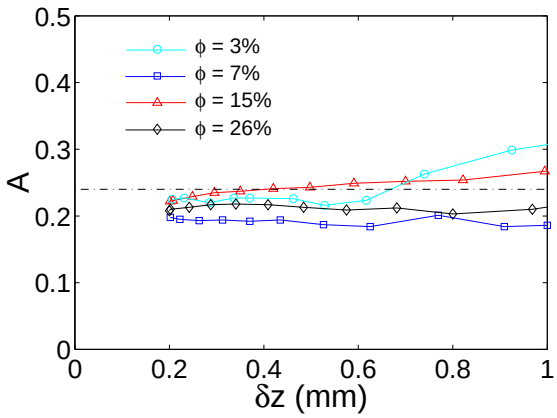


Figure 4.7: Estimation of the coefficient A of Eq. (4.13) from the experimental fracture surfaces of three glass ceramics. Their value do not depend on the length scale of the coarse graining of the profiles over their self-affine domain 100 μm $< \delta z <$ 1 mm as expected if Eq. (4.13) describes the fracture surface morphology. The obtained value $A(\nu) = \frac{1}{\pi}\frac{2-3\nu}{2-\nu} \simeq 0.22$ depends very slightly on the porosity. This value is quite comparable with the value $A \simeq 0.24$ (plotted in dashed line) obtained using the mean value of the Poisson's ratios $\nu = 0.21$ measured for the glass ceramics samples for glass ceramics (see Tab. A.1).

On the other hand, we observe that the coefficient A depends very slightly on the sample porosity. Thus, one gets $A(\nu) = \frac{1}{\pi}\frac{2-3\nu}{2-\nu} \simeq 0.22$ independently of porosity. To test the relevance of this value, we measure the Poisson's ratio in our samples. The propagation velocity of compressive and shear waves are measured and we obtain a value $\nu \simeq 0.21$ irrespective of the glass ceramics porosity (see Tab. A.1). The corresponding value for the coefficient A is therefore $A = \frac{1}{\pi}\frac{2-3\nu}{2-\nu} \simeq 0.24$. The expected

[20]The coarse graining of the profiles is obtained by truncating their Fourier components with wavelengths smaller than δz. See Ref. [88, 89] for the details of the procedure.

value for A is plotted in Fig. 4.7 (dashed line) to enable a comparison with the results of the inverse method: The value of the coefficient A obtained from a direct measurement of the Poison's ratio and the value obtained from the analysis of the fracture surfaces are very close (within less than 10 %). This agreement confirms experimentally that the non-local elastic interaction term in Eq. (4.13) describes the elastic force of the crack front in glass ceramics. This also confirms that the other terms in the development of K_{II} (see Eq. 4.10) can be neglected in first approximation.

Properties of the disorder : We have estimated the coefficient of the elastic restoring force and therefore the Poisson's ratio of glass ceramics through the statistical analysis of the crack roughness. The value is found in agreement with those measured directly for glass ceramics samples. Now, we can go further in the inversion process and analyze the properties of the disorder term $\eta(x, h, z)$ in the equation of crack propagation. This method should give interesting information on the mechanical disorder of the material. These properties are estimated here for glass ceramics samples with various porosities.

Eq. (4.13) leads to the relation

$$\eta(x, h, z) = \frac{\partial h}{\partial x} - A \int \frac{h(x, z') - h(x, z)}{(z' - z)^2} dz' \tag{4.18}$$

where the coefficient A is taken equal to the value measured previously for each porosity. It should be emphasized that the noise $\eta(x, y = h(x, z), z)$ obtained by this analysis corresponds to the one encountered by the crack front during its motion, and can be biased compared to the one describing the structural disorder of the glass ceramics.[21] From Eq. (4.18), it is possible to draw a map of $\eta(x, z)$ by measuring at each point of the fracture surface, the angle $\frac{\partial h}{\partial x}$ and the elastic restoring force.[22] Fig. 4.8 displays a 3D representation of a typical disorder $\eta(x, z)$ obtained on the surface of a fractured glass ceramic ($\phi = 26$ %).

To study quantitatively its properties, its spatial correlation functions $C(\Delta x) = \frac{\langle \eta(x+\Delta x,z).\eta(x,z)\rangle_{x,z}}{\langle \eta(x,z)^2\rangle_{x,z}}$ and $C(\Delta z) = \frac{\langle \eta(x,z+\Delta z).\eta(x,z)\rangle_{x,z}}{\langle \eta(x,z)^2\rangle_{x,z}}$ are computed along the x and z-axis respectively. The curves corresponding to the same sample ($\phi = 26\%$) are shown on Fig. 4.8. This analysis gives qualitatively similar results for other porosities. The correlation function along the crack propagation direction becomes uncorrelated after a distance $\Delta r \simeq 100$ μm. This is in rather good agreement with the length scale of mechanical heterogeneity expected for a porous material characterized by its grain size $d \simeq 116$ μm. On the other hand, the function $\eta(x, h(x, z), z)$ exhibits long-range correlation along the crack front direction. This result is clearly incompatible with the isotropic properties of the sample. However, as mentioned in footnote 22,

[21] See for example Ref. [90] for a comparison between the disorder of the material and the effective noise encountered by the moving crack front in the slightly different context of interfacial fracture.

[22] In fact, we can measure $\eta(x, h(x, z), z)$ where h is imposed by the position of the crack front. In other words, we do not measure the disorder of the material in a given plane (x,z) but the disorder on the rough surface defined by the crack front trajectory.

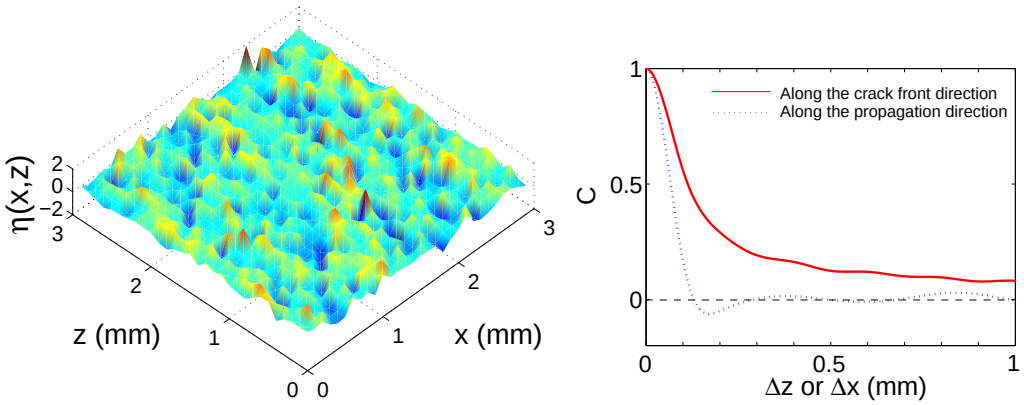


Figure 4.8: (left): 3D representation of the disorder $\eta(x, z)$ on a fracture surface of a glass ceramics with $\phi = 26$ % obtained by the inverse method described in the text using Eq. (4.18). (right): The solid and dotted lines are the spatial correlation functions computed along the z-axis and x-axis respectively.

the measured disorder corresponds to that encountered by the crack front during its propagation. It can have properties differing from those of the material. Such a structure would have been certainly impossible if the disorder used in the path equation of the crack front (Eq. (4.13)) had been annealed and not quenched. Indeed, in a recent work [91], Bolech and Rosso have considered the problem of an elastic line of position $x = h(z)$ in a random quenched potential $U(z, x)$ at the depinning threshold ($F = F_c$). They showed that the noise $\eta(x = h(z), z)$ along the line is strongly correlated, characterized by a spatial correlation function with a power-law decreasing tail. This was interpreted as a signature of the critical transition of pinning/depinning. This suggests that the measurement of noise correlation along the crack front is also reminiscent of its subcritical motion.

After studying the spatial distribution of the disorder measured on the glass ceramics, let us now focus on its magnitude. Fig. 4.9 displays the distribution of η measured on two fracture surfaces corresponding to two porosities. Each curve is well fitted by a Gaussian distribution although they display different second order moments σ that characterize here the amplitude of the disorder. In the inset of Fig. 4.9, this standard deviation σ is plotted as a function of the porosity of the broken sample. The latter is found to be roughly proportional to the porosity.

We recover the simple picture that the more porous the glass ceramics is, the more disordered it appears from a mechanical point of view - the limiting case being the homogeneous material corresponding to $\phi = 0$. We suggest here a simple quantitative explanation of this variation. At first, one recalls the definition $\eta = 2\frac{K_{II}^{\rm dis}}{\langle K_{Ic}\rangle}$ of the disorder given in Section 4.1. Therefore, the standard deviation σ of η is given by $\frac{\delta K_{II}^{\rm dis}}{\langle K_{Ic}\rangle}$ where $\delta K_{II}^{\rm dis}$ is the standard deviation of the toughness $K_{II}^{\rm dis}$. Let us assess first the

mean toughness $\langle K_{Ic} \rangle$ of the glass ceramics. Using the Eq. (A.3) and (A.7) giving the variation of their Young's modulus $E(\phi)$ and their fracture energy $G_{Ic}(\phi)$, one gets the variation of their toughness $\langle K_{Ic} \rangle(\phi) = \sqrt{G(\phi)E(\phi)} = \frac{K_{Ic}^0}{\sqrt{1-c^{\frac{2}{3}}}} \sqrt{(1-2\phi)(1-\left(\frac{c}{1-\phi}\right))}$ where K_0 is the toughness of the glass and $c = 0.63$. Note that this expression has been validated experimentally (see the insert of Fig. A.3 in Annex A). To estimate $\delta K_{II}^{\text{dis}}$, one has to notice that the spatial fluctuations of any quantity Q in a porous material made of solid grains characterized by $Q = Q_0$ in the bulk and $Q = 0$ in the voids are given by $\delta Q = Q_0 \sqrt{\phi(1-\phi)}$.[23] Finally, one gets the following estimate of the standard deviation $\sigma \simeq \frac{2\delta K_{II}^{\text{dis}}}{<K_{Ic}>} = \frac{2K_{II}^0}{K_{Ic}^0} \sqrt{\frac{\phi(1-\phi)(1-c^{\frac{2}{3}})}{(1-2\phi)(1-\left(\frac{c}{1-phi}\right)^{2/3})}}$. The coefficient $\frac{2K_{II}^0}{K_{Ic}^0}$ is not so simple to estimate because even the meaning of the toughness in mode II is not so clear. We have simply taken this coefficient equal to 1/2 and plotted the expected variations of σ with respect to ϕ in solid line in the insert of Fig. 4.9. Experimental points and the theoretical curve are in correct agreement.

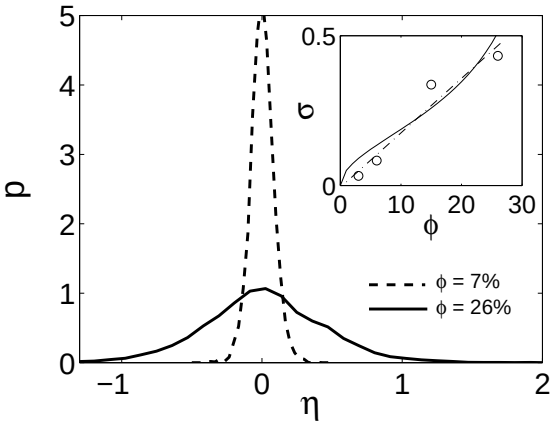


Figure 4.9: Distribution of the disorder η of two samples of glass ceramics with two different porosities measured from the fracture surfaces using the inverse method suggested in [88]. The disorder is Gaussian with standard deviation σ, which is plotted in inset with respect to the porosity ϕ and found to be roughly given by $\sigma \simeq 1.8\ \phi$ (dashed line). The theoretical estimation of the standard deviation of the disorder in glass ceramics proposed in this paragraph is also plotted in the inset (solid line).

Using the inverse method presented in [88], we have determined the coefficients

[23] One can calculate the standard deviation of the spatial distribution of the quantity Q of a two-phase material characterized by $Q = Q_0$ and $Q = 0$ in the solid and empty phase, respectively. One gets $(\delta Q)^2 = \langle Q^2 \rangle - \langle Q \rangle^2 = \frac{1}{V} \int_V Q(M)^2 dM - (\frac{1}{V} \int_V Q(M) dM)^2 = \frac{1}{V} \int_{V_{\text{solid}}} Q_0^2 dM + \frac{1}{V} \int_{V_{\text{voids}}} 0^2 dM - (\frac{1}{V}(V_{\text{solid}} \times Q_0 + V_{\text{voids}} \times 0))^2 = (1-\phi)Q_0^2 - (1-\phi)^2 Q_0^2$ that leads to $\delta Q = Q_0 \sqrt{\phi(1-\phi)}$.

of the Eq. (4.13) from the analysis of the morphology of the fracture surface. The obtained values are quite reasonable in view of the mechanical properties of the glass ceramics. This supports the relevance of the model of crack propagation in disordered media discussed in Section 4.1. The previous result suggests also that fracture surfaces could be a tool to measure the disorder properties of a material. Using the preceding method, it is possible to measure both the correlation length r_η of the disorder and its strength σ from a statistical analysis of the roughness of their crack surfaces. This method of characterization will be greatly improved when the link between material disorder and disorder encountered by the crack front will be theoretically made.

In the next part, we will focus on the amplitude of the crack surface roughness. This quantity is reminiscent of the properties of the material disorder, *i.e.* r_η and σ, studied previously. At first, the relation between this property of fracture surfaces and the material properties is established. Then, we will test it on the experimental case of glass ceramics.

Roughness amplitude : One of the most striking features of the experimental results reported in Chapter 3 is the robustness of the roughness exponents of the fracture surfaces with respect to the type of porous materials. On the other hand, the amplitude of the roughness – the proportionality coefficient in the power-law relation between the distance between two points of the fracture surface and their height difference – was shown to be sensitive to structural properties of the material such as the grain size d or the porosity ϕ. The analysis of various samples of glass ceramics led to

$$\Delta h(d)/d \simeq 1.7\,\phi \tag{4.19}$$

where $\Delta h(\Delta z)$ is the 1D correlation function computed along the direction of the crack front on the fracture surfaces (see Section 3.3 for details). This relation was shown to reproduce rather well the experimental results irrespective of the crack growth velocity. This point was then discussed in the first paragraph of Section 4.2 and shown to be in agreement with the suggested model of crack propagation in brittle materials. In the present paragraph, we use again this model: We will compare theoretically the relation between the structural properties of the disordered brittle material and the amplitude of the fracture surface roughness. This prediction will then be compared to the experimental results summarized by Eq. (4.19) obtained on the model disordered brittle material discussed in this chapter, the glass ceramics.

The morphology of the fracture surfaces has been shown to be well described by the motion of an elastic string creeping within a quenched disorder (see Eq. (4.12)). Its scaling properties along the crack front direction are given by the properties of this elastic string and characterized by $\zeta = 0.39$. The amplitude of the roughness along this direction is also given by the geometry of the string. We investigate here this geometry at the depinning threshold – driving force applied to the line is equal to the critical force ($F = F_c$) – and not in the creep regime ($F < F_c$) while assuming

that the roughness amplitude is comparable in both situations. In the first situation, the correlation function of the string is

$$\Delta h = k_0 r_\eta \left(\frac{\Delta z}{L_{\text{Larkin}}} \right)^\zeta \tag{4.20}$$

Here, k_0 is a constant of the order of unity, r_η is the correlation length of the disorder, ζ is the roughness exponent and L_{Larkin} is the Larkin length, *i.e.* the length scale at which the elastic restoring force is equal to the pinning force of the disorder. For the model of crack propagation with non-local elasticity, one gets $\zeta = 0.39$ and $L_{\text{Larkin}} = r_\eta \left(\frac{A}{\sigma}\right)^2$ where $A = \frac{1}{\pi}\frac{2-3\nu}{2-\nu}$ is the coefficient of the elastic restoring force. This leads to

$$\Delta h = k_0 r_\eta^{1-\zeta} \left(\frac{\sigma}{A} \right)^{2\zeta} \Delta z^\zeta \tag{4.21}$$

To obtain the constant k_0, we solve numerically (see the following paragraph for details) the equation giving the path of the crack (Eq. (4.13)) with all the coefficients – r_η, σ, and A – equal to unity. The approximation of a 2D quenched disorder $\eta(h, z)$ instead of the noise $\eta(x, z, h)$ is used. The solution is characterized by its height correlation function $\Delta h^*(\Delta z^*) = k_0(\Delta z^*)^\zeta$ with $k_0 = 0.35 \pm 0.01$. Using the following estimates derived both theoretically and experimentally (see previous paragraphs) $\sigma \simeq 1.8\,\phi$, $A = 0.22$ and $r_\eta \simeq d/2$ for a glass ceramics of porosity ϕ and a mean bead diameter d, one gets from Eq. (4.21) the expression of the roughness amplitude for these materials

$$\Delta h(d)/d = 1.18\,\phi^{2\zeta} \tag{4.22}$$

First at all, this confirms theoretically what was observed experimentally: $\Delta h(d)$ is proportional to d and the coefficient depends only on the porosity ϕ of the material. The variations of $\Delta(d)/d$ with ϕ are plotted in Fig. 4.10 and compared to the experimental measurements. The agreement between the two is rather good. Let us note that the model proposed here uses no adjustable parameters. The apparent linear variation of the amplitude with ϕ observed experimentally – compare Eq. (4.22) and Eq. (4.19)) – is rather close to the expected variation in $\phi^{2\zeta} \simeq \phi^{0.8}$. However, the amplitude is overestimated at low porosities. The possible decreasing trend of the correlation length r_η of the disorder with ϕ could be responsible for this slight discrepancy.

In this paragraph, we have shown that the amplitude of the roughness in the case of a brittle rupture is set by two microstructural parameters of the material: the "strength" σ of the disorder in the material and its spatial correlation length r_η. In the case of glass ceramics, we established the relation between these two parameters and the porosity ϕ and the bead diameter d which could be varied in a controlled manner. Therefore, it was possible to check experimentally the relation between the microstructure and the fracture surface morphology. It must be emphasized that this relation – Eq. (4.21) especially – applies to any material after a brittle

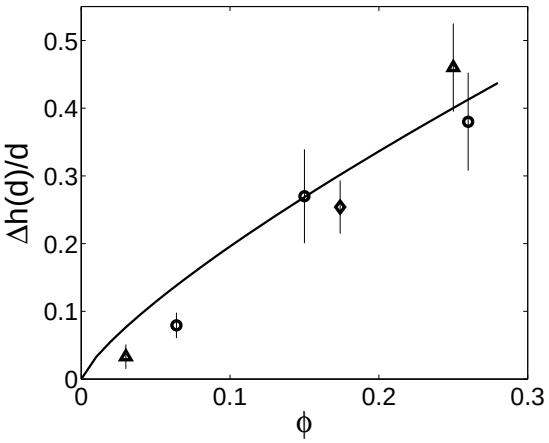


Figure 4.10: Variation of the amplitude of the roughness $\Delta h(d)/d$ of fracture surfaces of glass ceramics samples with respect to their porosity ϕ. The solid line is the theoretical prediction of the model proposed in this chapter. Note that this curve has been derived without any adjustable parameters.

fracture. Therefore, the roughness amplitude reflects the properties of the disorder in the material while the roughness exponent will be shown to be determined by the rupture mode of the material.

Height variation distribution : In this paragraph, we will interpret an important feature of fracture surfaces of porous materials using the model described in the present chapter: The distributions of height differences $P_{\Delta z}(\Delta h)$ between two points for various distances Δz collapses after normalization by Δz^ζ onto a Gaussian distribution (see Section 3.4 and 3.2). In other words

$$P(\Delta h) = 1/\Delta z^\zeta \; g(\Delta h/\Delta z^\zeta) \tag{4.23}$$

where g is a Gaussian distribution. In the model, the crack surface is given by an equation of motion of a line in a disordered medium which leads to a mono-affine geometry of the line [65] so that the collapse described in Eq. (4.23) with a unique exponent ζ is expected. More interestingly, one can wonder whether such a model can reproduce, in addition to the value of the roughness exponent and to the roughness amplitude, the shape of the distribution of the height variations. This is a crucial point because all the geometrical features of the surface would then be explained.[24] To answer this question, we shall solve numerically the equation of trajectory[25] proposed

[24]Statistically speaking, the geometry of a self-affine profile is entirely defined by the three following parameters: the self-affine exponent, the roughness amplitude and the distribution of height differences.

[25]The morphology of the fracture surface is set by the subcritical motion ($F < F_c$) of an elastic line in a random potential (see Eq. (4.12)). Here, we will solve numerically the same equation but

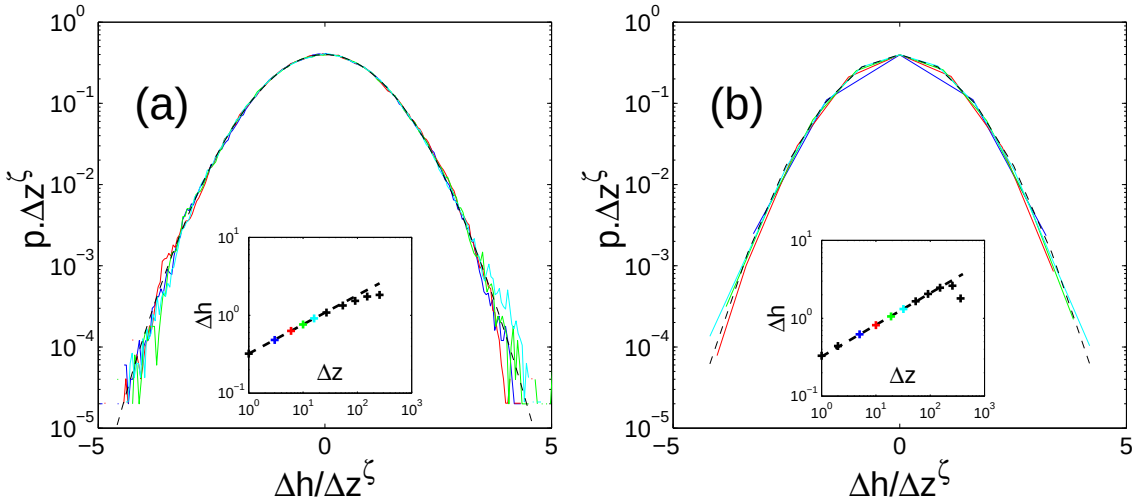


Figure 4.11: Normalized distribution of height variations of the elastic line on a simulated fracture surface obtained by (a) a direct resolution of the path equation of the crack front and (b) an extreme dynamics algorithm (see text for details) for various value of Δz. The two collapsing master curves obtained with $\zeta = 0.39$ are found to be Gaussian distributions $p(x) = 1/\sqrt{2\pi}e^{-x^2/2}$ represented in dashed line. The variation of the 1D correlation functions, *i.e.* the second order moment of the distribution, is shown in inset. The dashed lines are power-law fits characterized by their slope $\zeta = 0.39$. The coloring points correspond to values of Δz for which the distributions $P_{\Delta z}(\Delta h)$ have been plotted in the main panel.

in the model and then compute the distribution $P(\Delta h)$. Two types of simulation are used. The Eq. (4.12) is solved through a Runge−Kutta algorithm. The thermal noise term in this equation is removed and a constant driven force along the line is added so that the motion of the line above the critical threshold ($F > F_c$) is simulated (see note 25). The second simulation is a discrete model using an extreme dynamics: At any time step, one point of the line moves forward by a unit length, the position of the moving point being given by the weakest link on the line, defined as the point where the difference between the elastic restoring force $F_{\rm el}$ and the pinning force η is maximum. This process leads to line morphologies corresponding to a motion at the critical threshold ($F = F_c$) [92].

The insets of Fig. 4.11 display the height−height correlation function computed on the profiles (along the z-direction of the simulated) fracture surfaces) generated by (a) the direct resolution of the path equation and (b) the extreme dynamics algorithm. In both cases, the measured roughness exponent is found to be $\zeta = 0.39 \pm 0.01$ in agreement with the literature [83, 82, 93]. The normalized distributions $1/\Delta z^\zeta\, P(\Delta h/\Delta z^\zeta)$

at the critical threshold ($F = F_c$) and above it ($F > F_c$), the height variation distribution of the rough line being expected to be nearly the same in all these cases [80].

collapse onto a single master curve as expected for a mono-affine geometry (Eq. (4.23)). The main curve is a Gaussian distribution irrespective of the used numeric algorithm. Moreover, both Gaussian and constant distributions of disorder were used with no effects on the height variation distribution. This supports the robustness of this result.[26] This is in agreement with the observation of Gaussian distributed variations of height observed on the experimental fracture surfaces of porous materials.

Concluding remarks : The model of crack propagation in a brittle materials proposed in Section 4.1 explains the three important features of the experimental fracture surfaces of porous materials: the value of the scaling exponents, the amplitude of the roughness and the shape of the Gaussian distribution of height variation. In other words, one can reproduce *quantitatively* all the statistical properties of fracture surfaces. Thus, one can conclude that the proposed model is able to describe the fracture surfaces after brittle fracture in the case of glass ceramics. The natural next step is to enlarge the investigated experimental systems: We will focus now on other materials broken in a brittle manner for slow crack propagation. The roughness of their fracture surfaces will be studied. Their scaling properties will be then confronted to the predictions of the model.

4.3 Fracture surfaces of other brittle materials

The model of crack propagation discussed in Section 4.1 may explain the "universal" features of the morphology of fracture surfaces observed on a broad range of porous materials and described in Chapter 3. The main ingredients of this model are a low crack growth velocity, a brittle fracture as well as a mechanical disorder of the material so that the theoretical framework of the Linear Elastic Fracture Mechanics in the context of disordered materials may be used. After explaining *quantitatively* the crack morphology in the case of the glass ceramics chosen both for its simple microstructure and because its properties can be adjusted, it is now very tempting to study more complex disordered materials broken within the same hypothesis (quasi-static and brittle fracture). Especially, do their fracture surfaces exhibit similar properties? Can one explain them with the proposed model? In the present paragraph, we will focus on two examples of brittle failure. This part will present the questions that remain open about the study of fracture surfaces resulting from a brittle failure. The complete study of the problem is left for future work.

[26]This result must not be confused with the Gaussian geometry of elastic line driven in random media observed numerically by A. Rosso *et al.* [94]: They showed that the geometry of elastic lines at the depinning threshold is very well approximated by the one of a Gaussian signal. The latter is defined so that all their Fourier modes are independent and Gaussian distributed. This property induces necessarily the Gaussian distribution of height variation Δz. But the reciprocal is not true.

Silica glass at the micrometer scale : *Experiments :* Fracture surfaces of silica glass were investigated from the micrometer scale to the millimeter scale.[27] DCDC samples broken in a tensile mode in the stress corrosion regime are used. The experimental setup is described in detail in Section 2.1. The velocities investigated are smaller than 1 μm s^{-1}. A mechanical profilometer, with vertical and lateral resolutions of the order of 0.5 nm and 1 μm respectively, is used to get profiles perpendicular to the crack growth direction (z-axis). Surprisingly, at very large length scales compared to the nanometric structure of the glass, the fracture surface is observed to be rough as shown in Fig. 4.12. The 1D correlation function of the profiles is shown in insert of the same figure. Its power-law behavior suggests that fracture surfaces of glass in a domain of length scales around some tenths of millimeters are self-affine. The profiles perpendicular to the crack growth direction are characterized by a roughness exponent on the order of $\zeta \simeq 0.3$, slightly smaller than those observed for glass ceramics. Let us note that similar observations were reported on more complex glasses [95] at length scales between 100 nm and 10 μm.

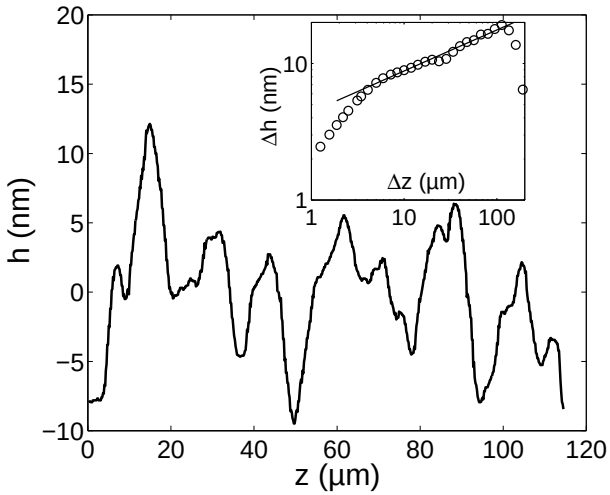


Figure 4.12: Profile extracted on a fracture surface of silica glass broken in the stress corrosion regime ($v_{\rm crack} < 10^{-6}$ m s^{-1}).

Interpretation: Since the scaling properties investigated here were observed at length scales *larger* than the process zone size of silica glass ($\ell_{\rm PZ} \simeq 100$ nm [14, 96]), it is natural to interpret them within the model of brittle failure developed in Section 4.1. The theoretical investigation of the fracture surfaces within the framework of Linear Elastic Fracture Mechanics leaded to the conclusion that, in the quasi static limit, brittle failure in disordered materials leads to self-affine fracture surfaces characterized

[27] The length scale of observation is crucial here. Fracture surface of silica glass has already been investigated in Chapter 2. At scales smaller than $\xi \simeq 100$ μm, it has been shown to be self-affine characterized by a roughness exponent $\zeta \simeq 0.75$. We focus here on larger length scales.

by a "small" roughness exponent ($\zeta < \zeta_{\rm dep} = 0.39$). Moreover, it was shown - according to the phase diagram presented in Fig. 4.3 - that three cases are possible: Logarithmic correlation of height or power-law correlations characterized either by $\zeta_{\rm eq} = 1/3$ or by $\zeta_{\rm dep} = 0.39$. The experimental measurement of a "small" roughness exponent $\zeta \simeq 0.3$ on fracture surfaces of silica glass in a domain of length scale much larger than the process zone size seems compatible with the predictions of the model. However, it is difficult to affirm whether these observations are reminiscent of the roughness exponent at equilibrium or at the depinning threshold and further experimental investigations would be required to decide.

Metallic alloy failure at low temperature : *Experiments :* In the previous paragraph, fracture surfaces of silica glass has been shown to exhibit scaling properties reminiscent of a brittle failure when observed at large length scales.[28] We will focus now on the failure of a metallic alloy, archetype of ductile materials. But we will study their fracture surfaces in a domain of length scales much larger than its process zone size, so that we could define at these scales an equivalent material the behavior of which would be perfectly elastic. We will see that at these scales, the geometry of fracture surfaces is reminiscent of a brittle mode of failure.

Stéphane Chapuliot and co-workers from the laboratory DEN/LISN at the CEA kindly provided us with compact tension specimen of 16MND5 steel broken at various temperature ranging from $T = 30°K$ to $T = 300°K$.[29] We will focus here only on the low temperature specimen. The complete study is currently performed by Claudia Guerra and coworkers in the "Fracture" Group. The height map (1024×1024 points corresponding to a field 5 mm $\times$ 5 mm^2) of its fracture surface obtained after scanning by a mechanical profilometer is represented in Fig. 4.13 a. The 1D height−height correlation functions computed perpendicularly and parallel to the crack growth direction on the surface is plotted in Fig. 4.13 b in semi-logarithmic scales. Surprisingly, the correlations of height do not follow a power-law behavior, but rather a logarithmic law in both directions

$$\Delta h(\Delta z) = A_z log(\Delta z/\ell_z) \quad \text{and} \quad \Delta h(\Delta x) = A_x log(\Delta x/\ell_x) \tag{4.24}$$

In that case, it is still possible to define a dynamic exponent as $z = \frac{A_z}{A_x}$.[30] Here, the fracture surface is isotropic so that $A_x \simeq A_z \simeq 19$ μm and $\ell_x = \ell_z \simeq 7.5$ μm. This leads to $z = 1 \pm 0.1$.

[28] compared to its process zone size; see Section 4.4 for a quantitative analysis of this effect.

[29] The experimental setup is similar to the one described in section 2.1 and used for aluminum alloy samples. In particular, the crack growth velocity is rapid, but not dynamic. See Ref. [97] for details.

[30] The 2D correlation function of the surface follows a pseudo Family−Vicsek scaling where all power-laws are changed by logarithms. In particular, the pseudo scaling function involved in Eq. (4.14) is $g(u) = log(u)$ with $u = \Delta z/\Delta x^{\frac{A_x}{A_z}}$ that defines the dynamic exponent $z = \frac{A_z}{A_x}$.

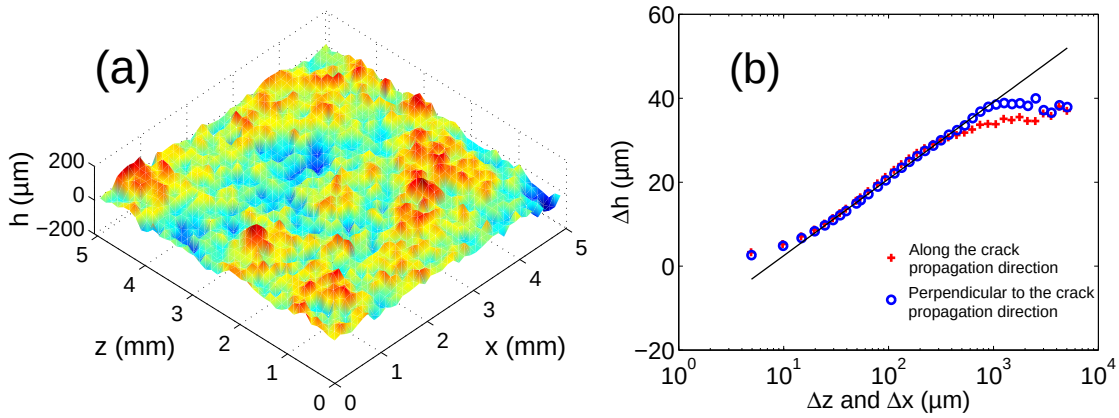


Figure 4.13: (a): Fracture surface of a metallic alloy broken at low temperature $T = 20°K$. (b): Its correlation function computed along the z and x-axis does not follow a power-law. The corresponding curves plotted in a semi-logarithmic scales suggest that the correlation of height are logarithmic.

Interpretation : At such a low temperature, metallic alloy does not break in a ductile manner. From the measurement of its toughness $K_{Ic} = 10$ MPa m$^{1/2}$ and its intrinsic strength $\sigma^* = 1.3$ GPa, one gets from Eq. (A.1) an estimate of the process zone size $\ell_{\rm PZ} \simeq 20$ μm in these materials at $T = 30°K$ [97]. In other words, at scales much larger than the micrometer scales, failure in these materials is brittle. Therefore, it is tempting to interpret the statistical properties of its fracture surface with the model proposed in Section 4.1. Within the framework of the Linear Elastic Fracture Mechanics, it was shown that for a given range of parameters (see the phase diagram in Fig. 4.3), the fracture surface morphology could be set by the geometry of a line at thermal equilibrium with long range elastic interactions. In other words, the fracture surface can be characterized by the scaling exponents $\zeta_{\rm th} = 0$ and $z_{\rm th} = 1$, *i.e.* by isotropic logarithmic correlations of height. Such a prediction for brittle fracture surfaces was also made in Refs. [40, 41]. These predictions are in apparent agreement with the experimental measurements made on fracture surface of brittle metallic alloy. However, the reasons for which height correlations are logarithmic and not characterized by $\zeta_{\rm dep}$ or $\zeta_{\rm eq}$ remains unclear. In other words, the position of the various brittle materials in the phase diagram presented in Fig. 4.3 is still an open question. Both experimental study of various brittle materials on a great range of length scales and theoretical study of Eq. (4.13) to improve our knowledge of the parameters that sets the limits between the various phases are required.

Concluding remarks : The experimental study of various kinds of fracture surfaces resulting from a brittle failure suggests that their scaling properties is characterized in a general manner by "low" roughness exponents, $\zeta_{\rm dep} = 0.39$, $\zeta_{\rm eq} = 1/3$

and $\zeta_{\rm th} = 0$. Theoretically, these three phases correspond to the three possible geometries predicted by the model of crack propagation in brittle materials, although the parameters that delimit each phase remain yet to be identified. On the other hand, the morphology of fracture surfaces studied in Chapter 2 and characterized by the "universal" roughness exponent $\zeta \simeq 0.75$ is clearly incompatible with the model of brittle failure proposed in section 4.1. The origin of this apparently abnormal[31] scaling property is discussed in the next section.

4.4 Fracture surfaces of ductile materials : Interpretation

The experimental investigation of various fracture surfaces have shown that their morphology satisfies a Family−Vicsek scaling, without exceptions. But the measurement of the exponents involved in this scaling suggests the existence of two classes for the morphology of fracture surfaces that are characterized by two different roughness exponents. We investigate here the underlying physical processes responsible for the scaling characterized by the roughness exponent $\zeta \simeq 0.75$.

Relevant length scales on fracture surfaces : At first, to identify the physical mechanisms leading to this roughness exponent, let us investigate the following scenario: Naively, one could imagine that some materials – silica glass, aluminum alloy, mortar, wood (see Chapter 2) – leads to one class of fracture surfaces while the other materials – sandstone, glass ceramics (see Chapter 3) – leads to fracture surfaces characterized by $\zeta \simeq 0.4$. The experiments on fracture surfaces of silica glass and metallic alloy over "unusual" domain of length scales, *i.e.* at length scales large compared to the typical length scale of non-linear processes involved in the failure of these materials, have cast doubts on this possibility because both scalings are found on same materials. Indeed, at small (resp. large) length scales, the fracture surface is characterized by a roughness exponent $\zeta \simeq 0.75$ (resp. $\zeta \leq 0.4$). This suggests that the roughness exponents characterise length scales rather than materials. Therefore, to understand the origin of the small scale regime, it is of interest to study the domain of length scales for which $\zeta \simeq 0.75$ is observed.

To investigate the self-affine domain of fracture surfaces with $\zeta \simeq 0.75$, we have focused on failure of silica glass.[32] For this material, the self-affine domain ranges at least from the nanometer scale – for experimental reasons, it is unfortunately

[31] The expression "abnormal" is used here because the normal case is considered to be the failure of a brittle material that leads to low roughness exponent. However, from an historical point of view, fracture surfaces with low roughness exponents could be considered as exceptions because they were observed after fracture surfaces with $\zeta \simeq 0.75$ [25, 26].

[32] This experimental work has involved many co-workers in the "Fracture" Group that are also the authors of the Ref. [98].

impossible to investigate their fracture surfaces at smaller length scales – up to an upper bound ξ_z (along z) of the order of one hundred of nanometers. The latter is defined in Fig. 4.14 a as the abscissa of the intersection between the power-law fit of the self-affine regime (with $\zeta \simeq 0.75$) and the plateau regime (horizontal line). This length is measured on fracture surfaces corresponding to various crack growth velocities v_{crack} (the experimental procedure to obtain a fracture surface which has clearly separated zones corresponding to different velocities is described in Section 2.1). The scaling exponents do not show any noticeable dependence on v_{crack}. On the other hand, the cutoff length ξ_z was observed to decrease slowly, as the logarithm of v_{crack} (Fig. 4.14 b). For the smallest value of v_{crack}, ranging from 10^{-12} to 10^{-9} m/s, we were able to observe in real-time, at the nanometer scale, the crack propagation during the specimen failure [34, 15]. At these scales, the crack was shown to grow through the growth and coalescence of nanoscale damage cavities [34, 15]. This cavitation process was shown to set the size of the process zone, *i.e.* the zone in the vicinity of the crack tip where linear elasticity stops being relevant [15]. The variation of the process zone size ℓ_{PZ} with respect to the crack velocity v_{crack} is presented in the inset of Fig. 4.14 b. First, ℓ_{PZ} is found to be larger, but of the same order of magnitude as ξ_z. Second, ℓ_{PZ}, like ξ_z, is observed to decrease as the logarithm of v. This leads us to the conjecture that the process zone size ℓ_{PZ} is the relevant length-scale that sets the crossover length ξ_z. At length scales smaller than ξ_z, the material cannot be identified with a coarse-grained equivalent linear elastic medium, which explains the failure of the model of brittle crack.

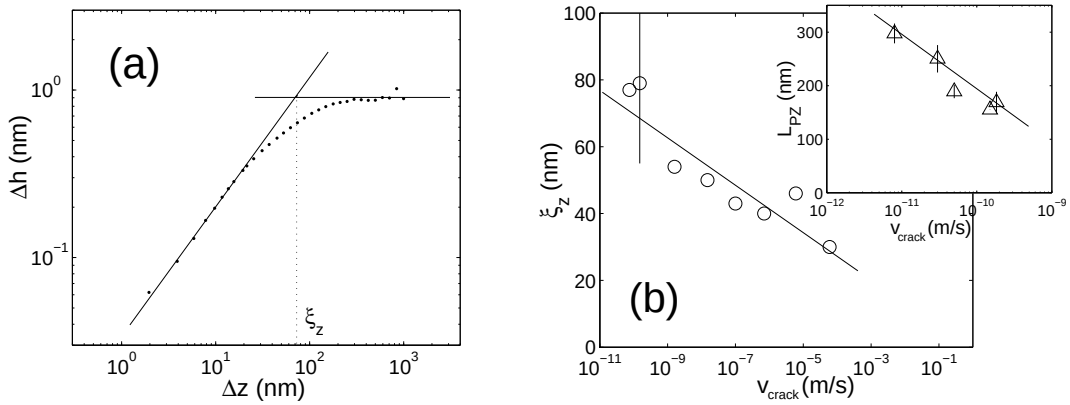


Figure 4.14: (a) Variation of the correlation function computed along the z-axis on a fracture surface of silica glass broken in the stress corrosion regime with $v_{\text{crack}} = 6.10^{-11}$ m s^{-1}. (b) Variation of the crossover length ξ_z (measured along z) as a function of the crack growth velocity v. The axes are semilogarithmic. The straight line corresponds to a fit $\xi \propto \log(v)$. Inset: Variation of the size of the process zone R_c (measured along x) as a function of the crack growth velocity v. The axes are semilogarithmic. The straight line correspond to a fit $R_c \propto \log(v)$.

Let us note that the upper bound ξ_x of the self affine domain with $\beta = 0.6$ observed along the x-axis of fracture surfaces is of the same order than ξ_z. Therefore, the 2D length scales domain with $\Delta x < \xi_x$ and $\Delta z < \xi_z$ where scaling regime of fracture surfaces of glass is characterized by the exponents $\{\zeta \simeq 0.75, \beta \simeq 0.6, z \simeq 1.2\}$, is observed at length scales where failure occurs through non-linear processes (such as damage or cavitation) that cannot be described through the LEFM framework.

To investigate the generality of this result, let us return to the other materials where such a scaling was observed. In Table 4.2, the upper cutoff length ξ_z that limits (along the z-axis) the scaling regime with the exponents $\{\zeta \simeq 0.75, \beta \simeq 0.6, z = \zeta/\beta \simeq 1.2\}$ as well as the expected process zone size $\ell_{\rm PZ}$ – either estimated using Eq. (A.1) or directly measured experimentally as for silica glass samples – are listed for each material. The width $L_{\rm sample}$ of the sample is also listed. The comparison of these three lengths suggests that two cases are possible: (i) $\ell_{\rm PZ} \ll L_{\rm sample}$: The cut-off length is smaller, but of the same order of magnitudes, than the process zone size ($\xi_z \simeq \frac{\ell_{\rm PZ}}{2}$). (ii) $\ell_{\rm PZ} > L_{\rm sample}$: The cut-off length is of the order of a tenth of the sample width ($\xi_z \simeq \frac{L_{\rm sample}}{10}$). The latter relation, that has also been observed for sandstone samples (see Fig. 3.15), has been reported for mortar [72] and wood [29] samples of various widths. In other words, when finite size effect due to finite geometry of the sample do not occur, *i.e.* all length scales are smaller compared to $L_{\rm sample}$, the process zone size $\ell_{\rm PZ}$ sets the upper bound ξ_z of the self-affine regime.

Material	ξ_z	$\ell_{\rm PZ}$	$L_{\rm sample}$
Silica glass[33]	80 nm $\pm$ 20 nm	150 nm $\pm$ 30 nm [98]	5 mm
Quasicrystal	2.1 nm $\pm$ 0.5 nm	$\simeq$ 4 nm [18]	10 mm
Aluminum alloy	80 μm $\pm$ 10 μm	$\simeq$ 200 μm	15 mm
Mortar	2.5 mm $\pm$ 0.5 mm	$>$ 20 mm	20 mm
Wood	1.0 mm $\pm$ 0.1 mm	$>$ 11 mm	11 mm

Table 4.2: Cut-off length ξ_z (measured along z) of the self-affine domain for various materials. This length can be compared with both the sample width $L_{\rm sample}$ and the estimated value of the process zone size of the materials. Note that when $\ell_{\rm PZ} \ll L_{\rm sample}$, the cut-off length is of the same order than the process zone size .

This result leads to the following picture: Below the process zone size, *i.e.* at length scales where the material cannot be identified with a coarse-grained equivalent linear elastic medium, the model of brittle crack presented in Section 4.1 fails and fracture surface exhibits universal features (see Chapter 2) characterized by the exponents $\{\zeta = 0.75, \beta = 0.6, z = 1.2\}$. The identification of the underlying physical process responsible for such as scaling raises many questions: How can non-linear processes proper to each material let universal signature on the fracture surfaces?

A possible model of crack propagation in quasi-brittle and ductile materials : We propose here a simple model that is able to reproduce the scaling properties of fracture surfaces at the scale of the non-linear processes of rupture. It gives the important physical mechanisms at the origin of its scaling properties. But the heart of this problem, *i.e.* the complex interactions between damage, crack front and microstructure, will not be analyzed quantitatively here and are let for future works.

The theoretical investigation of fracture surfaces characterized by $\zeta \simeq 0.75$ would require to integrate the effects of damage to the model of crack propagation in an ideal elastic brittle material of Section 4.1. This would require understanding the complex interactions between a crack front and a microcrack/cavity. We will avoid this difficulty by using here another approach. We will analyze the theoretical implications of the very basic properties of these fracture surfaces, *i.e.* their symmetry and their anisotropic scaling. The more general equation that satisfies them will then be derived.

Ductile crack surfaces display a Family−Vicsek scaling (see Section 2.4). Such a scaling results from the competition between the disorder of the material and the elasticity of the front – which displays long range elastic interactions. These two ingredients will lead to the two competing terms $F_{\rm el}$ and $F_{\rm dis}$ in the investigated equation for ductile fracture surfaces. Family−Vicsek scaling of fracture surfaces is the signature of the propagation of a line. Fracture surfaces resulting from a damage coalescence process as proposed in [46] would not have such a property. This suggests that an effective crack front can still be defined at all length scales, even if damage processes can be very spread.[34] These microcracks/cavities will be simply considered as external perturbations. In our very simplistic model, they will contribute to enhance the disorder of the material. Within this hypothesis, the term for the disorder $F_{\rm dis} = \eta(x, h, z)$ will be similar to the one involved in our model of brittle failure.

On the other hand, the microcracks/cavities will affect the crack front trajectory. This effect will be considered in average so that it is the same for all points of the front.[35] This effect is modeled by changing the elastic term in the path equation of the crack. In other words, we take in consideration the effect of the damage by defining an effective crack front with new properties – especially a new elastic energy – that are still to define.

Using symmetry arguments, let us now derive the properties of the elastic term. As for brittle fracture surfaces, these surfaces are invariant by the transformation $x \to -x$. The methodology described in Section 4.2 has been applied on fracture surfaces of silica glass and aluminum alloy. No signature of the propagation direction,

[34] At least in the experimental systems investigated in this work. For some fracture test geometries, *e.g.* without notch, the definition of this effective crack front may be impossible.

[35] The very simple model proposed here is a mean field like theory in the sense that the interaction of each microcrack/cavity with the front is equivalent to one effect applying uniformly on the front.

i.e. crack growth along $+x$ or along $-x$, can be observed. This suggests also that the problem of crack propagation in ductile materials can be divided into two problems: (i) The dynamics of the crack that will be given by a motion equation applying on the in-plane perturbations of the effective crack front - this equation is not time-symmetric; (ii) The path of this front leading to the geometry of the fracture surface that is given by a time-symmetric equation applying on its out-of-plane perturbations. This simplifies greatly the investigated equation: It depends on the sole out-of-plane perturbation h of the effective crack front. Moreover, terms such as the "memory" term involved in Eq. (4.10) that are not time-symmetric are excluded. In other words, the path followed by the crack front in $M(x_0, h(x_0, z_0), z_0)$ depends on the current geometry of the front (on $h(x = x_0, z)$) but not on the whole fracture surface ($h(x < x_0, z)$). Therefore, we expect the path equation to have the form.[36]

$$\frac{\partial h(x,z)}{\partial x} = F_{\text{el}}(h,z) + \eta(x,h,z) + F_0 \tag{4.25}$$

Limiting our investigation to linear models with h, the only elastic force that supplies all the previous requirements plus the various symmetric constraints linked to the system geometry (see the pages 46-48 of Ref. [65]), is $F_{\text{el}}(h,z) \sim \int \frac{h(z')-h(z)}{(z'-z)^\alpha} dz'$. If $\alpha = 2$, we recover the long-range elasticity of the crack front in an ideal elastic brittle material. If $\alpha = 3$, the elastic term is equivalent to a Laplacian term $\frac{\partial^2 h}{\partial z^2}$ [99] so that the elasticity of the effective crack front becomes purely local and the restoring force depends only on the local curvature. Tanguy et al. [99] have shown that the cases $\alpha < 2$ and $3 < \alpha$, respectively, are equivalent to the two previous cases, so that limiting our model to the range $2 \leq \alpha \leq 3$ is sufficient to test all the possible equations. Finally, within the various assumptions made here, the path equation for ductile fracture is

$$\frac{\partial h(x,z)}{\partial x} = A \int \frac{h(z') - h(z)}{(z'-z)^\alpha} dz' + \eta(x,h,z) + F_0 \tag{4.26}$$

where α is a free parameter to be fixed in the range $2 \leq \alpha \leq 3$. The noise η is supposed to be uncorrelated. Its properties – the spatial correlation lengths r_η^x, r_η^y and r_η^z and its magnitudes σ_x, σ_y and σ_z – as well as the coefficient A depend both on the material properties and the damage processes but are fixed and uniform in the material.

As in Section 4.1, the noise $\eta(x,h,z)$ is interpreted as a quenched noise so that the scaling exponents characterizing the solution of the Eq. (4.26) are ζ_{dep} and z_{dep} corresponding to the critical exponents at the depinning threshold. These exponents have been shown to depend only on the range α of the elastic term in Eq. (4.26) [99]. Renormalization group (RG) methods [39, 100] predict $\zeta_{\text{dep}} = (2\alpha - 3)/3$ and

[36] Inevitable imperfections in the loading system or in crack alignment are taken in consideration so that a small constant term F_0 is expected (See Section 4.1 for details).

$z_{\rm dep} = (5\alpha - 3)/9$ to first order in $\varepsilon = 2\alpha - 3$. Numerical simulations have been shown to be very powerful to solve pinning/depinning problems [92, 101]. The critical exponents $\zeta_{\rm dep}(\alpha)$ and $z_{\rm dep}(\alpha)$ has been measured very precisely through these numerical techniques for two situations: (i) $\alpha = 2$ leads to $\zeta_{\rm dep} = 0.39 \pm 0.005$ [82, 93] and $z_{\rm dep} = 0.78 \pm 0.02$ [84, 83] and (ii) $\alpha = 3$ leads to $\zeta_{\rm dep} = 1.26 \pm 0.01$ [39, 101] and $z_{\rm dep} = 1.51 \pm 0.03$ [102]. To get a rough estimation of $\zeta_{\rm dep}(\alpha)$ (resp. $z_{\rm dep}(\alpha)$) in the range $2 < \alpha < 3$, one can make a linear interpolation between these two values.

On the other hand, the experimental measurements made on ductile fracture surfaces have led to the "universal" exponents $\zeta_{exp} = 0.76 \pm 0.04$ and $z_{exp} = 1.24 \pm 0.06$ (see Tab. 2.3) irrespective of the studied material. An "arbitrary" value $\alpha \simeq 2.6$ used in our model would then allow to account for their values.

In other words, an effective crack front with non-local but rapidly decreasing interactions – with an elastic kernel in $\frac{1}{r^\alpha}$ with $\alpha \simeq 2.6 > 2$ – reproduces the Family−Vicsek scaling with the correct exponents observed on ductile crack surfaces. This suggests that, in average, the microcracks/cavities shield the interactions between two points of the crack. This is in agreement with the naive picture of ductile fracture: Damage ahead of the main crack concentrates the stress and makes the propagation of the information through the stress field of the unbroken material ahead the crack less efficient than in the ideal elastic case. In simple words, the effective crack front for a ductile failure is less stiff than in the brittle case. This results in a fracture surface with a higher roughness exponent.

Understanding the selected value $\alpha \simeq 2.6$ for this effective ductile crack front is a significant challenge for future investigations. This approach remains insufficient: With this simple model, it is not possible to account for the deviation to the Gaussian distributions of height variation fluctuations observed on the experimental ductile crack surfaces (see Section 2.2). This effect, which is not observed on brittle crack surfaces, suggests that the complex interactions with one microcrack/cavity and the main front must be investigated. In other words, the local disorder properties – taken constant everywhere in the material in our model – should depend on the local front shape. Models based on a coupling between disorder and line geometry is certainly the next step in the theoretical investigation of fracture surfaces resulting for non-linear processes of failure.

Conclusion

This study has related the morphology of fracture surfaces and the failure mechanisms in disordered materials. In particular, we have shown how the microstructural disorder influences the path followed by a crack and how it sets the self-affine geometry of fracture surfaces.

First, the relevant statistical properties of the roughness of experimental fracture surfaces have been identified. Two questions have been more specifically examined: Are they anisotropic with respect to the direction of propagation? This question is crucial because it may have very important applications: From the *post mortem* analysis of broken structures, one could find the direction of crack propagation and so the origin of the failure. On the other hand, to which extent do the surface properties depend on the material? To address these questions, five different materials have been studied: Aluminum alloy, silica glass, mortar, wood and quasicrystal. We have shown that the full description of fracture surfaces calls for the use of the 2D height−height correlation function, rather than just an analysis of 1D surface profiles. This function has been shown to follow a Family−Vicsek scaling that involves two independent scaling exponents: The roughness exponent $\zeta = 0.76 \pm 0.03$ and the growth exponent $\beta = 0.61 \pm 0.04$. They were shown to correspond to the self-affine exponents along the directions perpendicular and parallel to the crack propagation, respectively. Their value has been found to be independent, within experimental errors, of the material (aluminum alloy, silica glass, mortar, wood and quasicrystal) and of the crack growth velocity (within the range $10^{-12} - 10^{2}$ m s^{-1}). On the other hand, we showed that the distributions of height variations collapse onto a single master curve. This proves that the profiles along and perpendicular to the crack growth direction do not display multi scaling.

Regarding the dependence of the surface properties on the material, we found that materials made of cemented grains as sandstone displayed different scaling properties involving lower exponents $\simeq 0.4 - 0.5$. To understand the physical origin of their difference, we have studied an artificial material with a similar microstructure to sandstone, glass ceramics made of sintered glass beads. The characteristic size of their microstructure and the cohesion between grains can be tuned experimentally by modifying the bead diameter and the sample porosity. We showed that the fracture

surfaces of these materials display a Family−Vicsek scaling involving two exponents $\zeta = 0.40 \pm 0.03$ and $\beta = 0.48 \pm 0.04$ independent of the structural parameters and of the crack growth velocity in the range investigated. These exponents are significantly lower than those observed on various other disordered materials. This suggests the existence of a second "universality class" for failure problems.

To understand these results, and particularly the existence of two *a priori* different classes of fracture surfaces, we have then investigated theoretically the crack roughness in ideal linear elastic disordered materials. At first, we analyzed the stress field in the vicinity of a perturbed crack in a homogeneous elastic medium. Integrating the effect of the disorder on the crack motion, we derived a path equation for a crack in a disordered elastic material. This equation provides the fracture surface morphology that is shown to result from the motion of an effective elastic string that "creeps" within a 2D random quenched potential where the spatial position along the direction of crack propagation plays the role of time. The resolution of this equation leads to anisotropic fracture surfaces displaying a Family−Vicsek scaling with exponents $\zeta = 0.39$ and $\beta = 0.49$, irrespective of the crack growth velocity. These predictions are in good agreement with the experimental observations reported in glass ceramics and sandstone. Careful measurements of their macroscopic mechanical properties showed indeed that they behave as perfectly brittle materials, in coherence with the assumptions of the model. In other words, if one integrates the effect of the material disorder to the Linear Elastic Fracture Mechanics, one can explain *quantitatively* the morphology of fracture surfaces of brittle materials. Finally, we conjecture that the geometry of fracture surfaces of ductile materials may be captured if one takes into account the effects of the damage that screens the elastic interactions along the crack front.

Our study has been mainly devoted to the fracture surfaces of 3D materials. Other experiments have been performed in 2D geometries: Interfacial cracks propagating within the weak plane between two plates of Plexiglas [107, 108] and crack propagating in thin sheets of paper [109, 110]. The resulting crack surfaces have been shown to display also self-affinity, but they are characterized by roughness exponents different from those reported here for 3D fracture problems. Their value $\zeta_{\rm exp}^{\rm duc}$ is listed in

Fracture geometry	$\zeta_{\rm th}^{\rm br}$	$\zeta_{\rm exp}^{\rm duc}$	$\zeta_{\rm exp}^{\rm br}$
Interfacial	0.39 [83]	0.63 ± 0.03 [21]	?
2D	0.50 [103]	0.65 ± 0.05 [58, 104]	?
3D	0.39 [98]	0.76 ± 0.04 [33, 105]	0.40 ± 0.04 [106]

Table 4.3: Comparison between theoretical roughness exponent $\zeta_{\rm th}^{\rm br}$ for brittle fracture and measured roughness exponents $\zeta_{\rm exp}^{\rm duc}$ and $\zeta_{\rm exp}^{\rm br}$ for ductile and brittle fracture, respectively.

Tab. 4.3 and compared with the theoretical predictions $\zeta_{\text{th}}^{\text{br}}$ for a brittle failure in the same geometries. The experimental exponents are systematically larger than those expected for a brittle failure. We interpreted this abnormally high roughness exponent for 3D material as a signature of the damage processes occurring during the crack propagation. We suggest that the same interpretation is valid for interfacial crack and cracks in 2D media as previously proposed in Refs. [111, 103]. It should be noted that the present study of fracture in brittle materials is, to our knowledge, a unique example of agreement between the theoretical models and the experimental observations. Measurements for brittle materials in 2D geometries are still lacking and represent an important challenge for future experimental investigations.

Finally, the present study has focused on the geometrical properties of cracks. The natural next step will certainly be the study of their dynamical properties. One can imagine to compare the predictions of pinning/depinning models of crack propagation with crack front dynamics experimentally observed in interfacial failure [21]. This kind of models provides also some predictions on the relation between mean crack growth velocity and stress intensity factor. It would be interesting to test experimentally the relevance of these predictions. In this theoretical framework, the distribution of strength is also predicted to obey some peculiar scaling relations [90, 91] that would be interesting to investigate experimentally. Works in these directions are currently under progress.

Bibliography

[1] W. Weibull. A statistical theory of the strength of materials. *Proc. Roy. Swed. Inst. Eng. Res.*, **151**, 1–45 (1939).

[2] J. M. Boffa, C. Allain, and J. P. Hulin. Experimental analysis of fracture rugosity in granular and compact rocks. *Eur. Phys. J. Appl. Phys.*, **2**, 281–289 (1998).

[3] C. E. Inglis. Stresses in a plate due to the presence of cracks and sharp corners. *Trans. Inst. Naval Arch.*, **55**, 219–239 (1913).

[4] M. Marder and J. Fineberg. How things break. *Physics today*, **49**, 24–29 (1996).

[5] A. A. Griffith. The phenomena of rupture and flow in solids. *Phil. Trans. Roy. Soc. Lond.*, **A221**, 163–198 (1920).

[6] G. R. Irwin. Fracture. In *Handbuch der Physik*, volume 6, page 551. Springer-Verlag (1958).

[7] G. C. Sih. *Handbook of stress intensity factors.* Institute of fracture and solid mechanics (1974).

[8] B. Lawn. *Fracture of brittle solids.* Cambridge University Press (1993).

[9] R. V. Gol'dstein and R. L. Salganik. Brittle fracture of solids with arbitrary cracks. *Int. J. Frac.*, **10**, 507–523 (1974).

[10] B. Cotterell and J. R. Rice. Slightly curved or kinked cracks. *Int. J. Frac.*, **16**, 155–169 (1980).

[11] J. Hogdon and J. P. Sethna. Deviation of a general three-dimensional crack propagation law: A generalization of the principle of local symmetry. *Phys. Rev. B*, **47**, 4831–4840 (1993).

[12] E. Sommer. Formation of fracture lances in glass. *Eng. Frac. Mech.*, **1**, 539–546 (1969).

[13] D. Bonamy and K. Ravi-Chandar. Dynamic crack response to a localized shear pulse perturbation in brittle amorphous materials: on crack surface roughening. *Int. J. Frac.*, **134**, 1–22 (2005).

[14] F. Célarié, S. Prades, D. Bonamy, L. Ferrero, E. Bouchaud, C. Guillot, and C. Marlière. Glass breaks like metal but at the nanometer scale. *Phys. Rev. Lett.*, **90**, 075504 (2003).

[15] D. Bonamy, S. Prades, L. Ponson, D. Dalmas, C. L. Rountree, E. Bouchaud, and C. Guillot. Experimental investigation of damage and fracture in glassy materials at the nanometer scale. *Int. J. Prod. Tech.*, **26**, 339–353 (2006).

[16] R. Deegan, S. Chheda, L. Patel, M. Marder, H. L. Swinney, J. Kim, and A. De Lozanne. Wavy and rough cracks in silicon. *Phys. Rev. E*, **67**, 066209 (2003).

[17] O. Marchenko, D. Fichou, D. Bonamy, and E. Bouchaud. Time resolved observation of fracture events in mica crystal using scanning tunneling microscope. *App. Phys. Lett.*, **89**, 093124 (2006).

[18] L. Ponson, D. Bonamy, and L. Barbier. Cleaved surfaces of *i*-alpdmn quasicrystals: Influence of the local temperature elevation at the crack tip on the fracture surface roughness. *Phys. Rev. B*, **74**, 184205 (2006).

[19] G. I. Barenblatt. The mathematical theory of equilibrium cracks in brittle fracture. *Adv. Appl. Mech.*, **7**, 55–129 (1962).

[20] S. Nemat-Nasser and M. Hori. *Micromechanics: Overall Properties of Heterogeneous Materials*. Springer (1993).

[21] K. J. Måløy, S. Santucci, J. Schmittbuhl, and R. Toussaint. Local waiting time fluctuations along a randomly pinned crack front. *Phys. Rev. Lett.*, **96**, 045501 (2006).

[22] P. Daguier, B. Nghiem, E. Bouchaud, and F. Creuzet. Pinning and depinning of crack fronts in heterogeneous materials. *Phys. Rev. Lett.*, **78**, 1062–1065 (1997).

[23] M. Kanninen and C. Popelar. *Advanced Fracture Mechanics*. Oxford University Press (1985).

[24] D. Hull. *Fractography*. Cambridge University Press (1999).

[25] B. B. Mandelbrot, D. E. Passoja, and A. J. Paullay. Fractal character of fracture surfaces of metals. *Nature*, **308**, 721–722 (1984).

[26] E. Bouchaud, G. Lapasset, and J. Planès. Fractal dimension of fractured surfaces: A universal value? *Europhys. Lett.*, **13**, 73–79 (1990).

[27] K. J. Måløy, A. Hansen, E. L. Hinrichsen, and S. Roux. Experimental measurements of the roughness of brittle cracks. *Phys. Rev. Lett.*, **68**, 213–215 (1992).

[28] J. Schmittbuhl, F. Schmitt, and C. Scholz. Scaling invariance of crack surfaces. *J. Geophys. Res.*, **100**, 5953–5973 (1995).

[29] S. Morel, J. Schmittbuhl, J. M. Lopez, and G. Valentin. Anomalous roughening of wood fractured surfaces. *Phys. Rev. E*, **58**, 6999–7005 (1998).

[30] G. Mourot, S. Morel, E. Bouchaud, and G. Valentin. Anomalous scaling of mortar fracture surfaces. *Phys. Rev. E*, **71**, 016136 (2005).

[31] V. Y. Millman, N. A. Stelmashenko, and R. Blumenfeld. Fracture surfaces: a critical review of fractal studies and a novel morphological analysis of scanning tunneling microscopy measurements. *Prog. Mat. Sci.*, **38**, 425–474 (1994).

[32] E. Bouchaud and S. Navéos. From quasi-static to rapid fracture. *J. Phys. I France*, **5**, 547–554 (1995).

[33] L. Ponson, D. Bonamy, and E. Bouchaud. Two-dimensional scaling properties of experimental fracture surfaces. *Phys. Rev. Lett.*, **96**, 035506 (2006).

[34] S. Prades, D. Bonamy, D. Dalmas, E. Bouchaud, and E. Guillot. Nano-ductile crack propagation in glasses under stress corrosion: spatiotemporal evolution of damage in the vicinity of the crack tip. *Int. J. Solids Struct.*, **42**, 637–645 (2004).

[35] Y. Méheust. *Ecoulement dans les fractures ouvertes*. PhD thesis, Université Paris XI (2002).

[36] J. P. Bouchaud, E. Bouchaud, G. Lapasset, and J. Planès. Models of fractal cracks. *Phys. Rev. Lett.*, **71**, 2240–2243 (1993).

[37] D. Ertas and M. Kardar. Dynamic roughening of directed lines. *Phys. Rev. Lett.*, **69**, 929–932 (1992).

[38] M. Kardar. Nonequilibrium dynamics of interfaces and lines. *Phys. Reports*, **301**, 85–112 (1998).

[39] H. Leschhorn, T. Nattermann, S. Stepanow, and L. H. Tang. Driven interface depinning in a disordered medium. *Ann. Phys.*, **6**, 1–34 (1997).

[40] H. Larralde and R. C. Ball. The shape of slowly growing cracks. *Europhys. Lett.*, **30**, 87–92 (1995).

[41] S. Ramanathan, D. Ertas, and D. S. Fisher. Quasistatic crack propagation in heterogeneous media. *Phys. Rev. Lett.*, **79**, 873–876 (1997).

[42] S. Roux and H. Herrmann. *Statistical Models for the Fracture of Disordered Media*. Elsevier (1990).

[43] M. J. Alava, P. N. Nukala, and S. Zapperi. Statistical models of fracture. *Adv. Phys.*, **55**, 349–476 (2006).

[44] G. G. Batrouni and A. Hansen. Fracture in three-dimenssional fuse networks. *Phys. Rev. Lett.*, **80**, 325–328 (1998).

[45] V. I. Räisänen, M. J. Alava, and R. M. Nieminen. Fracture of three-dimensional fuse networks with quenched disorder. *Phys. Rev. B*, **58**, 14288–14295 (1998).

[46] A. Hansen and J. Schmittbuhl. Origin of the universal roughness exponent of brittle fracture surfaces: stress weighted percolation in the damage zone. *Phys. Rev. Lett.*, **90**, 45504 (2003).

[47] E. Bouchaud. Scaling properties of cracks. *J. Phys. Condens. Matter*, **9**, 4319–4344 (1997).

[48] J. Schmittbuhl, J. P. Vilotte, and S. Roux. Reliability of self-affine measurements. *Phys. Rev. E*, **51**, 131–147 (1995).

[49] I. Simonsen, A. Hansen, and O. M. Nes. Determination of the hurst exponent by use of wavelet transforms. *Phys. Rev. E*, **58**, 2779–2787 (1998).

[50] J. J. Amman and E. Bouchaud. Characterization of self affine surfaces from 3D digital reconstruction. *Eur. Phys. J. Appl. Phys.*, **4**, 133–142 (1998).

[51] J. L. Pouchou, D. Boivin, P. Beauchêne, G. Le Besnerais, and F. Vignon. 3D reconstruction of rough surfaces by sem stereo imaging. *Microchimica Acta*, **139**, 135–144 (2002).

[52] Ph. Ebert, M. Feuerbacher, N. Tamura, M. Wollgarten, and K.Urban. Evidence for a cluster-based structure of alpdmn single quasicrystals. *Phys. Rev. Lett.*, **77**, 3827–3830 (1996).

[53] Ph. Ebert, F. Yue, and K. Urban. Surface structure of cleaved icosahedral alpdmn single quasicristals after heat treatment. *Phys. Rev B*, **57**, 2821–2825 (1998).

[54] S. Prades. *Mécanisme de rupture du verre à l'échelle nanométrique*. PhD thesis, Université Pierre et Marie Curie-Paris VI (2004).

[55] M. Y. He, M. R. Turner, and A. G. Evans. Analysis of the double cleavage drilled compression specimen for interface fracture energy measurements over a range of mode mixities. *Acta Metall. Mater.*, **43**, 3453–3458 (1995).

[56] S. Morel, G. Mourot, and J. Schmittbuhl. Influence of the specimen geometry on r-curve behavior and roughening of fracture surfaces. *Int. J. Frac.*, **121**, 23–42 (2003).

[57] J. Feder. *Fractals*. Plenum (1988).

[58] E. Bouchbinder, I. Procaccia, S. Santucci, and L. Vanel. Fracture surfaces as multiscaling graphs. *Phys. Rev. Lett.*, **96**, 055509 (2006).

[59] S. Santucci, J. Mathiesen, K. J. Måløy, A. Hansen, J. Schmittbuhl, L. Vanel, A. Delaplace, J. Bakke, and P. Ray. Gaussian statistics of fracture surfaces. cond-mat/0607372.

[60] D. Amitrano and J. Schmittbuhl. Fracture roughness and gouge distribution of a granite shear band. *J. Geophys. Res.*, **107**, 2375–2390 (2002).

[61] J. Schmittbuhl, S. Gentier, and S. Roux. Field measurements of the roughness of fault surfaces. *Geophys. Res. Lett.*, **20**, 639–641 (1993).

[62] L. Ponson, D. Bonamy, and E. Bouchaud. Method and system for determining the propagation path of at least one crack from one or more fracture surfaces created by said crack(s). *Patent Application*, 11/311, 280 (2005).

[63] L. Ponson, D. Bonamy, and E. Bouchaud. Procédé et système de détermination du parcours de propagation d'au moins une fissure à partir d'une ou de surface(s) de rupture créée(s) par cette ou ces fissure(s). *Demande de Dépôt de brevet*, 511058 (2005).

[64] E. Bouchbinder, I. Procaccia, and S. Sela. Disentangling scaling properties in anisotropic fracture. *Phys. Rev. Lett.*, **95**, 255503 (2005).

[65] A. L. Barabási and H. E. Stanley. *Fractal concepts in surface growth*. Cambridge University Press (1995).

[66] F. Family and T. Vicsek. *Dynamics of fractal surfaces*. World Scientific (1991).

[67] S. Ramanathan and D. S. Fisher. Dynamics and instabilities of planar tensile cracks in heterogeneous media. *Phys. Rev. Lett.*, **79**, 877–880 (1997).

[68] E. Bouchaud, J. P. Bouchaud, D. S. Fisher, S. Ramanathan, and J. R. Rice. Can crack front waves explain the roughness of cracks? *J. Mech. Phys. Solids*, **50**, 1703–1725 (2002).

[69] H. Liebowitz, editor. *Fracture*, volume 5. Academic (1969).

[70] J. Schmittbuhl, S. Roux, and Y. Berthaud. Development of roughness in crack propagation. *Euro. lett.*, **28**, 585–590 (1994).

[71] J. M. Lopez and J. Schmittbuhl. Anomalous scaling of fracture surfaces. *Phys. Rev. E*, **57**, 6405–6408 (1998).

[72] G. Mourot, S. Morel, E. Bouchaud, and G. Valentin. Scaling properties of mortar fracture surfaces. *Int. J. Frac.*, **140**, 39–54 (2006).

[73] T. Backers, N. Fardin, G. Dresen, and O. Stephansson. Effect of loading rate on mode I fracture toughness, roughness and micromechanics of sandstone. *Int. J. Rock Mech. Min. Sci.*, **40**, 425–433 (1993).

[74] H. Gao and J. R. Rice. A first-order perturbation analysis of crack trapping by arrays of obstacles. *J. Appl. Mech.*, **56**, 828–836 (1989).

[75] M. Adda-Bedia, E. Katzav, and D. Vandembroucq. Second-order variation in elastic fields of a tensile planar crack with a curved front. *Phys. Rev. E*, **71**, 066127 (2006).

[76] R. C. Ball and H. Larralde. Three-dimensional stability analysis of planar straight cracks propagating quasistatically under type I loading. *Int. J. Frac.*, **71**, 365–377 (1995).

[77] A. B. Mochvan, H. Gao, and J. R. Willis. On perturbations of plane cracks. *Int. J. Solids Structures*, **35**, 3419–3453 (1998).

[78] G. C. Sih and H. Liebowitz. Mathematical theory of brittle fracture. *In Fracture*, volume 2, chapter 2. Academic Press (1968).

[79] A. B. Kolton, A. Rosso, and T. Giamarchi. Creep motion of an elastic string in a random potential. *Phys. Rev. Lett.*, **94**, 047002 (2005).

[80] A. Kolton, A. Rosso, T. Giamarchi, and W. Krauth. Dynamics below the depinning threshold in disordered elastic systems. *Phys. Rev. Lett.*, **97**, 057001 (2006).

[81] D. Ertas and M. Kardar. Critical dynamics of contact line depinning. *Phys. Rev. E*, **49**, R2532–R2535 (1996).

[82] A. Rosso and W. Krauth. Roughness at the depinning threshold for a long-range elastic string. *Phys. Rev. E*, **65**, 025101(R) (2002).

[83] J. Schmittbuhl, S. Roux, J. P. Vilotte, and K. J. Måløy. Interfacial crack pinning: Effect of nonlocal interactions. *Phys. Rev. Lett.*, **74**, 1787–1790 (1995).

[84] O. Duemmer. Conference on *Statistical physics in mechanics* in grasse, france, 11-23 june 2006.

[85] L. B. Freund. *Dynamic Fracture Mechanics*. Cambridge University Press (1990).

[86] Y. Pomeau. Symétrie des fluctuations dans le renversement dans le temps. *J. Physique*, **43**, 859–967 (1982).

[87] S. F. Edwards and D. R. Wilkinson. The surface statistics of a granular aggregate. *Proc. Roy. Soc. London, Ser. A*, **381**, 17–31 (1982).

[88] C.-H. Lam and L. M. Sanders. Inverse method for interface problems. *Phys. Rev. Lett.*, **71**, 561–564 (1993).

[89] J. Maunuksela, M. Myllys, J. Merikoski, J. Timonen, T. Kärkkäinen, M. Z. Welling, and R. J. Wijngaarden. Determination of the stochastic evolution equation from noisy experimental data. *Eur. Phys. J. B*, **33**, 193–202 (2003).

[90] S. Roux, D. Vandembroucq, and F. Hild. Effective toughness of heterogeneous brittle materials. *Eur. J. Mech. A*, **22**, 743–749 (2003).

[91] C. J. Bolech and A. Rosso. Universal statistics of the critical depinning force of elastic systems in random media. *Phys. Rev. Lett.*, **93**, 125701 (2004).

[92] S. Roux and D. Vandembroucq. Depinning transition as a critical phenomenon. *Int. J. Mod. Phys. B*, **17**, 4113–4122 (2002).

[93] D. Vandembroucq and S. Roux. Large-scale numerical simulations of ultrametric long-range depinning. *Phys. Rev. E*, **70**, 026103 (2004).

[94] A. Rosso, R. Santachiara, and W. Krauth. Geometry of gaussian signals. *J. Stat. Phys.*, L08001 (2005).

[95] J. P. Guin and S. M. Wiederhorn. Conference on *Fractography of glasses and ceramics* in Rochester, NY, USA, 9-12 July 2006.

[96] D. Bonamy, S. Prades, C. L. Rountree, L. Ponson, D. Dalmas, E. Bouchaud, K. Ravi-Chandar, and C. Guillot. Nanoscale damage during fracture in silica glass. *Int. J. Frac.*, **140**, 3–13 (2006).

[97] M. Reytier, S. Chapuliot, S. Marie, L. Ferry, and M. Nedelec. Study of cleavage initiation under thermal shock by tests on cracked rings and thermomechanical calculations. *Nucl. Eng. Des.*, **236**, 1049–1060 (2006).

[98] D. Bonamy, L. Ponson, S. Prades, E. bouchaud, and C. Guillot. Scaling exponents for fracture surfaces in homogeneous glass and glassy ceramics. *Phys. Rev. Lett.*, **97**, 125501 (2006).

[99] A. Tanguy, M. Gounelle, and S. Roux. From individual to collective pinning: effect of long-range elastic intercations. *Phys. Rev. E*, **58**, 1577–1590 (1998).

[100] O. Narayan and D. S. Fisher. Threshold critical dynamics of driven interfaces in random media. *Phys. Rev. B*, **48**, 7030–7042 (1993).

[101] A. Rosso. *Dépiégeage de variétés élastiques en milieu aléatoire*. PhD thesis, Université Pierre et Marie Curie-Paris VI (2002).

[102] O. Duemmer and W. Krauth. Critical exponents of the driven elastic string in a disordered medium. *Phys. Rev. E*, **71**, 061601 (2005).

[103] E. Bouchbinder, J. Mathiesen, and I. Procaccia. Roughening of fracture surfaces: the role of plastic deformation. *Phys. Rev. Lett.*, **92**, 245505 (2004).

[104] M. Mallick, P. P. Cortet, S. Santucci, S. G. Roux, and L. Vanel. Discrepancy between sub-critical and fast rupture roughness: a cumulant analysis. cond-mat/0607729.

[105] L. Ponson, D. Bonamy, H. Auradou, E. Bouchaud, G. Mourot, S. Morel, E. Bouchaud, C. Guillot, and J.P. Hulin. Anisotropic self-affine properties of experimental fracture surfaces. *Int. J. Frac.*, **140**, 27–36 (2006).

[106] L. Ponson, H. Auradou, P. Vié, and J.P. Hulin. Low self-affine exponents of fractured glass ceramics surfaces. *Phys. Rev. Lett.*, **97**, 125501 (2006).

[107] J. Schmittbuhl and K. J. Måløy. Direct observation of a self-affine crack propagation. *Phys. Rev. Lett.*, **78**, 3888-3891 (1997).

[108] A. Delaplace, J. Schmittbuhl, and K. J. Måløy. High resolution description of a crack front in a heterogeneous plexiglas block. *Phys Rev. E*, **60**, 1337–1343 (1999).

[109] S. Santucci. *Slow crack growth and crack pinning in heterogeneous media: experiments and models*. PhD thesis, Ecole Normale Supérieure de Lyon (2004).

[110] S. Santucci, L. Vanel, and S. Ciliberto. Subcritical statistics in rupture of fibrous materials: Experiments and models. *Phys. Rev. Lett.*, **93**, 095505 (2004).

[111] J. Schmittbuhl and A. Hansen. Roughness of interfacial crack fronts: stress-weighted percolation in the damage zone. *Phys. Rev. Lett.*, **90**, 045505 (2003).

[112] N. Shahidzadeh-Bonn, P. Vié, X. Chateau, J. N. Roux, and D. Bonn. Delayed fracture in porous media. *Phys. Rev. Lett.*, **95**, 175501 (2005).

[113] Y. Guenguen. *Introduction à la physique des roches*. Hermann (1992).

[114] M. F. Carrasco, S. K.Mendiratta, and J. M. Ferreira. Strength, porosity and permeability of sintered bodies made from glass microspheres. *Eur. Phys. J. Appl. Phys.*, **30**, 91–99 (2005).

Appendix A

Mechanical properties of glass ceramics

In this appendix, we will investigate the mechanical properties of glass ceramics. More precisely, our goal is to examine their rupture mode. The scaling properties of surfaces of fractured glass ceramics have been shown to be similar to those expected for an ideal brittle elastic heterogeneous material. We will see in this section that, at length scales larger than the size of the beads that constitutes it, glass ceramics can indeed be considered as perfectly brittle materials.

In the first paragraph, the presence of damage/microcracks during failure of glass ceramics in tension will be investigated. Then, macroscopic mechanical properties of these materials will be measured as a function of their porosity. The experimental results will be compared with the expected values for an ideal brittle elastic porous material.

Microcracks in glass ceramics : Let's investigate the presence of microcracks during the failure of glass ceramics. We can use the argument presented in Section 1.1 to assess the extent of the process zone – the zone in front of the main crack where microcracks are localized – in the glass ceramics samples. This leads to the following equation (see Eq. 1.9)

$$\ell_{pz} \simeq \frac{\pi}{8} \left(\frac{K_{Ic}}{\sigma^*} \right)^2 \tag{A.1}$$

Here, the quantities K_{Ic} and σ^* are defined at the macroscopic scale and we can measure it from the fracture tests performed on glass ceramics. In particular, the TDCB geometry used to obtain a quasi-static crack propagation (see Section 3.1), is well adapted to measure the toughness of a material because the crack is initiated from a notch. The curves load versus displacement obtained during the tests for samples of glass ceramics with three different porosities are shown in Fig. A.1. After an elastic regime where the displacement δ between the two points of force application

is proportional to the applied tensile force F, the crack initiates. Let us note that we cannot use this curve to assess the Young's modulus of the glass ceramics because the measured displacement is measured by the tensile machine and not directly on the sample. The force applied to initiate the crack is called F_c and coincides with the departure to this elastic regime. The toughness is then estimated using the expression $K_{Ic} = k_I F_c$ where k_I is the stress intensity factor for an applied force of magnitude unity in the same geometry.[1] This factor depends only on the geometry of the test and is found to be $k_I = 1250$ m$^{-3/2}$ through finite element calculation. Toughness values measured on glass ceramics samples with porosities ϕ ranging from 3% to 26% are listed in Table A.1.

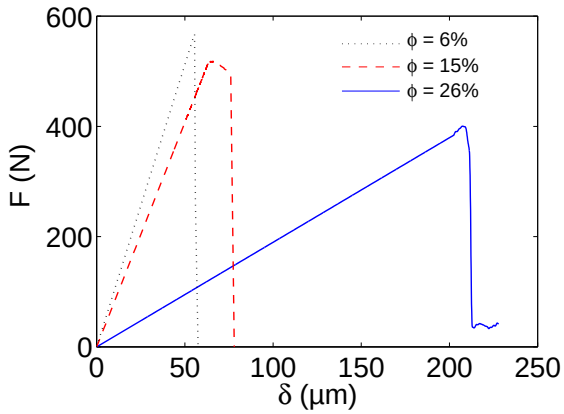


Figure A.1: Typical load versus displacement values obtained from three TDCB samples of glass ceramics with different porosities.

To assess their intrinsic strength σ^*, one will use the experimental study of N. Bonn et al. [112] performed on the same glass ceramics. In their work, they performed three points bending tests on bars of various porosities ϕ ranging from 23 % $< \phi <$ 47 %. We will fit their experimental results on σ^* with respect to ϕ on this range and will use them to extrapolate the values of σ^* on our range of interest, *i.e.* 3 % $< \phi <$ 26 %. Imposing a stress σ to the bar, they measured the span before failure $t_b(\sigma)$. This function is well fitted by $t_b \simeq c_1 e^{\frac{U_{act}}{k_B T}}$ with $U_{act} = g(\phi)/\sigma^4$ as shown in Fig. A.2. The function $g(\phi)$ is itself well fitted[2] by $g(\phi) \simeq c_2 exp^{-c_3\phi}$ as shown in the inset of Fig. A.2. In their experiments, the stress at rupture depends on the waiting time, the crack nucleation in these materials being a thermally activated process. To estimate the process zone size, one requires to assess the stress at rupture for a time $t* \simeq d/v_{crack}$

[1]The notch used in the experiments is 1 mm width. Therefore, the stress concentration at the notch tip is altered. As a consequence, this method is expected to slightly overestimate the value of the toughness of the glass ceramics samples .

[2]Let us note that N. Bonn *et al.* [112] used the following functions $g(\phi) \simeq (1 - 2\phi)^5$ to fit the same experimental data.

where d is the distance between two successive solid bridges in the material and v_{crack} the crack growth velocity. Taking $d \simeq 100$ μm the bead glass diameter and $v_{crack} = 50$ μm s^{-1} as the minimum crack speed observed during the various fracture tests – the crack growth velocity of each fracture test is listed in Table 4.1 –, we get a lower bound for σ^* that corresponds to the time scale $t^* \simeq 2$ s. This lower bound is given by

$$\sigma^* = e^{-c_3/4\phi} \left(\frac{c_2/k_B T}{ln(t^*/c_1)} \right)^{1/4} = \sigma_0 \, e^{-\frac{\phi}{0.18}} \tag{A.2}$$

with $\sigma_0 \simeq 90$ MPa. The real value of the intrinsic strength is certainly under estimates for small porosities – indeed, one would expect $\sigma^* \simeq \sigma_{glass} \simeq 3$ GPa when $\phi \simeq 0$ – but this point is not crucial because we are looking for a lower bound of the intrinsic strength. The latter are listed in Table A.1 as a function of the sample porosity ϕ.

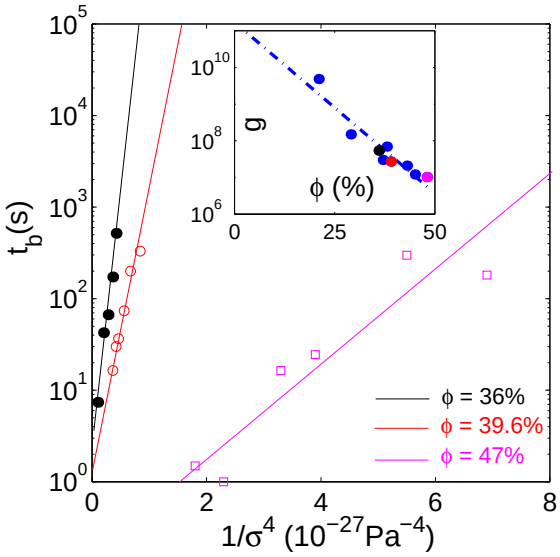


Figure A.2: Variation of the breaking time t_b of a test bar made of glass ceramics with the applied stress to the fourth power for three different porosities (courtesy of N. Bonn *et al.* [112]). The data can be well fitted by $t_b \simeq c_1 e^{g(\phi)/\sigma^4}$. The function $g(\phi)$ is plotted as a function of ϕ in the inset (courtesy of N. Bonn *et al.* [112]). It is found to be well fitted by $g(\phi) \simeq exp(-c_3\phi)$. From these expressions, one can assess the intrinsic strength σ^* of the glass ceramics corresponding to a given time scale t^*.

Using Eq. (A.1), we can now estimate an upper bound of the size of the process zone. The corresponding values are listed in Table A.1 for each broken sample. They are of the order of $1-2$ bead diameters for the largest porosities and smaller than 1 bead diameter for the lowest porosities. This result is in good agreement with the small R-curve effect[3] observed on a crack length propagation of $1-2$ bead diameters

[3]The R-curve effect is the observation of a transient regime in a fracture test where the crack is

during the fracture of samples with large porosities ($\phi \simeq 26$ %). The absence of R-curve effect for lower porosities confirms also this result.

The previous analysis based on the estimation of the process zone size of glass ceramics with Eq. (A.1) suggests that non-linear effects during the rupture of these materials occur at a scale smaller than the bead size. In other words, the roughness of fracture surfaces at larger scales than the bead size would be reminiscent of a brittle fracture in these materials. To confirm this important result, we propose a second argument based on the measurement of the fracture energy in the glass ceramics samples.

	$\phi = 3$ %	$\phi = 6$ %	$\phi = 15$ %	$\phi = 25$ %	$\phi = 26$ %
K_{Ic}	0.73 MPa m$^{1/2}$	0.71 MPa m$^{1/2}$	0.60 MPa m$^{1/2}$	0.40 MPa m$^{1/2}$	0.39 MPa m$^{1/2}$
σ^*	75 MPa	64 MPa	39 MPa	29 MPa	22 MPa
ℓ_{pz}	40 μm	50 μm	90 μm	120 μm	120 μm
E	20.6 GPa	18.7 GPa	15.3 GPa	10.9 GPa	10.9 GPa
ν	0.21	0.22	0.18	0.21	0.21
G_{Ic}	26 J m^{-2}	27 J m^{-2}	23 J m^{-2}	15 J m^{-2}	14 J m^{-2}

Table A.1: Mechanical properties of glass ceramics samples with various porosities ϕ and the same mean glass bead diameter $d = 116$ μm; (K_{Ic}) Toughness; (σ^*) Yield stress (lower bound); (ℓ_{PZ}) Process zone size estimated using Eq. (A.1) (upper bound); (E) Young's modulus; (ν) Poisson's ratio (G_{Ic}) Fracture energy

Griffith criterion for glass ceramics samples : Non-linear effects occurring during the failure of glass ceramics are very localized: (i) Damage processes induced by the high stress field at the tip of the (micro)cracks is essentially concentrated in a zone of 100 nm at their vicinity. (ii) Possible microcracks between consolidated glass beads around the front of the main crack are confined in a zone of the order of $1-2$ grains ahead the tip. They probably do not exist during the failure of glass ceramics with a low porosity. Therefore, one expects that a crack in these materials propagates roughly by breaking the solid bridges between grains one after the other. In other words, a single crack propagating in a glass ceramics sample is essentially made of broken bridges. In addition, very few broken bridges are present ahead of the main crack. To test this picture, we propose to estimate experimentally the variations of the fracture energy G_{Ic}[4] with the porosity ϕ of the glass ceramics samples. Comparing

initiated from a straight notch. In the first time of the fracture test, the process zone is growing and it is possible to reveal its presence by looking at the load versus displacement curve and its deviation to the brittle behavior. The distance covered by the crack during this transient regime is of the same order than the process zone size [56].

[4]The fracture energy G_{Ic} is the energy required to create two new fracture surfaces of unit area. G_{Ic} is always larger than the surface tension because the rupture involved dissipative and irreversible

this energy with the one required to break the solid bridges that constitutes the fracture surface, we will test the relevance of the scenario of brittle fracture of glass ceramics.

The relation $G_{Ic} = \frac{K_{Ic}^2}{E}$ is used to obtain the fracture energy for the samples used in the present study (Table A.1). We determine first the Young's modulus E of the samples: The velocity of sound in these materials as a function of their porosity[5] is measured with the help of Dominique Salin, Jérôme Martin and Fabrice Célarié. The experimental data plotted in Fig. A.3 a (see also Table A.1) are very well described by the relation

$$E \simeq E_0(1 - 2\phi) \tag{A.3}$$

with $E_0 = 22$ GPa. This relation is in excellent agreement with both experimental measurements performed on the same glass ceramics [112] and the predictions of a micromechanical model for the linear elasticity of porous media [20] (see [112] for details). The experimental procedure used to measure the toughness K_{Ic} of the glass ceramics has been described in the previous paragraph. Its variation with respect to the porosity is plotted in inset of Fig. A.3 b. Using the relation $G_{Ic} = \frac{K_{Ic}^2}{E}$, one obtains the fracture energy of glass ceramics plotted on the main panel of the same figure as a function of their porosity.

We now examine the compatibility of these experimental measurements with the proposed picture of the crack propagation in these materials. According to this scenario, the fracture energy G_{Ic} should be set by the total area of broken solid bridges between grains. The number of broken bridges is expected to vary very weakly with the sample porosity – the number of grains by unit volume is nearly constant. At the opposite, the area of one bridge depends crucially on the porosity. Therefore, one expects

$$G_{Ic} \sim S_{\text{bridge}} = \pi r_b^2 \tag{A.4}$$

A bead with one broken bridge is represented in Fig. A.4. The radius r_b of the fracture surface is fixed by the geometry of the bead

$$r_b^2 = (d/2)^2 - (d/2 - \ell)^2 \tag{A.5}$$

Here, d and ℓ are the bead diameter and the distance a bead moves towards a neighboring sphere during sintering, respectively. The latter are related to the porosity ϕ

processes: Once broken, the material cannot be healed by simply bringing back the two pieces back into contact.

[5] Young's modulus E and sound velocity v_{sound}, *i.e.* propagation velocity of compressive waves, are linked in an homogeneous material by the relation $v_{sound} = \sqrt{\frac{E}{\rho}}\sqrt{\frac{1-\nu}{(1-2\nu)(1+2\nu)}}$ [113] where ν is the Poisson's ratio and $\rho = \rho_{glass}(1-\phi)$ with $\rho_{glass} = 2530\,\mathrm{kg\,m^{-3}}$ the density of the glass ceramics. The frequency of the compressive waves is of the order of $f \simeq 500$ kHz so that the material is homogeneous at the scale of the corresponding wavelength $\lambda = \frac{v_{sound}}{f} \simeq 5$ mm. To assess the Poisson's ratio, we have also measured the propagation velocity v_{shear} of shear waves in the glass ceramics samples equal to $v_{shear} = \sqrt{\frac{E}{\rho}}\sqrt{\frac{1}{2(1+\nu)}}$.

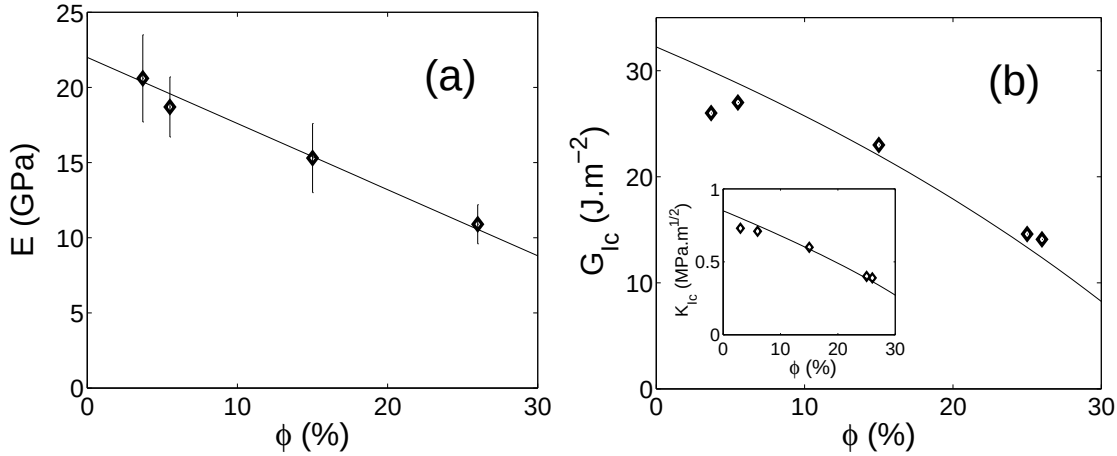


Figure A.3: Young's modulus (a) and fracture energy (b) variation with the porosity ϕ of the glass ceramics samples. The data presented in (a) and (b) are well described by the relations $E = E_0(1-2\phi)$ and $G_{Ic} = G_0 \frac{1}{1-c^{\frac{2}{3}}}(1-(\frac{c}{1-\phi})^{\frac{2}{3}})$ with $E_0 = 22$ GPa, $G_0 = 32$ J m^{-2} and $c = 0.64$ (represented in solid lines), respectively, in agreement with a brittle rupture model for these materials. The variations of the toughness measured experimentally are displayed in inset. The solid line displays the equation $\sqrt{E(\phi)G_{Ic}(\phi)}$ using the relations above.

by the expression

$$(1-\phi)(1-\frac{2d}{\ell}) = c \tag{A.6}$$

that is obeyed by any isotropically sintering body that preserves its solid mass [114]. c=0.64 is the random close packing compacity. Using Eq. (A.4), (A.5) and (A.6), one obtains

$$G_{Ic} \sim 1-(\frac{c}{1-\phi})^{\frac{2}{3}} \tag{A.7}$$

The corresponding curve is plotted in Fig. A.3 b and compared to the experimental measurements. The only adjustable parameter is the proportionality coefficient in the previous relation of proportionality (Eq. (A.7)). The fracture energy of a compact glass ceramics ($\phi = 0$ %) is adjusted to $G_0 = 32$ J m^{-2} which is a reasonable value compared to the fracture energy of the homogeneous glass $G_{glass} \simeq 10$ J m^{-2}. From Eq. (A.3) and (A.7) giving the variations of the Young's modulus and the fracture energy with respect to the porosity, one also gets the variations of the toughness – shown in inset of Fig. A.3 b. Variations of both fracture energy and toughness predicted within the assumption of brittle fracture of glass ceramics are in correct agreement with the experimental measurements. In other words, their macroscopic mechanical behavior is compatible with the proposed microscopic scenario of rupture.

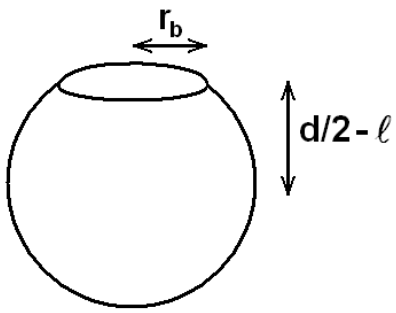


Figure A.4: Scheme of a bead with one broken bridge.

Concluding remark : Finally, from the previous analysis, we obtain a rather simple picture of crack propagation in glass ceramics samples under tensile condition: The crack is a well defined plane that propagates within the material by breaking the solid bridges between the sintered grains one after the other. In other words, the fracture of glass ceramics reproduces at the scale of the bead diameter the "classical" view of a perfectly brittle rupture usually applied to the cleavage of monocrystals at the atomic scale [8]. The choice of the glass ceramics motivated originally to the possible controlled variation of the microstructure of the broken material proved to be very relevant: In addition to the wide range of microstructures and related mechanical properties (see Eq. (A.3) and (A.7)) they allow to investigate, the fracture of glass ceramics represents an ideal tool to test the models of crack propagation in brittle disordered materials.

Appendix B

Publications

(i) L. Ponson, D. Bonamy and L. Barbier, Cleaved surface of *i*-AlPdMn quasicrystals: Influence of the local temperature elevation at the crack tip on the fracture surface roughness, *Phys. Rev. B*, **74**, 184205 (2006).

(ii) A. M. Bataille, L. Ponson, C. Gatel, E. Snoeck, S. Gota, L. Barbier, D. Bonamy and M. Gautier-Soyer. Characterization of antiphase boundary network in Fe_30_4 thin films : Effect on anomalous magnetic behaviour, *Phys. Rev. B*, **74**, 155438 (2006).

(iii) D. Bonamy, L. Ponson, S. Prades, E. Bouchaud and C. Guillot, Scaling exponents for fracture surfaces in homogeneous glass and glassy ceramics, *Phys. Rev. Lett.*, **97**, 135504 (2006).

(iv) L. Ponson, H. Auradou, P. Vié and J.P. Hulin, Low self-affine exponents of fractured glass ceramics surfaces. *Phys. Rev. Lett.*, **97**, 125501 (2006).

(v) L. Ponson, D. Bonamy and E. Bouchaud, Two-dimensional scaling properties of experimental fracture surfaces, *Phys. Rev. Lett.*, **96**, 035506 (2006).

(vi) L. Ponson, D. Bonamy, H. Auradou, G. Mourot, S. Morel, E. Bouchaud, C. Guillot and J. P. Hulin, Anisotropic self-affine properties of experimental fracture surfaces, *Int. J. Fracture*, **140**, 27-36 (2006).

(vii) D. Bonamy, S. Prades, C. L. Rountree, L. Ponson, D. Dalmas, E. Bouchaud, K. Ravi-Chandar and C. Guillot, Nanoscale damage during fracture in silica glass, *Int. J. Fracture*, **140**, 3-13 (2006).

(viii) D. Bonamy, S. Prades, L. Ponson, D. Dalmas, C. L. Rountree, E. Bouchaud and C. Guillot, Experimental investigation of damage and fracture in glassy materials at the nanometer scale, *Int. J. Materials & Product Technology*, **26**, 339-352 (2006).

French and American patent:

(ix) L. Ponson, D. Bonamy et E. Bouchaud, Procédé et système de détermination du parcours de propagation d'au moins une fissure à partir d'une ou de surface(s) de rupture créée(s) par cette ou ces fissure(s), *demande française de brevet*, 511058 (2005), *demande américaine de brevet*, 11/311, 280 (2005).

Résumé - Depuis près d'un demi-siècle, les ingénieurs savent décrire et prévoir la propagation d'une fissure dans un milieu élastique homogène modèle. Le cas des matériaux réels est beaucoup plus complexe. En effet, on ne sait pas relier leur durée de vie ou leur résistance à leur microstructure. Passage obligé avant de telles prédictions, il est nécessaire de comprendre comment le désordre structural du matériau influe sur le comportement d'une fissure. Dans cette optique, les surfaces de rupture représentent un champ d'investigation très prometteur.

A travers une étude portant sur divers matériaux hétérogènes, nous caractérisons les propriétés statistiques de leur rugosité et déterminons dans quelle mesure elles sont indépendantes du matériau. Nous montrons notament que les surfaces de rupture présentent des propriétés d'invariance d'échelle anisotropes, caractérisées par deux exposants universels. Etudiant ensuite une céramique de verre, matériau hétérogène modèle dont on peut contrôler la microstructure, on montre qu'il existe une seconde classe de surfaces de rupture caractérisée par la même structure anisotrope mais présentant des exposants plus faibles. Utilisant enfin des outils théoriques issus de la physique statistique hors équilibre combinés avec la mécanique de la rupture, nous établissons le lien entre ces propriétés et les mécanismes généraux de rupture à l'échelle microscopique. Cette étude nous permet notament d'associer les deux classes de surfaces de rupture à un processus de fissuration mettant en jeux de l'endommagement pour l'un et à une rupture parfaitement fragile pour l'autre.

Mots-clés : rupture, matériaux désordonnés, rugosité des surfaces de rupture, invariance d'échelle, mécanique de la rupture, ligne élastique en milieu aléatoire.

Abstract - For a half-century, engineers know how to describe and predict the propagation of a crack in a model elastic homogeneous medium. The case of real materials is much more complex. Indeed, we do not know how to relate their lifetime or their resistance to their microstructure. To achieve such a prediction, understanding the role of the microstructural disorder on the behavior of a crack is determinant. Fracture surfaces represent a promising field of investigation to address this question.

From the study of various disordered materials, we propose a statistical description of their roughness and determine to which extent their properties are dependent of the material. We show that fracture surfaces display an anisotropic scale invariant geometry characterized by two universal exponents. Glass ceramics is then studied because its microstructure can be tuned in a controlled manner. Their fracture surfaces display the same general anisotropic properties but with surprisingly low exponents independent of the detail of the ceramics microstructure. This suggests the existence of a second universality class in failure problems. Using finally theoretical tools from out-of-equilibrium statistical physics and fracture mechanics, we relate the statistical properties of fracture surfaces with the mechanisms occurring at the microscopic scale during the failure of a material. In particular, we show that the first class of fracture surfaces results from a failure involving damage processes while the second one results from a perfectly brittle failure.

Keywords : fracture, disordered materials, roughness of fracture surfaces, scaling invariance, fracture mechanics, elastic line in random medium.